

JUMR

Journal of Undergraduate Materials Research

"The Voice of Future Scientists and Engineers"

SOLAR HOUSES

You know you want one

DISCOVERIES & BREAKTHROUGHS INSIDE SCIENCE

Bringing science from the
laboratory to the living room

FEATURING RESEARCH FROM

Boise State

Wisconsin-Madison

Savannah State

Virginia Tech

North Carolina

Illinois Urbana-Champaign

A Publication of the Department of
Materials Science and Engineering at Virginia Tech

Volume 3 | Spring 2008

Dear Friends,

We are pleased to present Volume 3 of the *Journal of Undergraduate Materials Research*. Our third edition continues to build on the success of JUMR and to strengthen our collaboration with other departments, universities and organizations to provide an effective voice for the undergraduate researchers in materials science and related fields.

This year, we present papers from students at Boise State University, Savannah State University, the University of Illinois, the University of Kentucky, the University of North Carolina at Charlotte, Virginia Tech and the University of Wisconsin-Madison. The papers published were selected based on reviews by industry professionals, faculty and graduate students. The publication of papers from a variety of departments highlights the cross-disciplinary nature of the field of materials science and the broad impact of materials issues as we address many of the important engineering challenges facing us in the 21st century.

The past year has seen the JUMR grow in numerous ways. The collaborative effort envisioned by Alfred Knobler between the Departments of English and Materials Science and Engineering remains strong. This cooperation between liberal arts and engineering is reflected in the growth of our editorial board which now consists of members from seven departments and three colleges. The journal continues to expand its relationships with the materials professional societies through the creation of the American Ceramic Society (ACerS) best paper award and the organization of the first annual JUMR symposium at the MS&T'07 conference, allowing selected authors to gain experience in presenting their research to peers, faculty and industry leaders.

We are proud to be able to recognize the impact undergraduate students are making in the area of materials science and engineering. Through efforts such as a broader distribution and the JUMR symposium at MS&T'08, we hope to continue to increase the national attention given to undergraduate student research. Manuscripts are currently being accepted for upcoming editions, with those received by May 2nd, 2008 under consideration for Volume 4.

In closing, the staff of JUMR would like to congratulate all of our student authors for a job well done and thank each of our readers for their continued interest in the next generation of materials professionals.

Sincerely,

The Editorial Board

Back row (L-R): Kara LaFleur, Matt Brubaker, Niven Monsegue, Davis Eichelberger, Steven Kyriakides;
Middle row (L-R): Christelle Jullian, Mika Rivera, Michael Asaro, Susan Holt, Jessica Pritchard, Raghunathrao Thridandapani; **Front row (L-R):** Ben Poquette, Vaibhav Jain, Jairaj Payyapilly



Materials Science and Engineering
discover what we're made of...



On the cover:
Solar panel at the Virginia Tech CSES-Agronomy Farm.
Photograph by Matt Brubaker.

DISCLAIMER

The views, opinions and findings contained in the enclosed works are those of the individual authors. The publisher, editors, and authors assume neither responsibility nor liability for errors or any consequences arising from the use of the information contained herein. Mention of trade names or commercial products does not constitute endorsement or recommendations for use by the publishers, editors, or authors.

Final determination of the suitability of any information, procedure, or product for use contemplated by any user, and the manner of that use, is the sole responsibility of the user. This collection of works is intended for informational purposes only. Expert advice should be obtained at all times when implementation is being considered, particularly where hazardous materials or processes are encountered.

Journal of Undergraduate Materials Research (ISSN 1934-7677) Copyright © 2008 by the Virginia Tech Department of Materials Science and Engineering.

FEATURE ARTICLES

- 05 Letter from the Department Head**
David Clark, MSE
- 06 Solar Houses: You know you want one**
Jessica Pritchard, English
- 10 Discoveries and Breakthroughs Inside Science**
Lane W. Martin, Diane Hickey, Ben Poquette, Professor Kevin Jones,
& Professor Jerrold Floro
- 12 Materials Advantage Students Visit Washington**
Tricia L. Niswonger
- 63 Materials Professional Societies**
- 64 Upcoming Materials Conferences**



6

FEATURED DEPARTMENTS

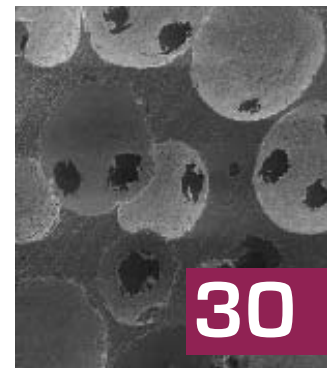
- 15 University of Wisconsin-Madison & Boise State University**

RESEARCH ARTICLES

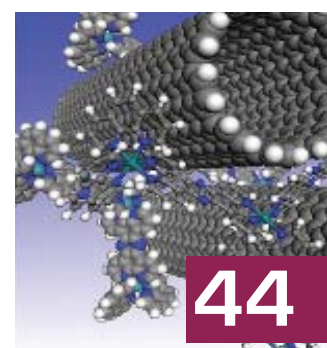
- 16 Structural Assessment of an Internal Fixation System for a Forearm Long Bone Mid-shaft Fracture**
MyKal Woody, Savannah State University
- 21 Biocompatibility and Hardness of Ti-Hf and Diamond-like Carbon Coatings for Orthopedics**
Stephanie Kuhn, University of Wisconsin - Madison
- 26 Optical Properties of an Electrochromic Device Based on Poly (aniline 2-sulfonic acid (PASA) Film, Formed by Ionically Self-Assembled Multilayers (ISAM) Technique**
Reza Montazami, Virginia Polytechnic Institute and State University
- 30 Characterization of Electrolessly Plated Graphite Foams with Particle Additions**
Michael Asaro, Jennifer Mueller, Patrick Dykema, Virginia Polytechnic Institute and State University
- 34 The Effect of Cornstarch Levels on the Surface Quality of Extruded Soy Protein Plastic**
Evan M. Ziolkowski, University of Wisconsin–Madison
- 38 Statistical Analysis of Impedance Data for Jet Turbine Oil Additives**
Matthew T. Luke, Boise State University
- 44 Ruthenium Coordination Chemistry: Implications for Directed Carbon Nanotube Assembly**
Thomas J. Younts University of North Carolina at Charlotte
- 50 Percolation of Fibrous and Bimodal Fillers in Thermoreversible Gelcast Aluminum Oxide**
Kristina Bond, University of Illinois Urbana-Champaign
- 56 Evaluation of Bearing Steel Corrosion in Oil Contaminated with Synthetic Seawater**
Brandon W. Christoffersen, Boise State University



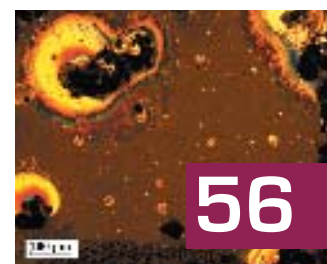
16



30



44



56

FACULTY REVIEWERS

Iver Anderson, *Iowa State University*
 Shawn Kelly, *Penn State*
 Kalayanu Kooptarmond, *University of Thailand*
 Morsi Mahmoud, *Advanced Technologies and New Materials Research Institute (ATNMRI), MuCSAT, Alexandria, Egypt*
 Gabor Muccsi, *University of Miskolc*
 William B. Spillman Jr., *University of Vermont*
 Diane Folz, *Virginia Tech*
 Paul Gatenholm, *Virginia Tech*

INDUSTRY REVIEWERS

Mike Bortner, *Nanosonic, Inc.*
 Matthew Hallihan, *Alcoa*
 Nagraj Kulkarni, *Oak Ridge National Labs*
 Judson Marte, *General Electric*
 Thomas Prucha, *AFS Inc*
 Garth Tormoen, *Southwest Research Institute*

GRADUATE STUDENT REVIEWERS

Kris Behler, *Drexel*
 Rahul Bhowmik, *North Dakota State University*
 Suresh Donthu, *Northwestern*
 Jessica Lensch Falk, *Northwestern*
 Dan Giarnola, *Johns Hopkins*
 Jennifer Kauffman, *Clemson*
 Rohit Khanna, *North Dakota State University*
 Mohammad Nazzal, *University of Kentucky*
 Anup Pancholi, *University of Delaware*
 Vishal Warke, *University of Alabama*
 Ka Wong, *North Carolina State University*

SPECIAL THANKS

David Clark, *Professor and Head*
 Materials Science and Engineering, Virginia Tech
 Carolyn Rude, *Professor and Chair*
 English, Virginia Tech
 Material Advantage
 Micron Technology, Inc.
 Alcoa, Inc. Campus Partnership Program

STUDENT EDITORIAL BOARD

Editor-in-Chief DAVIS EICHELBERGER
 Graduate Student,
 Materials Science and Engineering

*Co-Editor-in-Chief,
 Communications & Data Manager* SUSAN HOLT
 Graduate Student,
 Materials Science and Engineering

Editor-in-Chief Emeritus BEN POQUETTE
 Graduate Student,
 Materials Science and Engineering

Finance Manager CHRISTELLE JULLIAN
 Graduate Student,
 Materials Science and Engineering

Production Editor JESSICA PRITCHARD
 Undergraduate Student,
 English

Graphic Design Editor MATT BRUBAKER
 Undergraduate Student,
 Communication

Public Relations Manager STEVEN KYRIAKIDES
 Graduate Student,
 Materials Science and Engineering

Undergraduate Liaison MICHAEL ASARO
 Undergraduate Student,
 Materials Science and Engineering

Photographer NIVEN MONSEGUE
 Graduate Student,
 Materials Science and Engineering

Staff

JAIRAJ PAYYAPILLY
 Graduate Student, Materials Science and Engineering

JENNIFER MUELLER
 Graduate Student, Materials Science and Engineering

DANIEL CLEMENTS
 Undergraduate Student, Mechanical Engineering

VAIBHAV JAIN
 Graduate Student, Macromolecular Science and Engineering

MUNUSAMY PRABHAKARAN
 Graduate Student, Materials Science and Engineering

RAGHUNATHRAO THRIDANDAPANI
 Graduate Student, Materials Science and Engineering

MICHAEL WOODDELL
 Graduate Student, Materials Science and Engineering

KARA LAFLEUR
 Graduate Student, English

FACULTY EDITORIAL BOARD

JUMR Faculty Advisor DIANE FOLZ
 Materials Science and Engineering

Materials Science and Engineering ALEX ANING
 STEPHEN KAMPE
 GARY PICKRELL

Engineering Education MAURA BORREGO
 JEAN KAMPE

English EVA BRUMBERGER

Engineering Science and Mechanics, Materials Science and Engineering CHRISTINE BURGoyNE

Engineering Education, Virginia Tech Engineering Communications Center, MSE/ESM Engineering Communications Program MARIE PARETTI

Letter from the Department Head

David Clark, Materials Science and Engineering



Dear Students and Colleagues:

As is evident from the papers presented in the first three volumes of JUMR, we as faculty place a great deal of emphasis on providing a research experience for our students – undergraduate as well as graduate. The papers published in JUMR represent a fraction of the research that is on-going in the broad world of materials. Faculty,

industrial and government program managers know that keeping research funding in place for a wide range of topics and for all levels of students presents an extraordinary challenge.

Through participation in Congressional Visits Days (CVD), students from across the country have a unique opportunity to raise awareness about the vital role of funding for materials research in academia as well as government and industrial laboratories. The efforts of young people to engage our nation's leaders in dialogue on critical areas of research and education is gaining momentum as more and more students are visiting their senators and representatives. In the materials community, these activities are being organized by the Federation of Materials Societies (FMS) and Material Advantage (MA) Student Organization.

“The Materials S&E Students’ Congressional Visits Days provide a unique experience not only for the undergraduates and grad students who come to Washington, but also for the members of Congress and their staffs who interact with them. The students gain an understanding of how federal research policies are made, and how those decisions affect their academic and future professional careers. Senators and Representatives and their staffs gain a perspective they are not able to get from the statistical tables on university research they are constantly bombarded with. Through the students’ visits, faces are put on the numbers, and the enthusiasm is contagious. Student Congressional Visits Days are vital elements in the materials community’s advocacy efforts. Thanks to everyone who participates!”

-Betsy Houston,
Executive Director
Federation of Materials Societies

“Student participation in Congressional Visits Day has been an invaluable component all around. The accompanying training and experience of conducting the visits are very insightful into the inner working of the Federal government. Students are exposed to detailed information on how innovation directly fuels the Nation’s economy, while furthering America’s competitiveness in the global climate. Legislators and their staff are engaged by students who discuss their research and how they directly benefit from federally funded research. The promise of tomorrow is eloquently conveyed by students who share their enthusiasm for the material sciences & engineering.”

- Christian McKelvey,
Former Manager of Member Services & Student Affairs The
Minerals, Metals & Materials Society

“Conveying the importance of materials science and engineering education and research to congressional staffers is an extremely important task. Having our students serve as ambassadors to convey the excitement and potential of the discipline has to be one of the best ways to deliver our message.”

- Ian Robertson,
Professor and Head,
Materials Science and Engineering, University of Illinois

It is important for us to remember that our students are the future of engineering and science in the U.S. As word of the CVD events and JUMR reach more students, we hope they will choose to become an even larger force in keeping the research wheel turning. We hope that university faculty and administration understand the important role that students can have in shaping the future of R & D and will help support their travel to CVD.

Sincerely,

David E. Clark
Professor and Head
Materials Science and Engineering
Virginia Tech



Figure 1. University of Santa Clara's solar house

Jessica Pritchard, English

Amidst an unceasingly intricate political agenda lies what many consider a grave and often ignored issue: global warming. It would be naïve to overlook the current international political and financial demands, but few can refute global warming's ever-increasing presence looming on the horizon.

Fortunately, technological developments have brought about more affordable alternative energy sources, though most still require a fairly steep investment. I stress the term investment because alternative energy sources aren't something you can purchase with those ten hours of overtime last week, but thinking in the long-term, imagine the benefits that will come from your green steps into the future.

The Basics

Solar panels convert sunlight into electricity through photovoltaic cells that use solar energy to free electrons, allowing them to flow through the cell to create electricity.^[1] The sun offers enough daily energy to generate and meet global energy needs. Unfortunately, current technology generates a mere one-tenth of one percent of these energy needs.^[1] This is not to say, however, that the technology available today won't contribute to a healthier environment tomorrow.

Though solar technology remains in the beginning phases of alternative energy developments, the products out today appear to be more attuned to environmental awareness than ever

before. Despite the slightly higher price tags and comparably fewer energy efficient products, green participation is far more attainable than most would think, which is the idea universities around the world have embraced through their design and construction of individualized solar houses.

Solar Houses: They're All The Rage

The Solar Decathlon, an annual competition held on the National Mall in Washington, D. C. where 20 universities vie to build the best solar-powered house, serves as a public venue that demonstrates not only effective use of solar energy but also creative structural design. Participants, aware that every aspect of their design must use solely solar power, face the challenge of integrating innovative ideas with high-tech materials to make “powerful, comfortable, and stylish” homes that waste neither space nor energy.^[2] Simply put, the Solar Decathlon illustrates the amalgamation of nature and technology.

This year's Solar Decathlon winner hails from Germany. The Technische Universität Darmstadt, using strictly German-manufactured products, has created a solar house where the owner uses every nook and cranny, wasting little to no space. Not only does the Technische Universität Darmstadt take the lead in student-constructed solar houses but they also serve as the lead architects in creating a solar-powered campus, known as Solare Lichtweise. The university is in the process of installing solar panels atop each of its academic buildings that will then feed into the German power grid.^[8] Outside of the university, Germany has implemented a “solar feed-in tariff,” offering a 20-year flat rate contract that allows citizens to tap into the German power grid. This tariff will not only cover the initial cost of installing the solar panels but will also pay off in the long-run because of the contract's flat rate, further corroborating the investment aspect of solar energy.^[8]

The University of Maryland's LEAFhouse placed second at this year's competition, combining not only energy efficiency but also sustainability. LEAFhouse's features include a curved roof with solar panels arranged in angles intended to mimic the change in the sun's altitude over a year; a raised elevation that allows for nature to reclaim the earth (“reducing its footprint, literally and figuratively, of the land”) yet keeps the house anchored to the ground; and renewable construction materials, such as FSC-certified lumber and bamboo flooring.^[6] LEAFhouse uses a photovoltaic power system, one of the most com-



Figure 2. 3D Model of University of Maryland's solar house

mon features in solar-powered homes, that generates electricity through solar panels, charges batteries that then store electricity, and converts solar energy into traditional household alternating current. The house's plumbing features Aquatherm Fusiotherm polypropylene pipes fused together with fittings, reducing the likelihood of cracks and breaks.

The University of Santa Clara, ranked third at this year's event, believes that idealism drives their “design with purpose” mentality, as displayed in their Ripple House. Students from the School of Architecture and the School of Engineering featured energy-efficient materials in their design, such as integrated bamboo I-joists, which can hold up to 10,390 pounds before breaking or even bending. Bamboo is not only energy-efficient but also environmentally friendly, having a faster growth rate than wood and a root system that allows new shoots to grow from old stalks.^[7] Like the University of Maryland's LEAFhouse, the Ripple House implements a 7.5 kilowatt photovoltaic system that has a battery reserve compiled of 2,500 pound lead-acid batteries that can run up to five days without sunshine. Perhaps one of the most innovative features of the Ripple House, however, lies in the NanaWall, a sliding glass door that serves as both a window and a wall. This eight-foot wide structure contains highly-insulated, triple-pane glass that allows the maximum natural light to enter into the home with minimal energy

lost through heat transfer.^[7] Eco-friendly powder coat paints, water-based wood finishes and recyclable aluminum adorn this NanaWall, completing the environmentally conscious design.

The Virginia Tech team, who competed in the 2005 Solar Decathlon and received first place in the architecture competition, seeks to inform and educate on alternative energy through collaboration among students, faculty, and staff from the College of Architecture and Urban Studies and the College of Engineering. Tech's solar house has an energy-efficient V-shaped roof that holds 36 adjustable 200-watt SunPower solar panels, which not only produces energy but also collects rain, further contributing to another form of environmental friendliness—water conservation.^[4] This rainwater then supplies the house's water-filtering system. Aside from using innovative technology, Tech's solar house pays fine-attention to aesthetics—"the emphasis was on environmentally friendly materials for sustainable living."^[4] For instance, the floors consist of eucalyptus wood that expands and contracts as the room heats and cools, while the furniture consists of butcher block, which pieces together smaller chunks of wood rather than cutting large slabs from trees, thereby using more and wasting less.^[4] Beyond solar panels and environmentally-friendly materials, Virginia Tech students also chose energy-efficient appliances, including low-flow faucets, as well as a dishwasher, washer, and dryer with energy star ratings. You can even decide the water level used when flushing the toilet.^[4]

The walls are perhaps one of the most innovative features of Tech's solar house because they function as a light source within themselves, serving as the light and allowing you to select different colors. Three of the house's walls have two layers of panels filled with translucent insulation. Between these panels lie three systems: "a motorized shade that allows the user to control light and heat; linear, actuated vents at the top and bottom that provide ventilation for further thermal control; and dimmer-controlled LED lights that allow the user to make the wall and color, no paint required."^[4]

Bring It Down a Notch

These energy efficient features aren't strictly intended for academic exploration—you really can integrate even the smallest of features into your everyday life. The technologies available today can and will meet your daily energy needs through solar power.

Bear in mind, though, that a solar electric system alone will likely cost upwards of \$72,000. With that said, if you plan on building a solar-powered home, or even giving your current home a green facelift, understand that it may take a while for you to start reaping the financial benefits. Living in a solar-powered



Figure 3. Interior of the University of Santa Clara's solar house

home isn't one of those instant gratification splurges, though some may say that saving the environment is pretty rewarding, with or without fiscal reward.

With that said, if building a solar house falls slightly outside of your designated budget, try a few of these energy saving tips offered by National Geographic:

- 1- Replace your 75-watt incandescent light bulbs with 19-watt compact fluorescents;
- 2- Take the train for those shorter distance trips;
- 3- Use a fan rather than an air conditioner;
- 4- Replace older refrigerators (10 years or older) with more energy-efficient Energy Star models;
- 5- Quit taking long showers! Limit yourself to 5 minutes. This is really all you need;
- 6- Dry your clothes outside whenever possible. They'll smell better anyway;
- 7- Eat more fish, eggs, and poultry—it exhausts fewer fossil fuels;
- 8- Use public transportation whenever possible. It can be fast, convenient, and often fairly cheap.^[9]

Life has innumerable uncontrollable factors—energy conservation doesn't have to be one of them. For once, we each can take active steps towards eliminating, or at the very least reduc-



ing, energy consumption, thereby ameliorating the irreversible effects of global warming.

Go green. Live clean. You know you want to.

Further Resources

United States Green Building Council

www.usgbc.org

Ecological Home Ideas

www.ecologicalhomeideas.com

Ecobroker International

www.ecobroker.com

Alliance to Save Energy

www.ase.org

Partnership for Advancing Technology in Housing

www.pathnet.org

References

- [1] "Solar Energy: A Surging Energy Source." *National Geographic*. Date Accessed: 22-Oct-2007. <http://green.nationalgeographic.com/environment/global-warming/solar-power-profile.html?nav=FEATURES>
- [2] Walker, Cameron. "The Future of Alternative Energy." *National Geographic*. 28-Oct-2004. http://news.nationalgeographic.com/news/2004/10/1028_041028_alternative_energy.html
- [3] DOE Solar Decathlon Homepage. Date Accessed: 24-Oct-2007. <http://www.solardecathlon.org/about.html>
- [4] Virginia Tech Solar Home Homepage. Date Accessed: 18-Oct-2007. <http://vtsolar.arch.vt.edu>
- [5] Virginia Tech Spotlight on Innovation. "When the solar revolution knocks, a Virginia Tech collaboration answers." 11-Jan-2007. http://www.vt.edu/spotlight/20061204_solar.php
- [6] University of Maryland Solar Decathlon Homepage. Date Accessed: 29-Oct-2007. <http://solarhouse.umd.edu/page.php?id=65>
- [7] University of Santa Clara Solar Decathlon Technology Page. Date Accessed: 30-Oct-2007. <http://www.scusolar.org/technology>
- [8] Technische Universität Darmstadt Solar Decathlon Homepage. Date Accessed: 13-Nov-2007. http://www.solardecathlon.org/2007/team_darmstadt.html
- [9] Karlstrom, Solvie. "Top Ten Tips to Fight Global Warming." *National Geographic*. 5-June-2007. <http://www.thegreenguide.com/blog/tow/825>

About the Author

Jessica hails from Virginia Tech's English department, representing one of three English students to sit on JUMR's editorial board. She completed her undergraduate degree in May of 2007 during Volume 3's publication. She spent much of her time at Tech tutoring in The Writing Center and swing dancing with Solely Swing, the university's student-run swing dancing club. On most days, though, you could find her fulfilling her barista duties at the Daily Grind, serving the best cup of coffee in the world. Yeah!

DISCOVERIES AND BREAKTHROUGHS INSIDE SCIENCE:

Bringing science from the laboratory to the living room.



A partnership between the National Science Foundation, the American Institute of Physics, the Materials Research Society, and many more for the advocacy of science and technology in society.

Lane W. Martin¹, Diane Hickey², Ben Poquette³, Professor Kevin Jones², & Professor Jerrold Floro⁴

¹University of California, Berkeley, Department of Materials Science and Engineering

²University of Florida, Department of Materials Science and Engineering

³Virginia Polytechnic Institute and State University, Department of Materials Science and Engineering

⁴University of Virginia, Department of Materials Science and Engineering

Have you ever kicked back to watch your favorite science-based TV programming and had the thought, “That’s not so hard, I could do that.” With the help of a partnership between the National Science Foundation (NSF), the American Institute of Physics (AIP), 19 professional scientific organizations, including the Materials Research Society (MRS), and Ivanhoe Broadcast Network, Inc., you might have the chance to be a science-star for a day and to bring your work in the laboratory to the living rooms of millions of American television viewers.

The program, entitled Discoveries and Breakthroughs Inside Science (DBIS), is a syndicated science and engineering news service for local television newscasts. DBIS, which produces twelve 90-second news segments per month, makes sure that each segment is reviewed for scientific accuracy and is centered on a broad range of topics in engineering, science, technology, and mathematics (STEM). DBIS has been producing science related news stories since 2000 with the goal of promoting awareness and appreciation among local TV news viewers of the role of STEM in society. By delivering a broad spectrum of research news, DBIS hopes to highlight the critical role of science and engineering to society while exposing audiences to a diverse array of STEM professionals.

DBIS was founded on the premise that most of the American public does not pick up the latest copy of *JUMR*, *Science*, *Nature*,

or other science-related publications to get their science news. Studies have shown that the majority of the American public gets their (limited!) science-based news exclusively from TV. Studies by the Pew Research Center have found that since 2000 more than 56% of those polled regularly watched TV news programming^[1] and a NSF Science and Engineering Indicators (SEI) study that same year found that 44% of those polled cited TV as their leading source for science and technology information.^[2] Of those polled in these studies, only 8% noted that they watched in-depth science programming like *NOVA* on PBS. Furthermore, the 2004 NSF SEI study found that 50% of those surveyed would be interested in hearing about STEM developments; however, only 15% of those surveyed considered themselves “well informed” while 30% considered themselves “poorly informed” about science and technology in society today.^[3] Over the last decade, the way in which the public gets their news and information has changed greatly. However, even as internet and online news sources have flourished at the expense of other more traditional news sources, TV has remained a steady source of news for many individuals.^[1]

With this in mind, the American Institute of Physics and the NSF paired up with a number of scientific professional organizations to create the DBIS program. DBIS focuses its efforts on creating over 144, 90-second peer-reviewed reports for dissemination on TV news casts and on the internet each year.

The stories produced by DBIS come from many locations—in a period from May 2005 to April 2006 DBIS produced 59 stories from research universities press releases, 29 from partnership contacts, like MRS, 19 from journals or news magazines, 17 from professional STEM meetings, 11 from newspaper articles, 7 from government or company press releases, and 2 from internet science news websites. As partnerships organizations evolve the symbiotic nature of DBIS has grown. MRS, for instance, has seen fit to extend their involvement with DBIS after an exciting and fruitful initial experience in the program. The MRS-based DBIS Committee consists of members of different ages, scientific backgrounds, and geographic locales, in order to bring well-balanced, broadly interesting materials-related news from the ranks of the MRS membership to the American public. When searching for new stories for submission, the MRS committee is looking for stories that will be visually stimulating and transition well from paper to the camera. In order to impact the broadest number of viewers, stories must be of interest nationally and should provide direct benefits to the general public in the next few years. All in all, the committee tries to identify new materials research that has resulted in a tangible solution or explains a scientific or technical mystery that is of interest to more than just their scientific colleagues. Most importantly, the news is about the people, about the researchers involved, and the committee is always searching for a scientist or outside expert who can illustrate a complex concept to a general audience. By putting a face to the research, DBIS has the best chance to bring science to the general public.

In the first year of the MRS committee's involvement with the DBIS program, we have experienced great success in bringing the work of MRS members to story production. We have successfully been involved in the production of stories ranging from Man-Made Diamonds to Metal Rubber to bioactive toothpaste. And most importantly, the program works. As of February 2007, there were over 110 stations in the United States with subscriptions to the DBIS program. This means that on any given day a DBIS story could reach over 70 million viewers in the United States as well as the viewers of another 48 Spanish language stations. Furthermore, DBIS has partnered with public transit organization in cities like Atlanta, Chicago, Los Angeles, Milwaukee, Norfolk, Orlando, and San Diego, to bring DBIS clips to the riders of public transportation. Finally, DBIS has also extended its dissemination to new platforms including Roo Media, ScienceDaily, Voxant, Clip Syndicate, and Voice of America (seen in over 13 countries). This continued growth has led to the production of the 1000th DBIS segment in 2006 and hope for continued success in years to come.

If you are interested in seeing your research gain nationwide attention or know of a great scientific mind who could bridge the divide between the general public and science, please contact the MRS-DBIS committee: Chair - Prof. Jerry Floro, Uni-

versity of Virginia, floro@virginia.edu, or Anita Miller, MRS Headquarters, amiller@mrs.org. Our stories can be viewed at: www.aip.org/dibs.

DBIS Partner Organizations:

Acoustical Society of America; American Association of Physics Teachers; American Association of Physicists in Medicine; American Geophysical Union; American Industrial Hygiene Association; American Institute of Physics; American Mathematical Society; American Meteorological Society; AVS Science and Technology Society; American Society of Civil Engineers; American Society for Microbiology; American Water Works Association; Human Factors and Ergonomics Society; Incorporated Research Institutions for Seismology; Institute of Electrical and Electronic Engineers – USA; Materials Research Society; Mathematical Association of America; National Science Foundation; Optical Society of America; Space Telescope Science Institute; Universities Research Association

Related Links:

DBIS - www.aip.org/dibs
 Pew Research Center - <http://people-press.org>
 Gemesis Corp. - <http://www.gemesis.com>
 Nanosonic, Inc. - <http://www.nanosonic.com>
 U.S. Biomaterials Corp. - <http://www.usbiomat.com>
 Roo Media - <http://www.roo-media.com>
 ScienceDaily - <http://www.sciencedaily.com>
 Voxant - <http://www.voxant.com>
 Clip Syndicate - <http://www.clipsyndicate.com>
 Voice of America - <http://www.voanews.com>

References:

- [1] Pew Research Center, Pew Research Center Biennial News Consumption Survey: *Online News Audience Larger, More Diverse – New Audiences Increasingly Politicized*. June 8, 2004.
- [2] National Science Board, *Science and Engineering Indicators – 2002*. Arlington, VA: National Science Foundation, 2002 (NSB-02-1).
- [3] National Science Board. 2004. *Science and Engineering Indicators – 2004*. Two Volumes. Arlington, VA: National Science Foundation, 2004 (NSB-04-1(A))

Figure: (From left to right) Screen shots from various DBIS stories including: Metal Rubber, Man-Made Diamonds, Bug Breakthrough, and Molding Fingerprints.



Material Advantage Students Visit Washington

Tricia L. Niswonger

The Congressional Visits Day (CVD), sponsored by The Federation of Materials Societies (FMS) and the Material Advantage Student Program, is an event that gives students and faculty an exciting opportunity to visit on Capitol Hill with members of the U.S. Congress and congressional staffers from their own states. The 2007 event was held March 19–20. The goal of the event is to educate Congress about the importance of research in materials science, engineering, and manufacturing and the need to increase federal R&D funding. Approximately 60 Material Advantage students and faculty from 11 schools from around the country journeyed to Washington to participate.

CVD kicked off with a half-day orientation session to prepare the students for their visits with the legislators. A federal budget overview as well as a session on how to communicate effectively with congressional staff were two of the topics during the orientation. In addition, members of two panels, one focusing on the administration and the other on Congress, were available to answer questions before students headed to the Hill.

Training presenters included:

- Kei Koizumi, director, R&D Budget & Policy Program for the American Association for the Advancement of Science.
- Dan Byers, deputy associate director, Office of Science & Technology Policy.
- Lance Haworth, director, Div. of Materials Research, NSF.
- Raymond Orbach, undersecretary for science, DOE.
- William Jeffrey, director, National Institute of Standards & Technology.
- Jim Turner, chief counsel, House Committee on Science & Technology.

- Julia Jester, legislative assistant, office of Representative Vern Ehlers (R-MI).
- Colleen Shogan, legislative assistant, office of Senator Joe Lieberman (I/D-CT).
- Jack Wells, science fellow, office of Senator Lamar Alexander (R-TN).
- Deborah Koolbeck, policy advisor, Healthy Families & Communities Subcommittee, House Education & Labor Committee.

After the orientation session, students and faculty were divided into teams and, before heading to appointments with various legislators for the remainder of the afternoon, “practiced” the presentations that they would make. Later, in addition to meeting with congressional leaders, students had the opportunity to meet with leaders of scientific agencies and societies and attend congressional hearings.

The students finished the first day by attending the Materials Education Showcase, a grand display of exhibits that encouraged co-mingling of Congressional members, students, faculty, staff and exhibitors. Organized by the Federation of Materials Societies, this showcase included demonstrations, media displays, and poster representations of the community efforts that expose young people to the wonders and opportunities in science, technology, engineering and mathematics education using materials science and technology examples.

On the following morning, more congressional visits occurred followed by a wrap-up luncheon and evaluation session at Pizzeria Uno in Washington’s landmark Union Station.

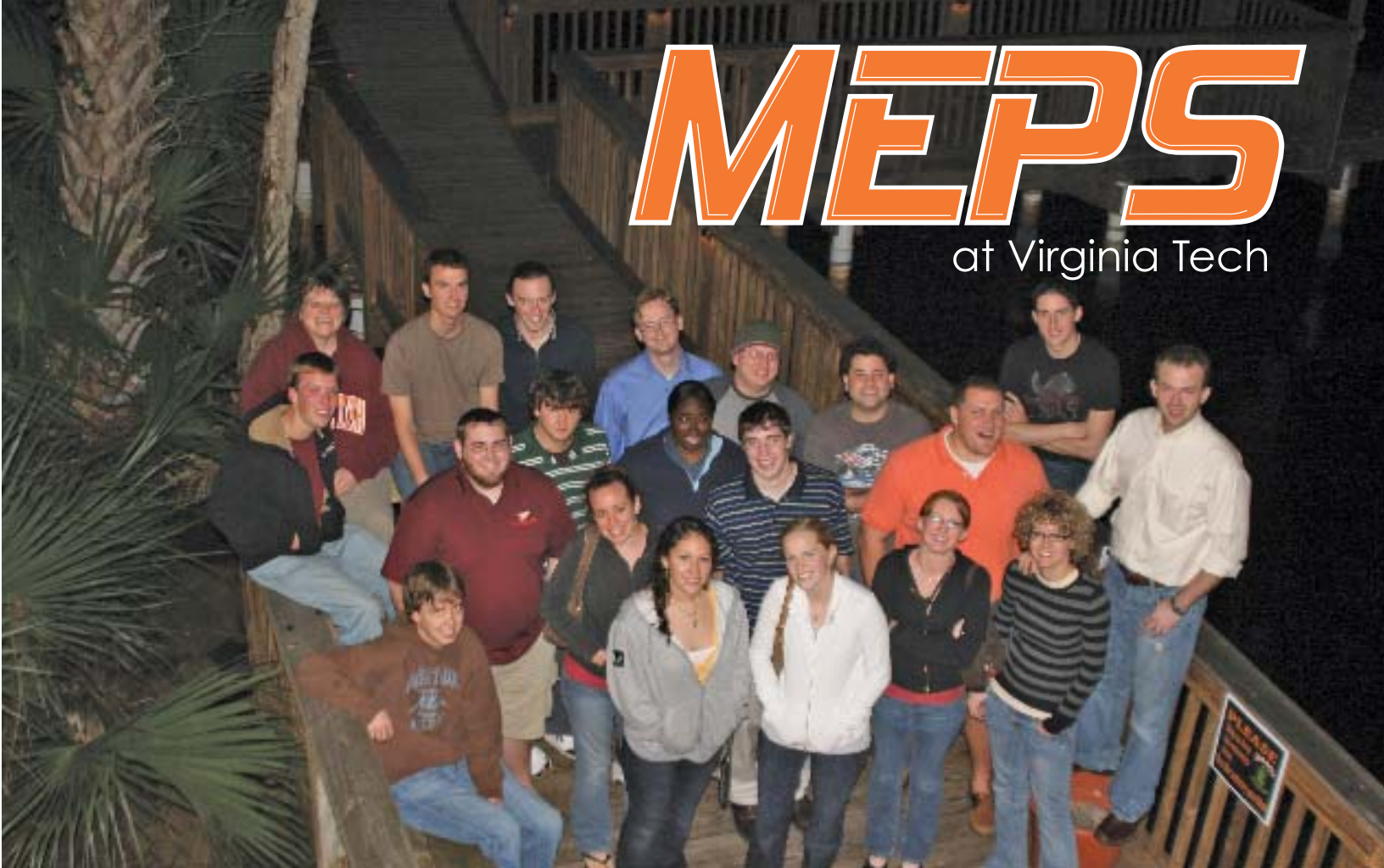
About the Author

Tricia L. Niswonger is The American Ceramic Society liaison to the Material Advantage Student Program.

**Published with Permission; First published in May 2007 issue of The American Ceramic Society Bulletin.*

MEPS

at Virginia Tech



The Materials Engineering Professional Societies (MEPS) is an academic and social organization run by the MSE student body at Virginia Tech. Each year, MEPS members represent the VT MSE department during professional conferences and Congressional Visits Day.

Additionally, MEPS hosts guest speakers and sponsors various field trips throughout the year. The organization also helps recruit interest in MSE through open houses and various outreach events. Socially, MEPS participates in numerous activities, such as intramural softball, bowling tournaments, and football tailgates for the College of Engineering.

Materials Science and Engineering
discover what we're made of...

The Journal of Undergraduate Materials Research (JUMR) hosted a symposium at the Materials Science and Technology conference in Detroit, Michigan on September 17, 2007. The symposium was created for undergraduate student presentations related to materials science and engineering. Participating schools included:

- Florida International University
- Virginia Tech
- University of Connecticut
- University of Missouri-Rolla
- University of Pittsburgh
- University of Washington
- Washington State University



Additionally, Dr. Uma Venkateswaran from the National Science Foundation discussed numerous research opportunities for undergraduates to pursue. The symposium was an excellent opportunity for undergraduate students to present their research, and JUMR looks forward to hosting another symposium at MS&T'08 in Pittsburgh.



Speakers and session chairs at the MS&T'07 JUMR symposium

University of Wisconsin-Madison Department of Materials Science and Engineering

The Department of Materials Science and Engineering at the University of Wisconsin-Madison is a dynamic community of outstanding faculty, dedicated educators and talented students. The department has had several names and has offered several different degrees since its founding in the mid 1800s. Until the mid-1990s, the BS in Metallurgical Engineering had been the primary degree offered. A BS degree in Materials Science and Engineering is now offered.

There are 16 faculty who teach materials science and engineering courses in the department to about 60

undergraduate students. Thus, our class sizes are small, and our faculty and staff know the students. There is opportunity for the undergraduate students to work in faculty members' research labs. There is a well established Co-

op Education/Internship Program through which students can get valuable industrial experience as an undergraduate.

There are many undergraduate scholarships

available including the Frank Worzala Memorial Scholarship, the Pat and Dick Moll Scholarship, the Tiemann Scholarship, and the Harry M. Clarke Scholarship.



Boise State University College of Engineering

Materials Science and Engineering is a dynamic field that is arguably one of the most important engineering disciplines. Materials Engineers combine material properties and structures with fundamental knowledge to optimize and develop materials.

Materials such as metals, ceramics, polymers, semiconductors, and composites are part of our everyday lives. Materials Engineers strive to improve such materials by studying the following:

- extraction of materials from natural and recycled resources,
- selection of appropriate materials for a given application,

- performance analysis of materials in use,
- investigate modes of failure,
- behavior of materials under various conditions,
- manufacture new products from raw materials.

Materials Science and Engineering is an interdisciplinary field. Physics, chemistry and engineering sciences are core concepts needed to study a material's structure

and properties in order to develop materials that meet the demands of modern technology. Many other university departments and affiliate faculty are involved and support the MSE program and research topics.



Structural Assessment of an Internal Fixation System for a Forearm Long Bone Mid-shaft Fracture

MyKal Woody

Savannah State University, Department of Engineering Technology
3219 College St. Savannah, GA 31404

Abstract

A novel low cost manufacturing method for bone replicas is developed in order to provide cross sectional geometry for 3-D modeling. A Finite Element Analysis (FEA), based on this geometry, is used to predict stress distributions in the radius with and without an internal fixation device attached. The changes in stress distribution under tensile and torsional loads are quantified and agree well with predictions in current literature where more expensive modeling techniques are used. Normal stresses near the radial cortex are seen to be higher with the fixation device, however stress gradients are substantially steeper resulting in lower tensile stresses with decreasing as radial distance. Shear stress minimum values increase with the presence of the plates and do not reverse direction as is the case with the un-plated radius. Stress shielding effects due to the plates and stress concentrations due to the holes are observed to significantly affect stress magnitude and distribution in the radius bone with a fixation device. The results from this research support the conclusion that fixation devices leave bones more susceptible to future injury.

Keywords: Internal Fixation, Radius, Finite Element, fracture, repair

1. Introduction

Accidents and their resulting injuries are everyday occurrences. For persons with physically demanding careers (athletes, construction workers etc.), the occurrence and severity of these injuries are higher than normal. The radius is one of two long bones (the other being the ulna) in the forearm which transmit and distribute loads from the wrist to the elbow. A typical mid-shaft fracture is repaired using Dynamic Compression Plates (DCP) as shown in Figure 1. The DCP system provides compressive stresses as well as stability at the fracture interface. These phenomena improve bone union and decrease external callus formation during healing. Once the fracture has fully healed, the ability



Figure 1. Dynamic compression plate applied to an ulna mid-shaft fracture (Reprinted with permission from *Wheeless Textbook of Orthopedic Surgery*)

of the forearm to fully function may be reduced due to the presence of the plate and/or screws, improper union, or callus formation. If the patient requires full use of the forearm for his or her career, inadequate forearm function after surgery and bone healing may potentially trigger a lawsuit against the operating surgeon or group. This may occur even if the patient was advised of potential surgical complications prior to surgery. More importantly, substantial loss of forearm

use may significantly reduce the quality of life and health of the patient. It is therefore essential to understand the internal changes in the bone that may occur if plates are retained after the bone has healed.

1.1 Other Literature

When modeling bones for testing, several variables need to be considered. Martin^[1] presented a mathematical model that could be histologically measured and related to the mechanical properties which determine bone function. The model aided in studying phenomena such as Wolff's Law^[2], regional acceleratory phenomena, and fluorochrome label escape errors. Properties of the trabecular bones were treated as variables in this work. By comparing prism and cube-based cell types, Kowalczyk^[3] parameterized elastic properties for the trabecular bone as FE models. Other literatures published on the subject of fixation devices have analyzed their performance. Gardener et al.^[4] characterized the stiffness of the Orthofix DAF (Dynamic Axial Fixator), an external fixation device, using a mathematical stiffness matrix. The analysis provided the means of analyzing inter-fragmentary motions that arise from physiological loading, regardless of complexity. Conjunctly, Claes et al^[5] provided a complete description of fixation stiffness needed to predict inter-fragmentary movement and potential effectiveness of device configurations. Results from the above investigations may provide insight into the FE results of this work on long bone performance with fixation devices.

1.2 Overview

In this work, Finite Element (FE) models of the radius and ulna bones with and without fixation devices are developed. The radius and ulna are restrained at the proximal ends and loaded at the distal ends in tensile and torsional modes. The load types used in the FE model simulate typical forearm usage during daily activity.

An inexpensive manufacturing method is also developed for suitable radius and ulna replicas. The replicas, made from lightweight plaster, are derived from geometrically correct plastic models. The method employs a manual counterpart to the cat scanning technique in order to obtain 2-D images to be extruded into a 3-D model.

2. Procedure

2.1 Manufacturing Method

This research introduces a cost-efficient way to replicate and transfer the radius and ulna geometry into CAD software. The process utilized Woodland Scenics lightweight Hydrocal, modeling clay, and talcum powder to create the bone replicas. In order to prevent adherence of clay to bone, the bone was lightly powdered with talcum powder. Modeling clay was then wrapped around the bone leaving the most irregularly shaped end of the bone exposed. With a scalpel the modeling clay was carefully cut in two halves. Once the bone was removed from the clay, both halves were evenly pressed together. The process

is repeated for the irregularly shaped end in order to obtain a full sized replica. Figure 2 shows an exploded view of the long bone enclosed in two clay molds.

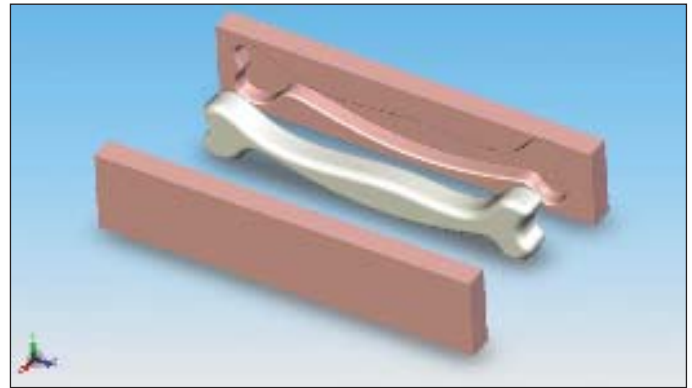


Figure 2. Clay molds and plastic bone used to create replicas

2.2 Replication of the Bone Model

The Hydrocal mixture was created by adding water to the powder in a 3/5ths mixture of water to powder. This resulted in a softer material upon curing such that slicing could be accomplished successfully. Once the paste was poured into the mold, air bubbles were removed by lightly shaking it. The model was then allowed to dry overnight in an upright position. The replicas were cut into one-inch sections and marked with a T on the tops for orientation purposes. All cross sectional slices were scanned in order to provide 2-D images to be imported into a 3-D modeling software package (SolidWorks). Some of these cross sections are shown in Figure 3. The conversion factor for the model was created by dividing the actual measurement of the marker by the measurement of the marker in SolidWorks. A measurement of the marker in SolidWorks was obtained by measuring it with a line segment.

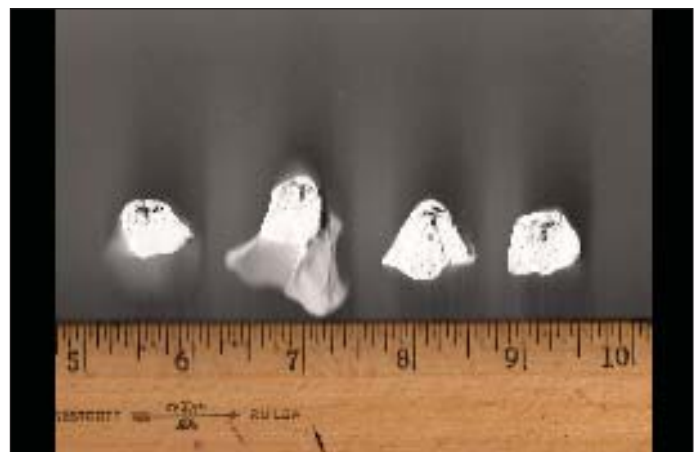


Figure 3. Scanned cross sectional slices for the radius model

Once all images were imported into SolidWorks and properly scaled, splines were sketched along their perimeters in their respective planes. Each plane was separated by one inch. To make the cortical and trabecular parts of the bones, the basic radius was copied three times. All of them were converted into either the cortical bone, left-end of the trabecular bone, or right-end of the trabecular bone. The original sketches were copied and resized to one fourth of their original size at the ends of the cortical bone and the area in the middle was reduced by half of the original size. Each cross-sectional sketch was extruded by 0.2mm to create profiles for lofting.

Screws were made in a similar fashion. The head of the screw was created from sketches of concentric circles that were lofted together. The top circle has a diameter of 5.0mm, the middle 6.0mm, and the bottom 3.5mm. By extruding the bottom circle to another circle 18.0mm below it, the shaft was created. Threads for the screw are created using the cosmic thread command and the 3.5mm circle at the end of the shaft.

The plates for the fixation device were created by extruding a rectangular sketch 3.3mm. Six circles were sketched on the plane on the top face of the plate. These circles were in two groups, starting 10.4mm from the (proximal/distal) ends of the plate and spaced an additional 10.4mm apart from each other. Each circle was cut-extruded through the plate and lined with the threads using the cosmic thread command.

3. FE Model

3.1 Numerical Properties

Separate models of the radius with and without an attached DCP fixation system were developed. The plate and screws were modeled as being perfectly bonded to the bone as well as each other, therefore no relative movement between bone and plate was allowed. The cortical bone was modeled as isotropic, while the trabecular bone was modeled as an orthotropic material. The Young's modulus and Poisson's ratio values used for the cortical bone were respectively, 11.4 (MPa) and 0.29.^[6] Trabecular bone material properties in their respective x, y and z-directions were: Elastic Modulus, 239 MPa, 309 MPa, 823 MPa; Poisson's ratio 0.169, 0.063, 0.423; and Shear Modules, 73 MPa, 134 MPa, 112 MPa.^[7]

A semi-course mesh with solid tetrahedral elements was used for both models. The plated model consisted of 37,222 elements while the un-plated model consisted of 25,000 elements. The elements used were Jacobian in order to compensate for the nodes that contact on irregular edges. Bones were restrained at their proximal end under a cantilever condition. A 10N force was applied at the distal end for all bones. The force was applied axially in order to simulate a tensile load. A 1 N.m couple was also separately applied at the distal end in order to

simulate a torsional load. The 3-D plated radius model used in the FE analysis, as well as a plated ulna model also developed, is shown below in Figure 4.

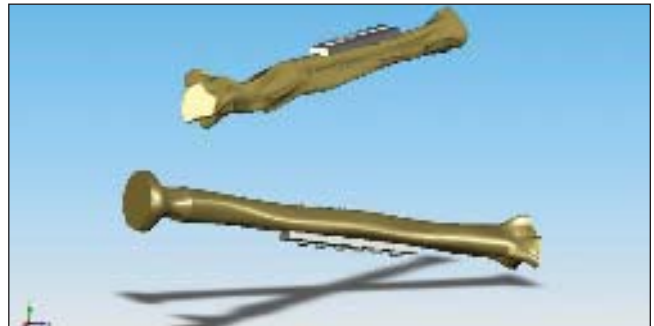


Figure 4. FE model of plated radius and ulna bones

3.2 FE validation

The mesh size was varied between course and fine to check for convergence. It was observed that stress results did not vary substantially with mesh sizes finer than the semi-course mesh used. Additionally, an FEA of a hollow cylinder was developed using the same type of element and approximately the same number of elements. The tube was modeled using cortical bone properties only. Stress results for the cylindrical tube under tensile and torsional load agreed well with theoretical calculations.

4. Results & Discussion

All results obtained from the FE analysis are graphed as stress vs. distance, measured from the surface inward towards the center of the bone. These graphs capture the local changes in the stress along planes transverse to the bone's longitudinal axis. They also allow for observation of general trends in the stress distribution which may have arisen due to the presence of the plates.

4.1 Tensile Load Results

For descriptive purposes, we will define the most proximal screw as the "first" screw position. Figure 5 shows a plot of the normal stress distribution along three transverse planes (series 1-3) for the plated bone. The 1st plane (series 1) is located on the proximal side of the first screw position; the second plane (series 2) is between the first and second screw, and so on. Figure 6 shows a similar plot for the un-plated radius. Based on Figures 5 and 6, the presence of the fixation device results in initially higher stresses near the cortex, however there is a substantial drop in these magnitudes at locations further inward. Normal stress values drop by as much as 80% at approximately 12mm from the cortex of the plated bone (Figure 5). Conversely, there is little or no normal stress reduction in the plated bone at

corresponding locations (Figure 6). It can also be observed that the difference in the normal stress values at equidistant points (from the longitudinal axis) on different planes is substantially smaller for the plated bone. For example, near the surface of the un-plated bone ($x = 0$), the normal stress values differ by as much as 26% (series 2 vs. series 3), while the plated values maximum difference is approximately 7% at $x = 0$.

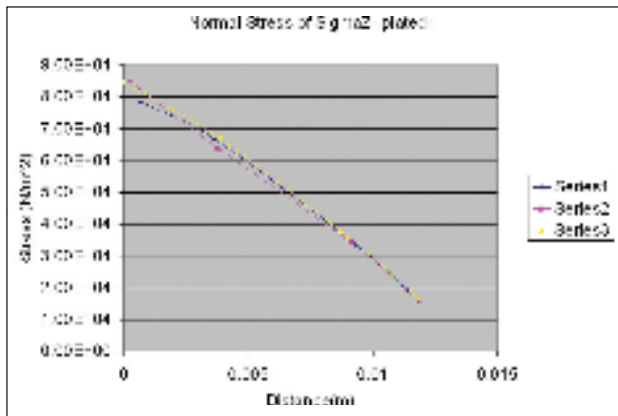


Figure 5. Normal stress distribution: plated radius under tensile load

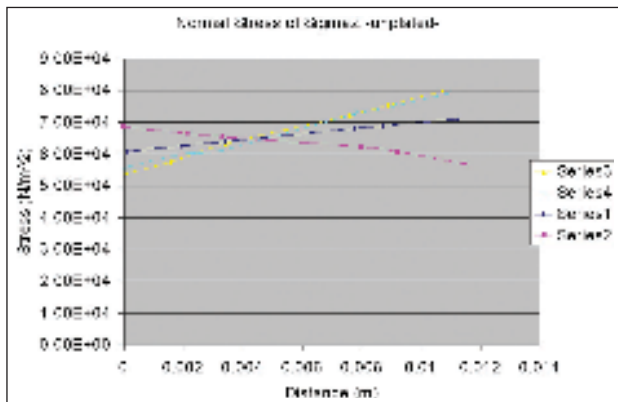


Figure 6. Normal stress distribution: un-plated radius under tensile load

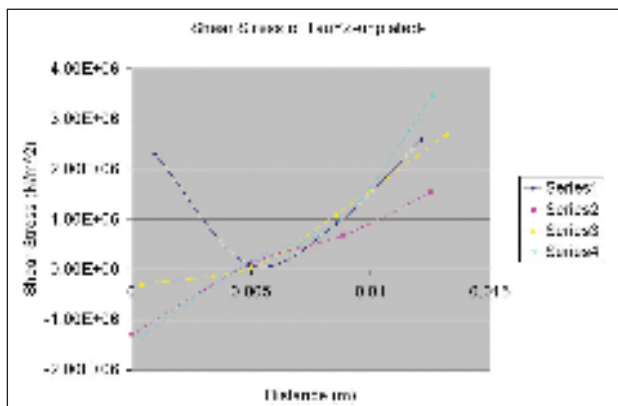


Figure 7. Shear stress distribution: un-plated radius under torsional load

4.2 Torsional Load Results

Figures 7 and 8 show the shear stress distribution along the same planes (defined in section 4.1) for the un-plated and plated bones respectively. The graphs show that the absolute values of the shear stresses in the un-plated and plated bones decrease to minimum values around 5 mm from the cortex and then increase further inward. The shear stress values and trends do not appear to change substantially with the presence of the fixation device. However, the plates do increase the minimum shear value (absolute) attained along the planes furthest from and closest to the applied load. Additionally, once this minimum value is attained, the shear direction is observed to reverse along three planes in the un-plated bone (series 2-4, Figure 7). This reversal only occurs on one plane in the plated bone (series 2, Figure 8). For the plated bone, the shear stresses along the planes closest to and furthest from the applied load do not reverse direction with increasing distance inward.

5. Conclusion

The decreased normal stress with the presence of the plates supports the concept of stress shielding advocated by many authors.^[8, 9] Stress shielding implies that the plate takes some of the load away from the bone. The consequences of stress shielding however may be detrimental to bone strength as bone will remodel and adapt to the level of stress that is placed on it (Wolff's law). The steep stress gradients created due to the presence of the plates may also result in high density or strength gradients. This fact should be of concern to patients and surgeons as this increases the likelihood of micro-cracks during strenuous repetitive activity. Since the model did not account for slippage between plate and bone, it is a conservative one. Relative slippage would introduce added shear stress near the cortex and contact stresses, which may affect bone vascularity.^[10] These FE results indicate that plate retention after the fracture has healed may result in a bone that is more susceptible to micro-cracks and reduced density in the vicinity of the plates.

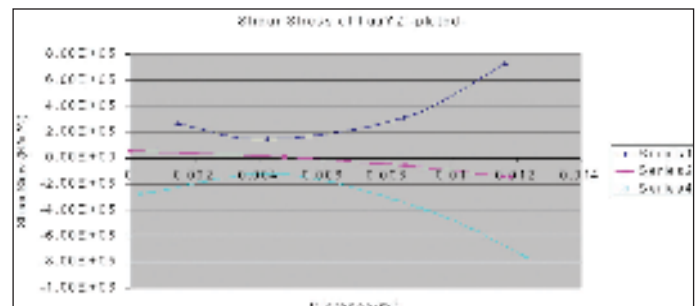


Figure 8. Shear stress distribution: plated radius under torsional load

Acknowledgments

This research was performed at Armstrong Atlantic State University (AASU) as a component of the Minority Access to Graduate Education and Careers in Science, Technology, Engineering, and Mathematics (MAGEC-STEM) program at Savannah State University (NSF grant #0310328). I would like to thank my research mentor, Dr. Cameron Coates, of AASU, for his supervision of this project and am also grateful to the Georgia Space Grant Consortium for providing partial funding for this work.

References

- [1] Martin, R.B. The Usefulness of Mathematical Models for Bone Remodeling. *YearBook of Physical Anthropology* **1985**, 28(S6), 227-236.
- [2] Pearson O. M.; Lieberman D.E. The Aging of “Wolff”s Law”: Ontogeny and Responses to Mechanical Loading in Cortical Bone. *YearBook of Physical Anthropology* **2004**, 47, 63-69.
- [3] Kowalczyk, P. Elastic properties of Cancellous Bone Derived from Finite Element models of parameterized microstructure cells. *Journal of Biomechanics*. **2003**, 36(7), 961-972
- [4] Gardner, N. T.; Weemaes, M. A mathematical stiffness matrix for characterising mechanical performance of the Orthofix DAF. *Medical Engineering & Physics* **1999**, 21(2), 65-71
- [5] Claes, L.; Duda, N. G.; Wilk H.; W. Helmut, K. A Method to Determine the 3-D Stiffness of Fracture Fixation Devices and its Application to predict Inter-fragmentary Movement. *Journal of Biomechanics*. **1997**, 3:31, 247-252.
- [6] Tencer .F. and Johnson K.D. *Biomechanics of Orthopedic Trauma*; Martin Dunitz Ltd: London; 1994; pp. 31.
- [7] Keveany T.M.; Morgan E.F; Niebur .L.; Yeh O.C. Biomechanics of Trabecular Bone. *Annual Review in Biomedical Engr.***2001**, 307-33.
- [8] Ganesh, V.K.; Ramakrishna K.; Ghista, D.N. Biomechanics of bone-fracture fixation by Stiffness-graded Plates in Comparison with Stainless-Steel Plates. *Biomedical Eng Online* 2005, 4, 46.
- [9] Cheal E.J.; Hayes W.C.; White III A.A.; Perren S.M. Stress Analysis of Compression Plate Fixation and its effect on long term Remodeling. *Journal of Biomechanics* **1985**, 18, 141-150.
- [10] Perren, S.M.; Cordey J.; Rahn B.A.; Gautier E.; Schneider E. Early Temporary Porosis of Bone Induced by Internal Fixation: A reaction to neurosis, not to stress protection. *Clinical Orthopedics and Related Research* **1988**, 232, 139-151.

About the Author

Mykal is a sophomore at Savannah State University majoring in mechanical engineering with a minor in engineering management. Mykal was born and raised in Atlanta, GA.

Mykal is a Minority Access to Graduate Education and Careers in Science Technology Engineering and Math (MAGEC-STEM) scholar. Mykal recently received 1st place for my oral presentation in the Peach State Louis Stokes Alliance for Minority Participation (PSLSAMP) Fall Forum and Research Conference.

Mykal intends to work as a mechanical engineer for a company that allows me to grow technically and provides increasing leadership responsibilities. Mykal plans to complete a Master’s degree in Engineering while working and eventually create and run an engineering business.

Biocompatibility and Hardness of Ti-Hf and Diamond-like Carbon Coatings for Orthopedics

Stephanie Kuhn

University of Wisconsin - Madison, Department of Materials Science & Engineering
1509 University Avenue, Madison, WI 53706

Abstract

Every year, about 300,000 total hip replacement (THR) surgeries are performed in the United States. The typical lifespan of an implant ranges between 10 and 20 years, with implant failures largely due to materials issues such as biocompatibility, wear, corrosion, and premature stress failures. The objective of this research is to examine the feasibility of using a new class of materials, namely Ti-Hf alloys and low friction diamond-like carbon (DLC) coatings, for improving the performance of orthopedic devices. Biocompatibility and hardness tests were performed, which showed Hf did not adversely affect the biocompatibility of Ti and that the DLC coating did not adversely affect the biocompatibility of the Ti-Hf alloy. Furthermore, the biocompatibility of the Ti-Hf alloy was comparable to that of Ti-6Al-4V. The research was done as a collaborative effort between the College of Engineering and the School of Veterinary Medicine at the University of Wisconsin – Madison and NASA Glenn, Cleveland, OH.

Keywords: biocompatibility, diamond-like carbon, hemocytometer, orthopedic, Ti-Hf

Introduction

Every year, about 300,000 total hip replacement (THR) surgeries are performed in the United States. The cost of a single procedure can exceed \$20,000.^[1] The most common recipients of THR's are between the ages of 65 and 70; however, it is becoming more prevalent in the younger demographic.^[2] The durability of a THR, is in the range of 10 to 20 years depending on the patient's age, weight, and physical activity. One of the major issues associated with THR's is that retrieval surgeries are often needed to replace corroded, worn, or fractured parts from the original implant. These procedures tend to be more expensive and debilitating. The orthopedics industry aspires to

extend the life of the implant and has concentrated on developing new materials and surface modifications that are more biocompatible and corrosion and wear resistant, as well as those that exhibit high strength.

A THR consists of three main components, the acetabular cup, femoral head, and femoral stem, which can be seen in Figure 1. The acetabular cup is polymeric and is usually made of ultra high molecular weight polyethylene (UHMWPE). The femoral head and stem are metallic and usually made of either Co-Cr or Ti-6Al-4V alloys.

Figure 1 summarizes some of the issues and their respective locations on the implant. There is significant wear at the poly-

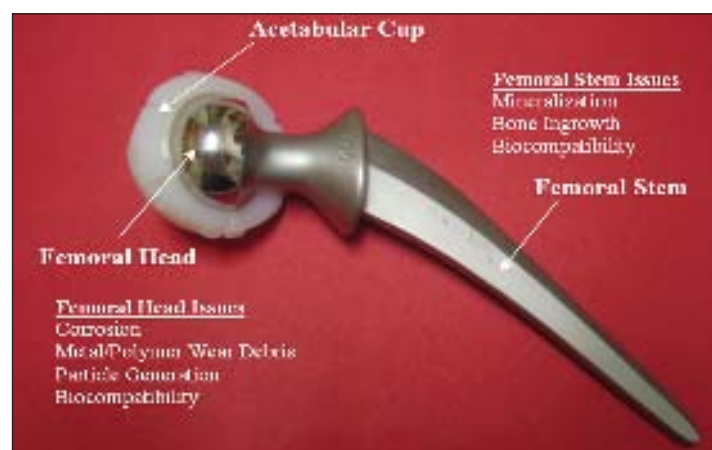


Figure 1. Components of a THR

mer/metal interface. The alloy used for the femoral head is significantly harder than the polymer used for the acetabular cup. This causes the generation of wear particles up to about 5µm in size, thus causing adverse tissue reactions. The rate of wear can range from 0.1 to 0.5 mm per year depending on the weight and activity of the patient.^[3] Fibrosis, an immune response eliciting fibroblasts to combat foreign objects inserted in the body, is well-researched in the orthopedics industry.^[4] Fibroblast cells are widely used in medical device research (ATCC), so 3T3 mouse fibroblasts were selected for biocompatibility testing.

The materials used for orthopedic implants must be biocompatible as well as exhibit good wear and corrosion resistance. Material selection is only part of the issue concerning biocompatibility and implant longevity. Surface modifications are also being studied as a means of reducing friction, minimizing wear, and promoting bone ingrowth. Research has shown that diamond-like carbon (DLC) coatings reduce polymer wear and increase corrosion resistance in synovial fluid, the body's natural lubricant.^[5] DLC is a composite of carbon in the graphite and diamond states, which has a low friction coefficient and high hardness, and would be deposited on the femoral head.^[6] The biocompatibility and hardness of Hf and DLC coatings were assessed via biological testing and hardness measurements. Table 1 lists the materials that were used for testing.

1. Materials Selection

The Ti-6Al-4V alloy was selected for evaluation because it is commercially used for THR's and exhibits good biocompatibility and strength-to-weight ratio. Aluminum and V are added primarily to increase the strength of Ti, but the toxicity of V is much greater than that of Ti.^[7] Therefore, V was chosen as a negative control, while Ti was chosen as a positive control for biocompatibility testing. Hafnium was selected for evaluation because, similar to Ti, it forms a passive oxide layer and is in the same group as Ti in the periodic table, thus likely to exhibit comparable properties. Furthermore, Hf is expected to increase the strength of Ti because of the large difference in atomic radii. Large solute atoms create localized stress fields, which impede dislocation motion, thus increasing the strength of the material.^[8] The Ti-Hf phase diagram shows very narrow two-phase regions, which implies that there is less

segregation upon solidification, and a lower tendency for galvanic corrosion. Limited studies have shown evidence that Hf is biocompatible when used as a coating for biomedical applications, but no studies were found for which Hf was used in the bulk material.^[9]

DLC coatings were selected for evaluation for the low friction coefficient in attempt to improve wear resistance.

2. Procedure

2.1 Sample Preparation

The metallic samples varied in surface roughness R_a , weight, and surface area; therefore, they had to be polished to a comparable R_a value in order to eliminate that variable during testing. The samples were polished according to the procedure outlined in Table 2. Weight was a non-issue since the biocompatibility test protocol, created in part of the research project, requires the cells be seeded on top of the surface of interest. The total surface area was taken into consideration when analyzing the cell viability results.

Materials for Biological Testing		
Initial	Material Research	Surface Modification Research
Ti	20wt%Hf-80wt%Ti	20wt%Hf-80wt%Ti
V	Ti-6Al-4V	
Hf		

Table 1. Materials for biological testing

Sample Preparation Procedure									
Material	Pretreatment	Mount	Remove from Mounting Press	Polish					Colloidal Silica
				SiC Paper					
				320	400	600	800	1200	
Ti	Roughen sample surface (convex side up) with 180 SiC	Phenolic Mounting Powder T = 133-149° C P = 29 MPa Premold = 5 min Mold = 10 min	Immediately	N/A	N/A	N/A	X	X	X
V			Immediately	N/A	N/A	N/A	X	X	X
Hf			After 30 min.	N/A	N/A	N/A	X	X	X
80%Ti-20%Hf	N/A		Immediately	X	X	X	X	X	X
60%Ti-40%Hf	N/A		Immediately	X	X	X	X	X	X
40%Ti-60%Hf	N/A		Immediately	X	X	X	X	X	X
20%Ti-80%Hf	N/A		Immediately	X	X	X	X	X	X

Table 2. Sample preparation procedure

The samples were then removed from the mounts and ultrasonically cleaned in acetone and ethanol for 3 mins each. Profilometry measurements were performed to ensure that the surface roughness was comparable (0.05 – 0.1 μm) for all samples.

2.2 Knoop Microhardness

Knoop microhardness measurements were performed for the Ti-Hf alloy and Ti-6Al-4V at a 50g load for 12 seconds.

2.3 Diamond-like Carbon Thin Film Deposition

Plasma Immersion Ion Implantation and Deposition (PIIID) technology, pioneered at the University of Wisconsin – Madison in the late 1980's, was used to coat Ti-Hf alloy samples. An Ar plasma cleaned the surface of the sample, and was followed by an acetylene (C_2H_2) plasma, which created a DLC film, with a 0.5 μm thickness, on the substrate (Figure 2).^[10]

2.4 Cell Cultures

The samples were individually packaged and placed in an autoclave chamber at 125°C for one hr, to be sterilized prior to *in vitro* testing.

The cells were seeded on the surface of a flask and about 20 mL of growth medium was added to cover the bottom of the flask, and changed every two days. Growth medium is a solution containing essential nutrients for cell growth, and consisted of Dulbecco's Modified Eagles' Media with 2 mM glutamine, 25 mM HEPES buffer, 1% non-essential amino acids, 10% fetal calf serum, 50 mgL^{-1} ascorbic acid and supplemented with 1%

penicillin/streptomycin antibiotic.^[11,12] The flask was placed in an incubator at 37°C and 5% CO_2 for one week or until cells became confluent. Confluent cells grow as a monolayer to cover the surface of the flask. The 3T3 mouse fibroblast cell line is categorized as adherent, indicating that the cells grow on a substrate, and not in suspension. In order to transfer the cells from one substrate to another, they had to be trypsinized. Trypsin is an enzyme that breaks down the proteins that bind cells to a substrate, thus suspending them in the growth medium allowing them to be transferred. The Biocompatibility Test Protocol, outlined in Appendix I, was developed and carried out for each sample.

3. Results and Discussion

3.1 Knoop Microhardness

Figure 3 shows that the hardness of 80Ti-20Hf is comparable to that of Ti-6Al-4V. Five measurements were taken for each sample and an error of ± 1 standard deviation was assessed for each sample. There is a large error bar associated with Ti-6Al-4V, and it is most likely attributed to the presence of multiple phases that vary in hardness. Conversely, Ti-Hf has a much smaller error bar, which can be attributed to the single phase microstructure.

3.2 Cell Cultures

Figure 4 shows that the biocompatibility of Ti is much greater than that of V, which confirms that the test methods were rigorous enough to adequately differentiate between Ti and V, as well as the Ti-Hf alloy

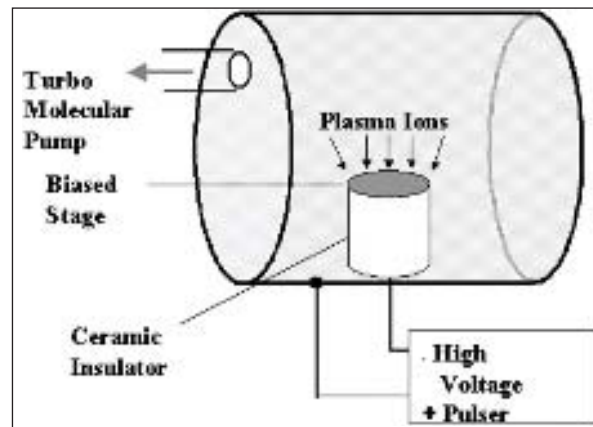


Figure 2. Plasma immersion ion implantation and deposition (PIIID)^[10]

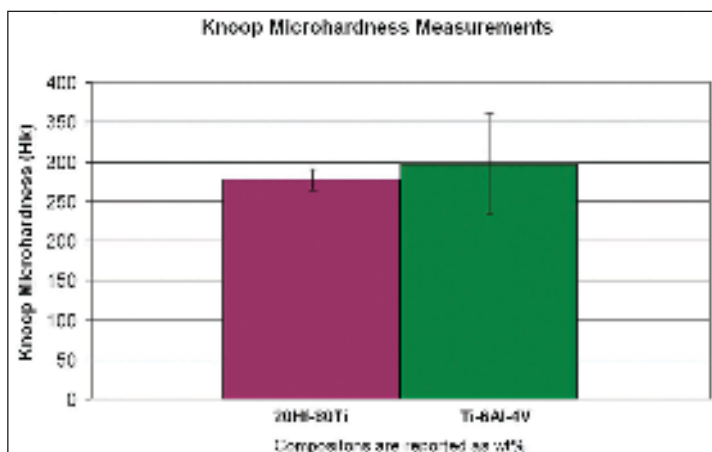


Figure 3. Knoop microhardness measurements

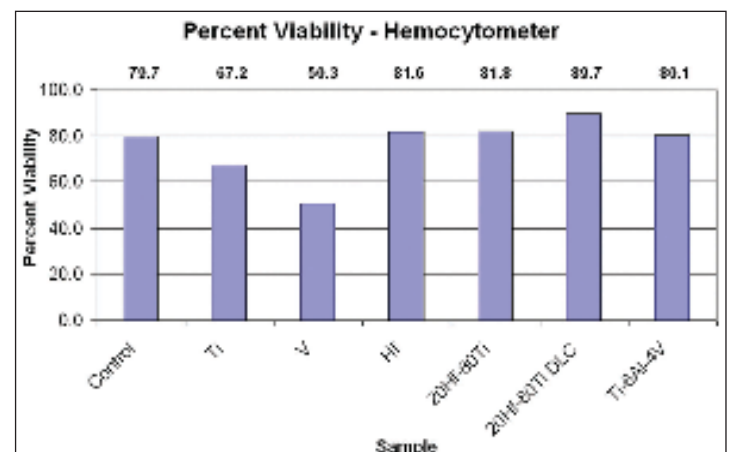


Figure 4. Percent viability - hemocytometer

and the other samples. The biocompatibility of the Ti-Hf alloy is comparable to that of Ti, which means that Hf does not adversely affect the biocompatibility of Ti. The biocompatibility of the DLC coated Ti-Hf alloy is comparable to that of the non-coated alloy, which indicates that DLC coatings do not adversely affect the biocompatibility of the bulk material. Lastly, the biocompatibility of both the DLC-coated and non-coated Ti-Hf was comparable to Ti-6Al-4V.

4. Conclusions

A protocol was established for testing the biocompatibility of metallic materials, and can be used for future work with considerable efficiency. Cell viability results from the hemocytometer showed that Hf does not adversely affect the biocompatibility of Ti. Similarly, DLC coatings do not adversely affect the biocompatibility of Ti-Hf alloys, suggesting that DLC coatings have the potential to be used along with Ti-Hf to improve wear resistance, thus minimizing the likelihood of adverse tissue reactions. The biocompatibility of the DLC-coated and non-coated Ti-Hf alloys were comparable to that of Ti-6Al-4V, proving these materials could potentially be used in orthopedic applications. Hardness measurements showed that Hf strengthens Ti via solid-solution strengthening, which could minimize stress-related failures in an orthopedic implant.

5. Future Work

This research covers the initial steps in exploring the potential use of Hf and DLC in orthopedic applications. Further testing should be done on a large sample set to establish statistical viability at a 24 hr incubation time. It would be beneficial to examine the long term effects of these materials on biological systems and to establish biocompatibility with respect to other relevant cell lines. Finally, *in vivo* biocompatibility testing would be another option for future research.

Appendix I: Biocompatibility Test Protocol

1. Growth medium was disposed and confluent cells from four flasks were trypsinized (5 mL/flask) for 10 mins.
2. Trypsinized cells were collected into a 50 mL tube and 15 mL growth medium was added.
3. The tube was placed in a centrifuge set to 23°C and spun at 1600 rev/min for 10 mins to produce a cell pellet.
4. Excess medium/trypsin was decanted and the cell pellet was separated.

5. 2 mL growth medium was added to the 50 mL tube and mixed.
6. A 1:5 trypan blue dilution (dilution factor = 5) was used to count the number of living cells/mL to determine the volume required so that each test well contained 5×10^5 cells.
 - a. 10 μ L cell/growth medium solution and 40 μ L trypan blue was pipetted into a 1.5 mL tube and mixed thoroughly.
 - b. 20 μ L was pipetted onto a hemocytometer slide and the viable cells were counted (cell count = 81 cells).
 - c. Equation 1 was used to determine the number of cells/ μ L (4.05×10^3 cells/ μ L).

$$\text{No. of cells / } \mu\text{L} = \text{cell count} \cdot \text{dilution factor} \cdot 10 = 4.05 \times 10^3 \text{ cells / } \mu\text{L} \quad (1)$$

- d. Equation 2 was used to determine the volume to be pipetted into each well to total 5×10^5 cells (123 μ L/well)

$$\text{Volume of cells / well} = \frac{\text{number of cells desired}}{\text{number of cells / } \mu\text{L}} \quad (2)$$

7. An autoclaved metal sample was placed in a labeled test well and growth medium was added to cover the surface of the metal sample (Note: For those wells that did not contain a metal sample, growth medium was added to cover the surface of the plate).
8. 120 μ L cell/growth medium solution was pipetted into each well.
9. The plates were incubated for 24 hrs, followed by cell viability testing.
10. Growth medium (which may have contained dead cells that had detached from the substrate) was collected into a labeled 15 mL tube.
11. Cells were trypsinized for 10 mins (trypsin covered the surface of the substrate) and pipetted into the labeled 15 mL tube.
12. The tube was placed in a centrifuge set to 23°C and spun at 1600 rev/min for 10 mins to produce a cell pellet.
13. Excess growth medium/trypsin was decanted and the cell pellet was separated.
14. 250 μ L of growth medium was added to the tube and mixed thoroughly.
15. A 1:1 trypan dilution was used to count the number of live and dead cells/mL to determine the percent viability.
 - a. 10 μ L trypan blue and 10 μ L of cells/growth medium was pipetted into a 1.5 mL tube

and mixed thoroughly (the 15 mL tube was replaced on ice).

- b. 20 μ L was pipetted onto a hemocytometer slide and covered with a cover slip.
- c. The live and dead cells were counted and recorded.
- d. The hemocytometer slide and cover slip were rinsed and cleaned with ethanol.

Steps 7-15 were repeated for each metal sample.

Acknowledgements

This research was done at the University of Wisconsin – Madison as a senior design project, under the supervision of Dr. Kumar Sridharan and Dr. James Clum. It was a collaborative effort between the Materials Science and Engineering Department and the School of Veterinary Medicine in association with Dr. Peter Muir, Dr. Mark Markel, and Zhengling Hao. The metallic samples were provided by NASA Glenn, Cleveland, Ohio in association with Dr. Sai Raj.

References

- [1] Kelley, Raina. *Rebuilding Your Body*. *Newsweek*. July 10, 2006, pp. 93-94.
- [2] Zimmer – For Patient and Caregiver (U.S.). Frequently Asked Questions. <http://www.zimmer.com/z/ctl/op/global/action/1/id/8140/template/PC/navid/68>. Accessed September 2006.
- [3] Dearnaley, G. Diamond-like carbon: A Potential Means of Reducing Wear in Total Joint Replacements. *Clinical Materials* Vol. 12, No. 4, 1993, pp. 237-244.
- [4] Personal Communication with SVM. University of Wisconsin – Madison, School of Veterinary Medicine, 2015 Linden Drive, Madison, WI 53706. November 28, 2006.
- [5] Narayan, Roger. J.; Hobbs, Linn W.; Jin, Chunming; Rabiei, Afsaneh. The Use of Functionally Gradient Materials in Medicine. *Journal of Materials* Vol. 58, No. 7, July 2006, pp. 52-56.
- [6] Bares, J.A.; Sumant, A.V.; Grierson, D.S.; Carpick, R.W.; Sridharan, K. Small Amplitude Reciprocating Wear Performance of Diamond-Like Carbon Films: Dependence of Film Composition and Counterface Material. University of Wisconsin – Madison, Madison, WI, 2005.
- [7] Chandrasekaran, Margam; Zang, Su Xia. Effect of Alloying Time and Composition on the Mechanical Properties of Ti Alloy. *Materials Science & Engineering* Vol. 394, No. 1-2,

2005.

- [8] Material Science on CD-ROM, Version 2.1. Aluminum Alloys: Strengthening. <http://www.matter.org.uk/matscicdrom/manual/as.html>. Accessed May 2007.
- [9] Mohammadi, S.; Esposito, M.; Cucu, M.; Ericson, L.E.; Thomsen, P. Tissue Response to Hafnium. *Journal of Materials Science: Materials in Medicine* Vol. 12, No. 7, July 2001, pp. 603-611(9).
- [10] Sridharan, K.; Reeber, R.R. “Plasma Source Ion Implantation” *Advanced Materials and Processes*, 146, pp. 21-22, 1994.1.
- [11] Ball, M.D.; Downes, S.; Scotchford, C.A.; Antonov, E.N.; Bagratashvili, V.N.; Popov, V.K.; Lo, W.J.; Grant, D.M.; Howdle, S.M. Osteoblast Growth on Titanium Foils Coated with Hydroxyapatite by Pulsed Laser Ablation. *Biomaterials* Vol. 22, No. 4, 2001, pp. 337-347.
- [12] Carroll, W.M.; Rochev, Y.; Clarke, B.; Burke, M.; Bradley, D.J.; Plumley, D.L.; Proft, J. Influence of Nitinol Wire Surface Preparation Procedures, on Cell Surface Interactions and Polymer Coating Adherence. *Materials & Processes from Medical Devices Conference*; Anaheim, CA; USA; 8-10 Sept. 2003. pp. 63-68. 2004.

About the Author



Stephanie graduated with a Bachelor of Science in Materials Science and Engineering from the University of Wisconsin – Madison in the spring of 2007. During the summer of 2007, she plans to travel throughout Europe before returning to the U.S. to begin a full time career as an engineer at Kimberly-Clark Corp. in Roswell, GA.

Optical Properties of an Electrochromic Device Based on Poly (aniline 2-sulfonic) acid (PASA) Film, Formed by Ionically Self-Assembled Multilayers (ISAM) Technique

Reza Montazami

Virginia Polytechnic Institute and State University, Department of Physics
435 Robeson Hall, Blacksburg, VA 24060

Abstract

A new ElectroChromic Device (ECD) was designed and constructed based on Ionically Self Assembled Multilayers (ISAM) technique, in which oppositely charged polymers are used to construct films of multiple layers. The ECD device proposed and studied in this work was based on Poly (aniline 2-sulfonic) acid, (PASA), as the active electrochromic polyanion, and Poly (allylamine hydrochloride), (PAH), as the inactive polycation. Cyclic Voltammetry (CV) technique was employed to study redox properties of the polymer film and to help to determine the operating voltage of the device. It was determined that the PAH/PASA ECD has two redox states between -700mV and $+700\text{mV}$. The ECD with 40 bilayers demonstrated dark green to light brown to dark gray electrochromism, in the -700mV to $+700\text{mV}$ window. The major transmittance occurred at -600mV (dark green) and $+600\text{mV}$ (dark gray). The ECD in the relaxed state, i.e. no voltage applied, is light brown. At -600mV , in visible spectrum, the highest contrast ($\Delta T=27\%$) appeared at approximately 690nm (dark green) and at $+600\text{mV}$ the highest transmittance in visible range was a broad range between approximately 600nm to 710nm .

Keywords: Electrochromic, Ionically Self Assembled Monolayers, ISAM, Poly (aniline 2-sulfonic) acid, PASA

1. Introduction

ECDs are devices that are constructed of thin polymer film on conductive material. The polymer film reacts to voltage by changing color and/or optical density.

The color change is reversible by reversed voltage and it is because of the redox properties of the electrochromic polymer(s). When applying voltage, the electron flow will change the electronic structure of the electrochromic material by reducing or oxidizing it, this change in structure appears as a change in color and/or optical density. To date, some of the known applications of optical switching are seven-segment displays^[1], anti-glare mirrors^[2] and solar-attenuated windows^[3]. Other possible future application of ECDs is in flat panel displays.

In this work we report the electrochromic properties of Poly (aniline 2-sulfonic) acid, (PASA) which was used as a polyanion. Poly (allylamine hydrochloride), (PAH), a non electrochromic polyelectrolyte, was used as the polycation to help form the layers of polymer film. In forming the polymer film, we used one electrochromic polymer only; however two oppositely charged electrochromic polymers can also be used to form a polymer film. Such a device is called Complementary ElectroChromic Device, CECD.^[4,5] CECDs are expected to have more redox states compared to ECDs with just one electrochromic polymer. ISAM technique was employed to construct the polymer film on the substrate. In this method opposite charged polymers are used to buildup several layers of polymers on the Indium Tin Oxide (ITO) coated glass substrate. Due to the opposite charge

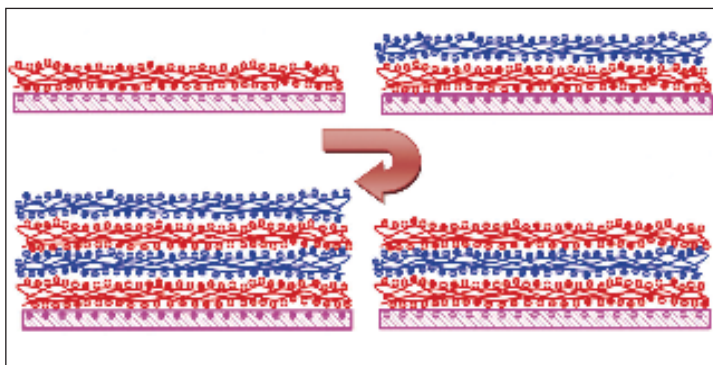


Figure 1. ISAM technique, layers of opposite charged polymers are used to construct the thin polymer film.

of neighboring layers, layers bind together to form the polymer film as shown in Figure 1.

ISAM technique makes it possible to have nanometer control on the thickness of the film. The formed films are very homogenous and smooth. Strong ionic interactions between cationic and anionic layers make very stable and robust films.

2. Procedure

2.1 Substrate

A 25mm x 75mm x 0.7mm unpolished float glass, SiO₂ passivated with ITO coating on one surface ($R_s = 8 - 12 \Omega/\text{sq}$) was used as the conducting substrate (Delta Technologies, USA). The non ITO surface and about 20 mm of the ITO coated side of the slide was covered by electrical tape to prevent any ISAM film deposition. Then the slide was cleaned with Acetone and washed with Deionized (DI) water and dried with nitrogen before the deposition of the ISAM film.

2.2 Solutions

All chemicals were reagent grade and were used as received. DI water was used throughout the entire solution preparation process. All chemicals were commercially available (Sigma-Aldrich, USA). 2mM PASA solution (pH 3) was used as polyanion and 10mM PAH (pH 9) was used as polycation. Both solutions are water based and freshly prepared prior to use.

2.3 Film Deposition

ISAM technique was used to deposit thin film of PAH (polycation) / PASA (polyanion) on the substrate. Substrate was washed with DI water prior to the deposition process to provide a negatively charged surface. Deposition was done at room temperature, using an automatic dipping machine.

To form the first bilayer the sample was: 1) exposed to PAH by spinning it in PAH bath for 4 minutes; 2) then washed in three steps, 45 seconds each, with DI water to wash off any

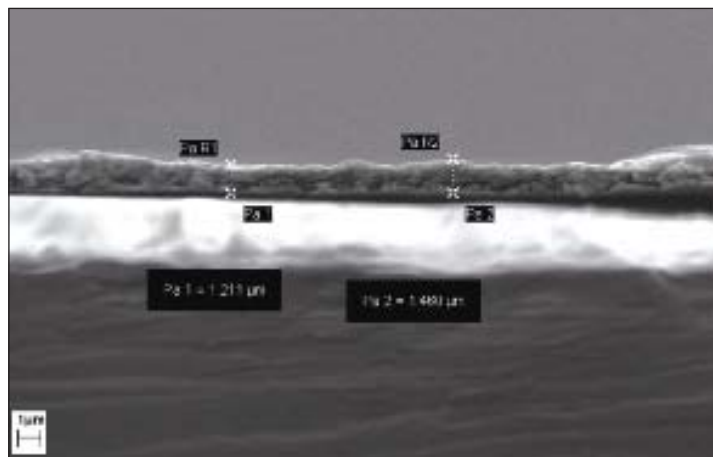


Figure 2. SEM image of 40 bilayers of PAH / PASA on ITO

loosely bound PAH molecules. After forming the first monolayer, the sample was; 3) exposed to PASA by spinning it in PASA solution for 5 minutes and then; 4) washed with DI water in three steps, 45 seconds each, to remove any loosely bound PASA molecules. These four steps were to form one bilayer, consist of one polycation and one polyanion layer. This process was repeated 40 times to form a thin PAH / PASA film of 40 bilayers. This process can be repeated any desired number of times and can be use to control the thickness of the ISAM film. The electrical tapes were then removed. Scanning Electron Microscopy (SEM) was used to investigate thickness of the ISAM film. The thickness of each bilayer is estimated to be 30 – 35 nm. The cross section of the film showed homogeneity as shown in Figure 2.

3. Results and Discussion

3.1 Cyclic Voltammetry

After constructing the PAH/PASA thin film, a three electrode CV technique was performed to characterize the electrochemical properties of PAH/PASA film in 0.1M NaClO₄ aqueous electrolyte solution. A Standard Calomel Electrode (SCE) was used as the reference electrode and a platinum flag (wire) as the counter electrode. The polymer film was scanned at 200mV/s from -600 mV to +1400mV to investigate the redox states. From the CV data operating voltage was determined to be in between -600mV and +600mV. The oxidation peak appears at approximately +600mV and reduction peak appears at approximately -600mV as shown in Figure 3.

3.2 Electrochromic Switching in Salt Solution

The electrochromic device was then immersed in 0.1 M NaClO₄ aqueous solution and the voltage was applied across the device and a copper electrode that was also immersed in the solution. The voltage was varied from -700mV to +700mV and

two color changes were observed at -600mV and $+600\text{mV}$, as it was predicted from the CV data as shown in Figure 4.

3.3 Results

To further illustrate the redox properties of the electrochromic material, we studied the optical properties of PAH/PASA device using the UV-Vis. spectroscopy method. In this method a concentrated beam of electromagnetic waves with varying wavelength from 400nm to 1100nm was shined at the device and the transmitted wave was collected at the other end of the apparatus for detail analysis of transmittance and absorbance behaviors of the device.

3.3.1 Absorbance

At -600mV the lowest absorbance in the visible range occurred at approximately 510nm , which corresponds to the dark green color of the film, and the highest absorbance occurred at approximately 690nm as shown in Figure 4 and 5.



Figure 4. Color change of 40 bilayers of PASA at different voltages. From left to right, at -600mV , 0.0mV , and $+600\text{mV}$.

At $+600\text{mV}$ the lowest absorbance in the visible range occurred at a wide range. The lowest value was at the highest wavelength, which corresponds to

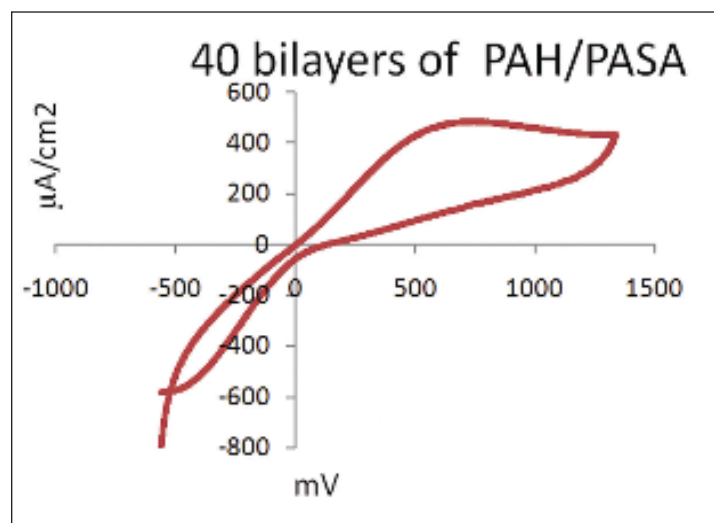


Figure 3. Cyclic Voltammetry of PAH/PASA at 200mV/s scan rate, oxidation peak can be seen at $\sim +600\text{mV}$ and reduction is predicted to be at $\sim -600\text{mV}$.

the gray color of the film as shown in Figure 4 and 5.

3.3.2 Transmittance

The highest transmittance difference was observed between the -600mV reduction peak and the neutral line. This showed an approximately 27% ($\Delta T=27\%$) contrast, which appeared at approximately 690nm wavelength as shown in Figure 6.

The highest contrast for the $+600\text{mV}$ oxidized state was approximately 25% ($\Delta T=25\%$) which was observed at approximately 480nm wavelength.

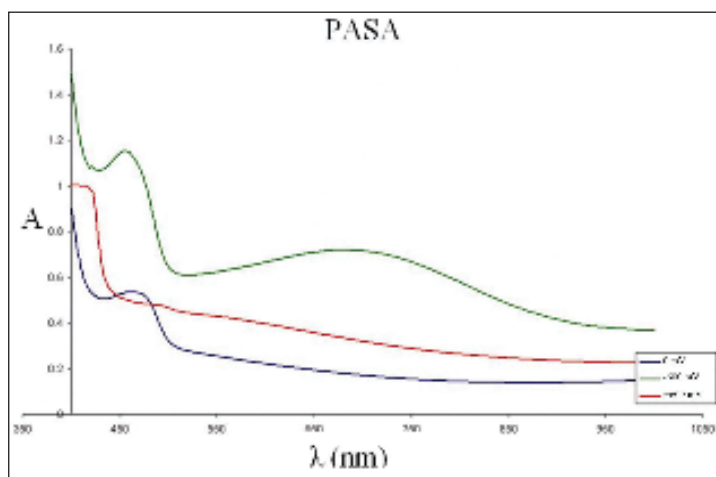


Figure 5. Absorbance measurements of PAH/PASA device at -600mV (reduction state) and $+600\text{mV}$ (oxidation state) in comparison with the absorbance of the device at neutral state (0mV).

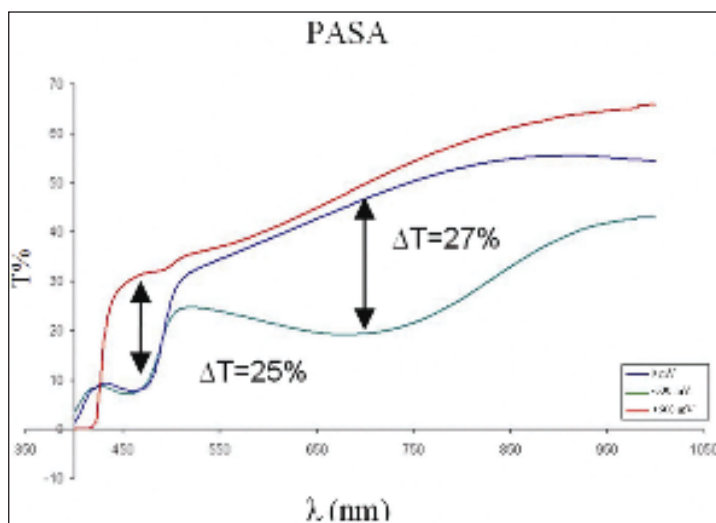


Figure 6. Transmittance measurements of PAH/PASA device at -600mV (reduction state) and $+600\text{mV}$ (oxidation state) in comparison with the transmittance of the device at neutral state (0mV). The highest contrast is about 27% that is observed at $\sim 690\text{nm}$, and is between reduced and neutral states.

4. Conclusions

Redox properties of a system based on PASA was demonstrated in this paper. PASA was found to have promising electrochemical and spectral properties. PASA has two redox states in the -1.0V to $+1.0\text{V}$ range. The color change remains after disconnecting the voltage, which confirms that the electrochromic device based on PAH and PASA polymers has long term memory. According to the CV data, the polymer film oxidizes at $+600\text{mV}$ and reduces at -600mV . The device changes color at both oxidation peak ($+600\text{mV}$) and reduction peak (-600mV) which agrees with the results from the CV. The device showed about 25% contrast at the oxidation peak and about 27% contrast at the reduction peak.

Acknowledgements

The author wishes to thank Dr. Randy Heflin and Mr. Vaibhav Jain for their guidance and assistance in the research described here during the 2005-2006 and 2006-2007 school years. The author also would like to thank NSF for providing financial support for this research and also departments of Physics, Chemistry, Chemical engineering, and MACRO program at Virginia Tech for making this research possible.

References

- [1] K. S. Kingo Itaya, Haruo Akahoshi, Shinobu Toshima, *Journal of Applied Physics* **1982**, 53, 2.
- [2] B. FGK, *Lampert CM, Granqvist CG (eds) SPIE institute series* **1990**, IS4 20.
- [3] R. D. Rauh, *Electrochimica Acta* **1999**, 44, 11.
- [4] K. B. P. V. Ashrit, G. Bader, F. E. Girouard and Vo-Van Truong, *Solid State Ionics* **1992**, 59, 10.
- [5] A. H.-L. G. a. W. Z. Marie-Claude Bernard, *Electrochimica Acta* **1998**, 44, 15.

About the Author



Reza Montazami received his B.S. in Physics and Astronomy from Virginia Tech in 2007. He is currently pursuing a Ph.D in Materials Science and Engineering at Virginia Tech.

Characterization of Electrolessly Plated Graphite Foams with Particle Additions

Michael Asaro, Jennifer Mueller, Patrick Dykema

Virginia Polytechnic Institute and State University, Department of Materials Science & Engineering
213 Holden Hall, Blacksburg, VA 24061

Abstract

With a low density and high bulk thermal conductivity, graphite foams are ideal for thermal management systems such as computer heat sinks, radiators, and heat exchangers. Previous work has shown it is possible to improve the foams performance by opening the porosity with nanoparticle additions in the foams precursor, an oil based mesophase pitch.^[1] The open porosity allows more fluid, such as air or water, to pass through the foam and carry heat away. The original study, performed by Jennifer Mueller at Oak Ridge National Labs (ORNL), considered the concentrations of nanoparticle's used. The present study looked to determine the effects of using different types of nanoparticles at a range of sizes from the nano- to micro- level. The study began by adding, respectively, silver, ceria, alumina, tungsten, and nickel to different batches of mesophase pitch at a single weight percent concentration to create graphite foams with a significant amount of continuous porosity. The pitch was foamed, carbonized, and graphitized. The final foam products were then measured in a variety of ways including thermal conductivity, permeability, and scanning electron microscope (SEM). As a side project, an electroless copper plating solution was passed through the foams to determine if a continuous and uniform copper coating could be built up. The copper coating that was eventually obtained coated the foam walls without filling the open porosity and may help to increase the foams solderability, strength, durability, and corrosion resistance.

Keywords: Carbon, Foam, Thermal, Electroless

1. Introduction

Graphite foams are an excellent material for use in thermal management systems such as computer heat sinks, radiators, and heat exchangers. The graphite ligaments themselves have a thermal conductivity of $>1700 \text{ W/mK}$.^[2] As can be seen in Figure 1, they are usually aligned parallel to the pore structure, which gives the bulk foam a thermal conductivity on par with aluminum. The foams also exhibit a very low density of approximately 0.5g/cm^3 , one-fifth that of aluminum.^[2]

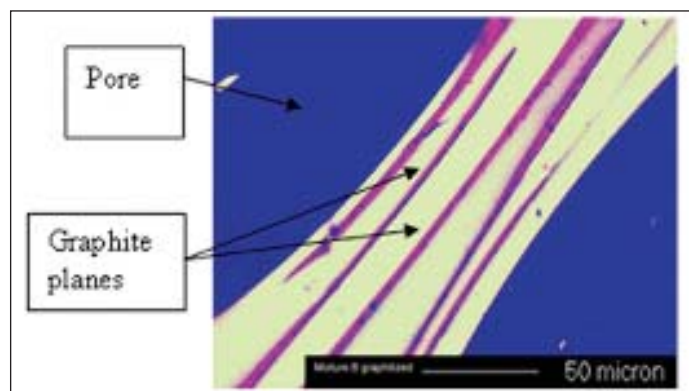


Figure 1. Optical image of graphite foam showing highly aligned graphite planes

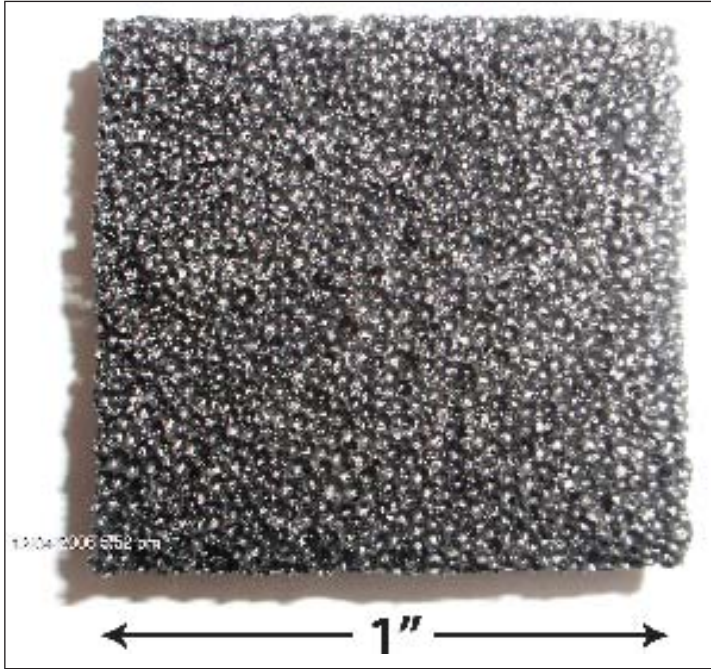


Figure 2. Photograph of graphite foam

Previous work has shown that the addition of carbon nanoparticles to the foam precursor, an oil based mesophase pitch, will act as nucleation sites for pore windows during the foaming process. The open porosity will create a more permeable foam with a greater capacity to let fluid move through it; this will create a better performing system with greater overall efficiency. Whereas the previous work looked at the effects of varying the concentrations of the nanoparticles, the new work looked to determine how particles of different materials and varying sizes at the same concentration, 5 weight percent, would effect the pore structure.

A side project looked to explore the feasibility of passing an electroless copper plating solution through the foam with the increased open porosity. A copper layer could help to improve the foams solderability, strength, durability, and corrosion resistance. The electroless plating side project culminated in a continuous and uniform copper coating throughout the surface of the foam without filling the open porosity.

2. Procedure

2.1 Foam Preparation

Ceria, nickel, tungsten, silver, and alumina particles were each added to the mesophase pitch precursor, at 5 weight % concentrations, and processed to create graphite foam. Their measured particle size can be seen in Table 1 where the particles ranged from 11um to 50nm

Particle Size Data		
	Mean Size (um)	Median Size (um)
Alumina (0.05)	Not Accurate	
Alumina (0.30)	1.95	0.27
Ceria	5.39	4.99
Nickel	12.69	9.69
Silver	0.62	0.47
Tungsten	11.84	10.72

Figure 3. Particle size data

(the analyzer used was unable to get an accurate reading on the 50nm alumina because the particles were too small). The pitch-particle mixture was heated in an oxygen-free atmosphere to approximately 50°C above the pitch’s softening point. The pressure and temperature in the furnace were then raised after the pitch had melted. In its molten stage, the pitch formed bubbles at nucleation sites, and mesophase crystals formed. The mesophase pitch began to polymerize and the bubbles were trapped in place creating a foam structure. After the foaming process the material was carbonized by slowly ramping a furnace up to 1000°C. Finally, the carbonized foam was graphitized at 2800°C in an inert atmosphere of nitrogen and argon.

2.2 Permeability

Tests were conducted at Oak Ridge National Laboratory on an apparatus developed to measure the face velocity of air flowing into and out of the system, thus giving a pressure drop. A (2 x 2 x 0.25 inch) block of graphite foam was placed into the system and the lid tightly sealed. The flow rate was manually adjusted to obtain face velocities varying from 0 to 300 Ipm and the corresponding pressures were recorded.

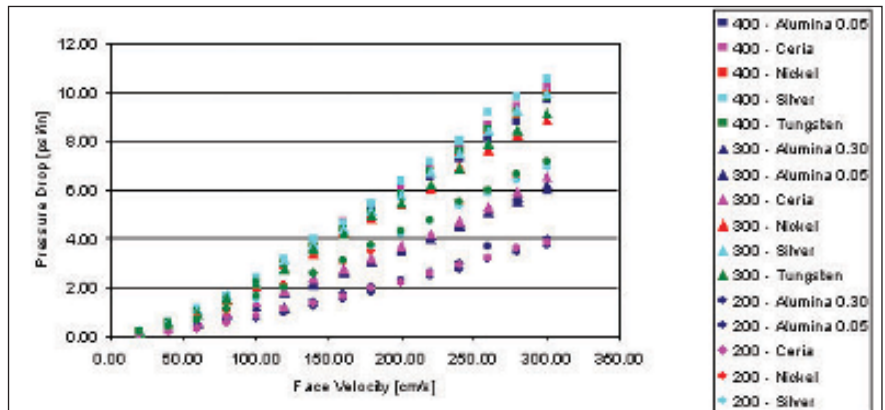


Figure 4. The effects of the type of particle and processing pressure on the foams permeability

2.3 Scanning Electron Microscopy (SEM)

Samples were viewed with a LEO 1550 Field Emission SEM with an accelerating voltage of 5 kV to view the graphitized samples. Since the carbon foam is already electrically conductive, the samples did not need to be sputtered with a metallic coating before being analyzed.

2.4 Electroless Plating

Electroless plating consists of three major steps: sensitizing, activating, and plating. Sensitizing helps to gather all the readily oxidized material on the surface. The activating step lays down a layer that provides catalytic nucleation sites. The final plating stage builds a uniform autocatalytic layer on the surface that will continue to thicken as long as new solution is passed over the surface.

2.5 Thermal Conductivity

Thermal diffusivity was measured using a xenon flash diffusivity technique and thermal conductivities were calculated using Equation 1.^[5] The technique involves a bulb flashing for less than 1 millisecond and releasing a small amount of heat on one side of the sample. An IR camera at the other side measures the change in temperature.

$$\alpha = \frac{\kappa}{\rho C_p} \quad (1)$$

Where:

α is the thermal diffusivity

κ is the thermal conductivity

ρC_p is the heat absorbed by the material

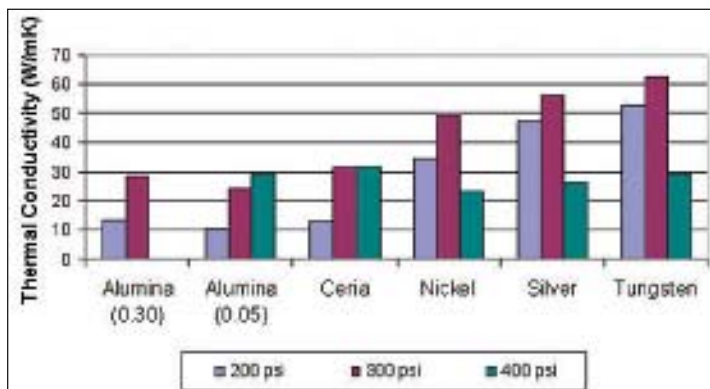


Figure 5. The effect of the type of particle on the thermal conductivity

3. Results and Discussion

3.1 Particle Additions

The foams that were processed at higher processing pressures had a higher pressure drop, meaning there was less open porosity, compared to the foams processed at lower pressures for a given material (Figure 4). Interestingly though, the ceramic particles caused more open porosity than the metal particles at the two lower processing pressures, but were about equal at the 400psi processing pressure.

At the 400 psi pressure level, very little change can be seen in the thermal conductivity of the foams. The 200 and 300 psi runs, however, show significant differences between the metal and ceramic particles. See Figure 5.

The larger of the alumina and silver particles had respective median sizes of 0.3um and 0.5um. The nickel and tungsten particles had a median size of approximately 10um. As can be seen in Figure 5 below, the trend in these numbers is not consistent with the trend in thermal conductivity. This means that cheaper particles of larger sizes can be used to increase the thermal conductivity just as effectively as the smaller particles.

3.2 Copper Plating

As can be seen in Figure 6 a copper coating was obtained. The EDS analysis in Figure 7 shows that the pores are indeed copper while the ligaments remain pure carbon. Figure 8 shows a picture of the copper plated foam taken with the SEM. The non-coated pores could have occurred either because no plating reached the pore or the copper fell out during the cutting process.

4. Conclusions

Adding particles to the foam precursor helped to increase the amount of open porosity and thus allow

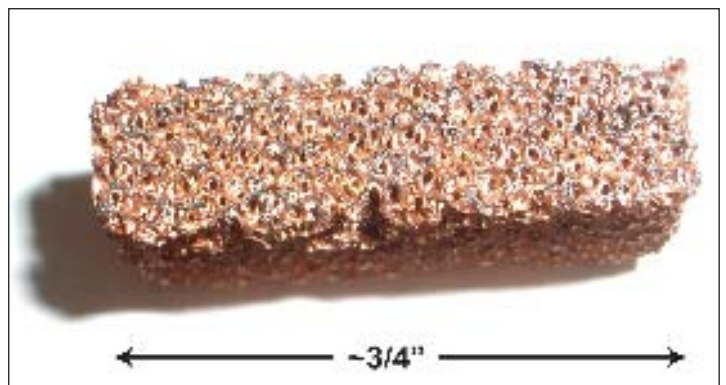


Figure 6. The inside of a piece of foam that was coated with copper

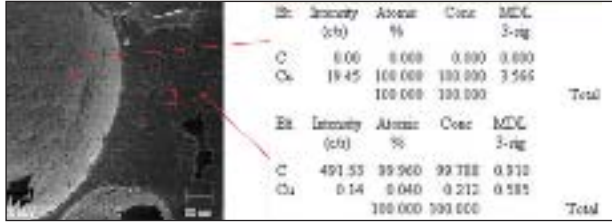


Figure 7. EDS analysis showing the pore as 100% copper and the ligament as 99.96% carbon

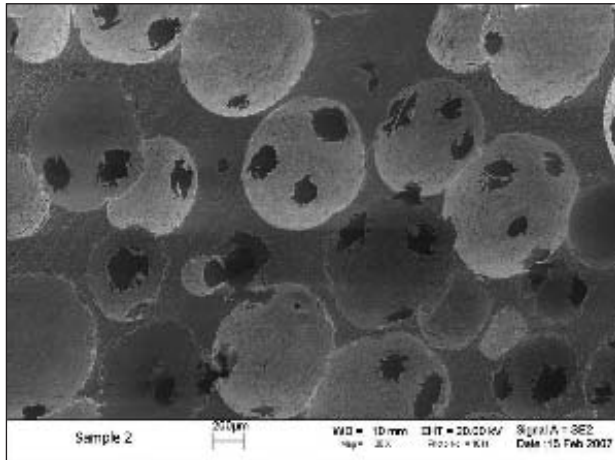


Figure 8. An SEM image showing numerous pores coated with copper

more heat to be dissipated into the atmosphere more quickly. The specific properties of the particles that affect the amount of porosity have yet to be determined, but there is a very clear trend that at lower processing pressures (less than 400 psi), ceramic particles have a much greater effect than metal ones. Thermal conductivity of the foams was also aided by the addition of particles at the lower processing pressures, but the specific properties that are most important are still unknown.

The feasibility of coating the foam with a uniform layer of copper was shown. Other plating materials should be possible but at this point are untested.

Acknowledgements

We would like to thank graduate student, Ben Poquette for his help with numerous aspects of the project and most importantly his support in the lab during the copper plating experiments. The work was done under the supervision of Dr. Steve Kampe with the aid and ideas of Dr. Gary Pickrell and Dr. Marie Paretti. Their input was invaluable.

References

- [1] Gallego, Nidia C. and Klett, James W. 2003. Carbon Foams for Thermal Management. *Carbon* 41: 1461-1466.
- [2] Klett, James W. High Thermal Conductivity Foams One Pager. Available at: <http://www.ms.ornl.gov/researchgroups/CMT/cmt.htm>, Accessed on October 12, 2006.
- [3] Klett, James and McMillan, April. Modeling Convective Heat Transfer with Graphite Foams. Available at: <http://www.ms.ornl.gov/researchgroups/cmt/foam/Convective%20Heat%20Transfer.pdf>. Accessed on April 2, 2007.
- [4] Klett, James W. High Conductivity Graphite Foams and Applications." Available at: <http://www.ms.ornl.gov/researchgroups/CIMTECH/foam/one-pagers.pdf>, Accessed on April 2, 2007
- [5] Klett, J. W., McMillan, A. D., Gallego, N. C., Walls, C. A. 2004. The Role of Structure on the Thermal Properties of Graphitic Foams *Journal of Materials Science* 39: 3659-3676.

About the Author



Michael Asaro is a senior at Virginia Polytechnic Institute and State University in Blacksburg, VA. After graduation this spring he will begin graduate work in Materials Science and Engineering at Virginia Tech as well as a career at Nanosonic, Inc., a company also located in Blacksburg.

The Effect of Cornstarch Levels on the Surface Quality of Extruded Soy Protein Plastic

Evan M. Ziolkowski

University of Wisconsin–Madison, Department of Materials Science & Engineering
1509 University Avenue, Madison, WI 53706

Abstract

The ratio of soy protein isolate to cornstarch was studied in the extrusion of four different formulations of soy protein plastic in order to qualitatively examine the surface quality upon extrusion. Levels of glycerol and moisture were constant across all samples, and no other additives were used in the mixtures. Mixtures were made using a planetary mixer, and then extruded using a single-screw extruder equipped with a 10.16 centimeter sheeting die with a 0.152-centimeter opening. The surface of the extruded plastic became smoother with increasing starch content, but the processability became too difficult with very high starch levels.

Keywords: soy protein plastic, biopolymers, sheet extrusion

1. Introduction

With increasing awareness of the environmental hazards surrounding petroleum-based plastics, many have started researching alternative materials to avoid these risks. One of the primary environmental issues for any material is its relative biodegradability. While petrochemicals have dominated the plastics industry for the last 70 years, there are concerns about the extended use of conventional plastics and the effect they may have on the environment.^[1] A widespread system for plastics recycling is available in most areas of the United States, but the system largely relies on the consumer to take responsibility for his or her own refuse. For these reasons, demand for biodegradable plastics, such as those made using a soy protein base, has risen in recent years.

1.1 Forms of soy protein

The three basic forms of soy protein are soy flour, soy protein concentrate, and soy protein isolate. Soy flour is produced by grinding soybeans into a powder, discarding the hulls, and extracting the oil. Soy protein concentrate, a more purified form that contains approximately 65% protein, is made by leaching out all of the water soluble carbohydrates from soy flour.^[2] Soy protein isolate, the purest and most expensive form, can be produced by a chemical treatment process to bring the soy to

an approximate 90% protein content.^[2] Much of the research done today on soy protein plastics is done using soy protein isolate to better manage the levels of each component in the mixture prior to processing.

1.2 Early research in soy protein plastics

The concept of using soy protein in both plastics and adhesives has existed as early as the 1910s. Patents were first issued in 1913 and 1917 for preparing plastics from a soy protein base.^[1] In the early 1930s, Ford Motor Company researched methods to develop and produce a soy-based resin that would be used in their vehicles for interior plastic components. This and prior research was ultimately abandoned because of the industry's overall move towards plastics based on petrochemicals for their wide availability, easy processability, and lower price.^[1]

Today, the market is beginning to return its focus toward the possibilities of more widespread use of soy protein plastics.^[1] The prospect of global climate change and the volatility of oil supply and price is driving a demand for plastics made from materials other than petrochemicals. Environmentalists have been pushing for research in the area of biopolymers as a way to reduce the amount of plastic consumed in the world.^[2] In order to reduce petroleum-based plastic use on the consumer level, further advancements must be made to allow for using biopolymers in consumer plastics.

1.3 Recent research in soy protein plastics

The primary areas of research on soy protein-based plastics are to reduce the cost of soy protein plastic products, and to improve both their short- and long-term mechanical performance.^[3] Recent research has already shown that various polyols (such as sorbitol and glycerol) and water will plasticize soy protein effectively, but each of the plasticizing agents created somewhat different properties in the resulting plastics.^[4] Some alcohols studied for use as plasticizers are toxic to humans, so the type of plasticizer used depends on the application of the final product.^[3] Like different kinds of plastics, different formulations and the soy-to-plasticizer ratio will also affect the applications in which the plastic can be used.

One of the main problems currently hindering the use of soy-based plastic in consumer product applications is the relative processability of these new biopolymers in comparison to the current consumer-grade plastics on the market. The research world knows little about the behavior of soy protein plastics when they are formed or molded using the common methods of processing petrochemical polymers. Recently, however, several research groups have done studies on the molecular composition^[5] or mechanical properties of extruded or compression-molded plastic.^[6,7]

At the University of Wisconsin–Madison, recent studies have focused on the rheology of soy protein isolate-based plastics,^[8] and this project is continuing to expand on that research through the examination of different formulations of soy-based plastics and the surface quality after extrusion. This sheet extrusion research focuses on altering the levels of cornstarch and soy protein in the different formulations, while maintaining the levels of water and glycerol in each composition.

2. Procedure

Four different formulations of soy protein-based plastics were explored by altering the ratios of soy protein isolate and starch. Soy protein isolate was used instead of soy protein concentrate in order to more carefully manage the ratio of protein and starch in the formulations. These formulations were then extruded using a single-screw extruder with a 10.16 centimeter wide sheeting die to extrude an approximate 0.152-centimeter thick profile. The extrudate quality was examined qualitatively, with careful attention to the surface properties and the consistency of the plastic.

2.1 Formulations

Each formulation was composed of soy protein isolate, cornstarch, lab grade glycerol, and deionized water. The formulations, shown in Table 1, are variations of those used by Ralston.^[8]

The moisture content of each component of the formulations was tested using a moisture analyzer. The moisture content was factored into the calculation to find the dry weight of the components needed in each formulation.

Formulations by % weight				
	A	B	C	D
Soy Protein Isolate	31.2	26	20.8	13
Starch	20.8	26	31.2	39
Glycerol	18	18	18	18
DI Water + Moisture	30	30	30	30

Table 1. Composition of the formulations by weight percent

2.2 Preparation

To prepare each formulation, the soy protein isolate and cornstarch were measured and blended using a planetary mixer for five minutes before adding the glycerol and deionized water. Each mixture was then blended in the planetary mixer for ten more minutes. The sides of the mixing bowl were scraped, and any large pieces of material were broken apart. Each formulation was then mixed for an additional fifteen minutes.

Each formulation was blended until the consistency was that of a damp powder. Approximately 500g of each formulation was produced, and was extruded immediately following the mixing process to reduce moisture loss.

2.3 Extrusion

Each formulation was extruded using a single-screw Brabender plasticorder extruder, with a 10.16 centimeter wide sheeting die set at 0.152 centimeters in thickness, at variable speed between 15 and 50 RPM. The temperature zones were set at 90°C, 125°C, 135°C, and 105°C from the first zone, immediately following the feed throat, to the die. These temperatures were chosen since it has been shown that an optimal injection molding temperature for soy protein plastics is 130°C.^[9] Though the plastic was not being injection molded, the soy was still being processed though an outlet with a small thickness.

3. Results and Discussion

For the purposes of this experiment, all observations were qualitative in nature. Large differences were exhibited in the processability and surface quality between each of the four

formulations, so higher precision was unnecessary for the scope of the project.

3.1 Observations during extrusion

Formulations A and B, the formulations with lower cornstarch content, exhibited some tearing at the die during extrusion. Formulation A showed high tearing on the edges and some roughness on the top and bottom faces of the extrudate, where formulation B exhibited very little tearing on the edges and smoother top and bottom faces.

Formulation C extruded with a fairly smooth overall surface, and exhibited virtually no tearing at the edges of the plastic. This mixture seemed to extrude the most easily of all tested formulations.

Finally, formulation D extruded with some difficulty and was unable to completely fill the die with material. The powder would frequently squeeze back out toward the feed throat, even when the screw was not filled with material. Nevertheless, the surface quality of this formulation was smooth and comparable to formulation C.

3.2 Observations after extrusion

All four formulations behaved similarly while cooling. The extrudate was still flat and flexible, even when it was cool to the touch. After it sat in open air overnight, the plastic was much harder and curled slightly from the center to the edges across the width of the extrudate. All of the formulations could be either cut with scissors or scored with a blade after this overnight drying period.

Formulations A through C all retained a similar surface quality, but formulation D had a drier appearance after drying overnight.

3.3 Analysis of observations

Formulation A exhibited tearing at both the edges and the top and bottom surfaces of the extrudate, and formulation B showed only some mild tearing on the surfaces. It is assumed that since the only difference between the two mixtures is the increased level of starch in formulation B, that the higher starch content was the reason for the improved surface quality. The extrusion of formulation C further supported this statement, because little to no tearing was observed on either surface or the edges of the extruded material.

The difficulty with formulation D indicates that an upper limit does exist in processing this basic formulation of soy protein plastic effectively. The results for formulation D were also poor when compared to formulation C. The addition of other additives, such as soy oil, may be useful to the processing of the plastic and further refine the extrudability of these basic formulations.

3.4 Mold growth

Prior to extrusion, formulations that were mixed and then stored in plastic bags began to grow mold after one and a half weeks of storage. The cause of this mold growth is unknown, as previous formulations of soy protein plastic did not exhibit this problem. After extruding, mold growth does not appear to be an issue.

4. Conclusions

4.1 Feasibility

Increasing levels of cornstarch in the soy protein plastic formulations clearly have an effect on the surface quality of the final extruded plastic film. While the exact cause for these differences remains unknown, it is possible that the inclusion of cornstarch reduces the coefficient of friction between the plastic and the metal screw and die. This idea could also explain why formulation D had such difficulty in processing; very low friction could cause the plastic to slip on the screw too easily, which will reduce the overall processability.

Formulation C exhibited the most feasible combination of processability and final surface condition out of the four mixtures tested. Since the ratio of starch to soy protein isolate was 3:2, it is possible that soy protein concentrate and cornstarch could be used in the mixtures to produce similar results. The lower cost of soy protein concentrate could allow more inexpensive but comparable materials to be produced.

4.2 Future research

This research could be continued by looking for a more optimal starch level, and also by comparing the results of this research to qualitative properties of the extrudate after including other additives in the mixture, such as soy oil. Also, testing the tensile properties, water resistance, variance of the coefficient of friction, and biodegradability of the extruded material can continue the optimization process. These properties can be compared to those of conventional petrochemical plastics. Finally, comparative mixtures could be tested using soy protein concentrate in place of soy protein isolate to see the variability in properties between the two grades of soy protein.

Acknowledgements

This work was done at the University of Wisconsin–Madison as a senior design project under the supervision of Dr. Tim A. Osswald and Brian Ralston, from the Department of Mechanical Engineering, and Dr. James A. Clum from the Department of Materials Science and Engineering.

References

- [1] Myers, D.J. Industrial applications for soy protein and potential for increased utilization. *Cereal Foods World* **1993**, *38*, 355-360.
- [2] Swain, S. N., Biswal, S. M., Nanda, P. K., Nayak, P. L. Biodegradable soy-based plastics: opportunities and challenges. *J. Polym. Environ.* **2004**, *12*, 35-42.
- [3] Kumar, R., Choudhary, V., Mishra, S., Varma, I.K., Mattiason, B. Adhesives and plastics based on soy protein products. *Ind. Crops Prod.* **2002**, *16*, 155-172.
- [4] Wang, S., Zhang, S., Jane, J.L., Sue, H.J. Effect of polyols on mechanical properties of soy protein. *Polym. Mater. Sci. Eng.* **1995**, *72*, 88-89.
- [5] Choi, S. G., Kim, K. M., Hanna, M. A., Weller, C. L., Kerr, W. L. Molecular dynamics of soy-protein isolate films plasticized by water and glycerol. *J. Food Sci.* **2003**, *68*, 2516.
- [6] Wan, V. C., Kim, M. S., Lee, S. Water vapor permeability and mechanical properties of soy protein isolate edible films composed of different plasticizer combinations. *J. Food Sci.* **2005**, *70*, E387.
- [7] Seung, Y. C., Chul, R. Sorption characteristics of soy protein films and their relation to mechanical properties. *Lebensmittel-Wissenschaft Technol.* **2001**, *35*, 151-157.
- [8] Ralston, B. E. & Osswald, T.A. Viscosity of soy protein plastics as determined by screw-extrusion through a capillary die. *Soc. Plast. Eng. Annu. Tech. Conf. Proc.* **2006**, 1479-1483.
- [9] Huang, H. C., Chang, T. C., Jane, J. Mechanical and physical properties of protein-starch based plastics produced by extrusion and injection molding. *J. Am. Oil Chem. Soc.* **1999**, *76*, 1101-1108.

About the Author



Evan M. Ziolkowski graduated with his B.S. in Materials Science and Engineering and a Technical Communication Certificate in May of 2007 from the University of Wisconsin-Madison. He is originally from Arlington Heights, IL.

Statistical Analysis of Impedance Data for Jet Turbine Oil Additives

Matthew T. Luke

Boise State University, Department of Material Science and Engineering
1910 University Dr. Boise, ID 83725

Abstract

A gold, parallel-plate capacitor test cell was used to make electrochemical impedance spectroscopy (EIS) measurements on high resistivity gas turbine engine oil as a function of the oil additive type. The additive effects on the EIS response were determined by analyzing ester-based basestock oil mixed with a single additive. This work was performed for four different additives: antioxidant, metal deactivator, anti-wear, and extreme pressure. Multiple measurements were made for each basestock-single additive mixture. To determine whether the EIS response of each additive showed a significant difference, statistical analysis was performed on the data using a student's t-test. Low-frequency data showed the largest difference in additive responses. Statistical analysis showed that the extreme pressure additive has the greatest effect on oil impedance. Mixtures of antioxidant and metal deactivator additives did not show interaction.

Keywords: electrochemical impedance spectroscopy, sensor, turbine engine, oil, additive

1. Introduction

Recently, there has been a great interest in using electrochemical techniques as non-destructive methods for monitoring oil quality.^[1-3] Oil quality can be a function of contamination, oil degradation, and additive depletion. This paper focuses on using electrochemical impedance spectroscopy (EIS) to study individual additive effects.

Based on earlier work that analyzed oil conditions using EIS, a gold, parallel-plate sensor was used to make measurements for various oil additives, figure 1.^[4] The inert electrode materials allow for the direct measurement of an oil binary mixture (oil + single additive) by negating interfacial reactions that would occur using a bearing steel substrate. Several additives are used in oils and lubricants to protect the engine from heat and wear. Monitoring additive levels can provide insight into their role in preventing engine wear as well as signal timely oil replenishment. Making distinctions in impedance data requires analyzing statistical variations.

Oil additives in the synthetic ester basestock include: metal deactivator, extreme pressure, antioxidant and anti-wear. The

extreme pressure additive forms a tribological film on the substrate under high pressures to reduce wear. The metal deactivator additive protects soft metals in the lubricant system such as Cu and Mg and chelates wear particles formed from these metals. A chelating agent is a molecule that bonds to specific ions in a solution and, in this case, prevents them from reacting/interfering with the lubricating properties of the oil. The anti-wear molecule creates a tribological film on the ferrous bearing and gear surface to reduce wear. The antioxidant molecule reacts with free oxygen in hot engine environments to prevent degradation of the oil basestock molecules. A more detailed summary of the additives is found shown in table 1. It should be noted that each additive concentration in the binary mixtures (oil + additive mixtures) closely corresponds to additive concentrations present in the full formulation for each respective additive.

EIS analysis was performed on the basestock oil plus single additive mixtures to understand the additive effects. In addition to the single additive mixtures, two additives were mixed to determine the effects of additive interaction. Since the metal

deactivator additive tends to be acidic while the antioxidant additive tends to be basic, these two additives were mixed and tested for interaction.

To ensure that the variations in the EIS data were significant, statistical analysis was used to compare data sets. Accounting

Oil Component	Code	Purpose	Compound and General Structure
Basestock	same	A 5 cSt oil. The 5 cSt oil gives the best thermal stability maintaining a deposit free engine (40K hrs between maintenance).	Fully Synthetic esters (Pentacyclic + organic acid (C5 to C10 acids))
Antioxidant	AO	Phenyl- α -naphthylamine is used to react with free oxygen in hot environments so that the oxygen does not oxidize the basestock and cause deposits or make the oil acidic.	Aromatic Amine (phenyl- α -naphthylamine) N-(1-Naphthyl)sealine
Metal Deactivator	MD	Benzotriazole is used to chelate any wear products that can get into oil and deliver these particles to the filter.	Benzotriazole
Anti-Wear	AW	Tricresyl Phosphate associates with ferrous surfaces making a low shear stable film that acts as a sacrificial tribological or boundary layer to prevent wear.	Mix of para/meta isomers of Tricresyl Phosphate
Extreme Pressure	EP	Performs the same function as an anti-wear additive but at high pressures.	Generally compounds containing chlorine or sulfur.

Table 1. Summary of oil additives found in a commercial grade engine oil

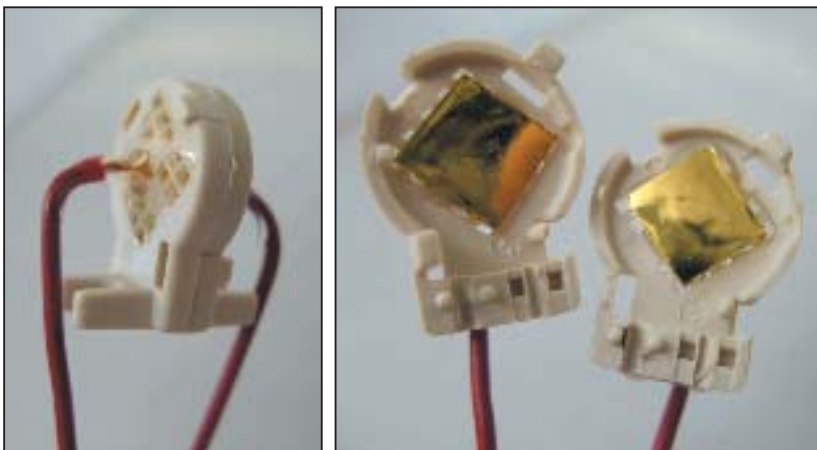


Figure 1. Capacitive Impedance Sensor constructed for use in additive testing. The plastic case keeps the electrode faces at a constant spacing.

for the statistical variation in data sets is necessary for making predictions based on the impedance measurements (i.e. if the results are within the range of statistical error, no prediction can be made).

2. Procedure

All EIS measurements were made using a Gamry Reference 600 Potentiostat/Galvanostat/ZRA inside of a copper Faraday cage. A two-electrode EIS set-up was used to make the measurements (to prevent impedance artifacts due to charging of a reference electrode). Both electrodes were made of high purity gold foil and all tests were performed at measured room temperature ($23 \pm 2^\circ \text{C}$).

Construction of a sensor from an existing casing allowed for a constant electrode spacing. The plastic superstructure of an HS1101LF-ND humidity sensor (obtained from Digi-key Inc.) was used for the sensor casing, figure 1.

Pure gold foil, attached to copper wire leads, was attached with epoxy to the inside of the case. Only the electrode faces were exposed to the oils. This sensor was immersed in each of the additive/oil mixtures and the open circuit potential was monitored for 10 minutes to ensure stability. All tests were performed in open air and as such, absorption of a small amount of ambient moisture by the oil was assumed. Absorption was considered to be consistent between tests and to have a minor effect on impedance. The first test used fresh oil and a clean sensor. For the second test, the oil was stirred but the sensor was not cleaned. For the third and fourth tests fresh oil was again used and the sensor was cleaned between tests. The AC amplitude was 1V. This amplitude was selected to reduce the noise in the data. (AC amplitudes as low as 100 mV were studied and the trends in the impedance response remained the same, however, the noise increased.) The measured frequency range for the test was 1,000,000 Hz to 0.001 Hz.

It should be noted that the gold electrode surfaces were slightly non-planar and this could lead to the appearance of a second double-layer capacitance, which appears as a second “hump” in a Nyquist plot of the data. Charge that builds up at the surface gives rise to a double-layer capacitance term. However, if the surfaces are not flat, this double-layer can vary over the surface of the electrode and can give rise to a second, or pseudo-double-layer capacitance.

For the tests involving the metal-deactivator and antioxidant mixtures the same setup and procedure was followed, except the frequency range was shortened. The frequency range tested was 1,000,000Hz to 0.01Hz. Three different ratios of antioxidant to metal deactivator were tested: 1:1, 1:2 and 2:1.

EIS data is typically displayed on Bode and Nyquist plots. When dealing with AC, Ohm's Law becomes $V = IZ$ where Z is impedance with real and imaginary components. A Bode plot shows the magnitude of the impedance ($|Z|$), also called the modulus or Z_{mod} versus frequency on a logarithmic scale.

Nyquist plots show the imaginary versus real components of impedance.

3. Results and Discussion

The data for the additive tests are shown in Figures 2 and 3.

Compiling the data from the four trials, an average impedance value, with its standard deviation, was calculated at two different frequencies (at a high and low frequency). The stated variance

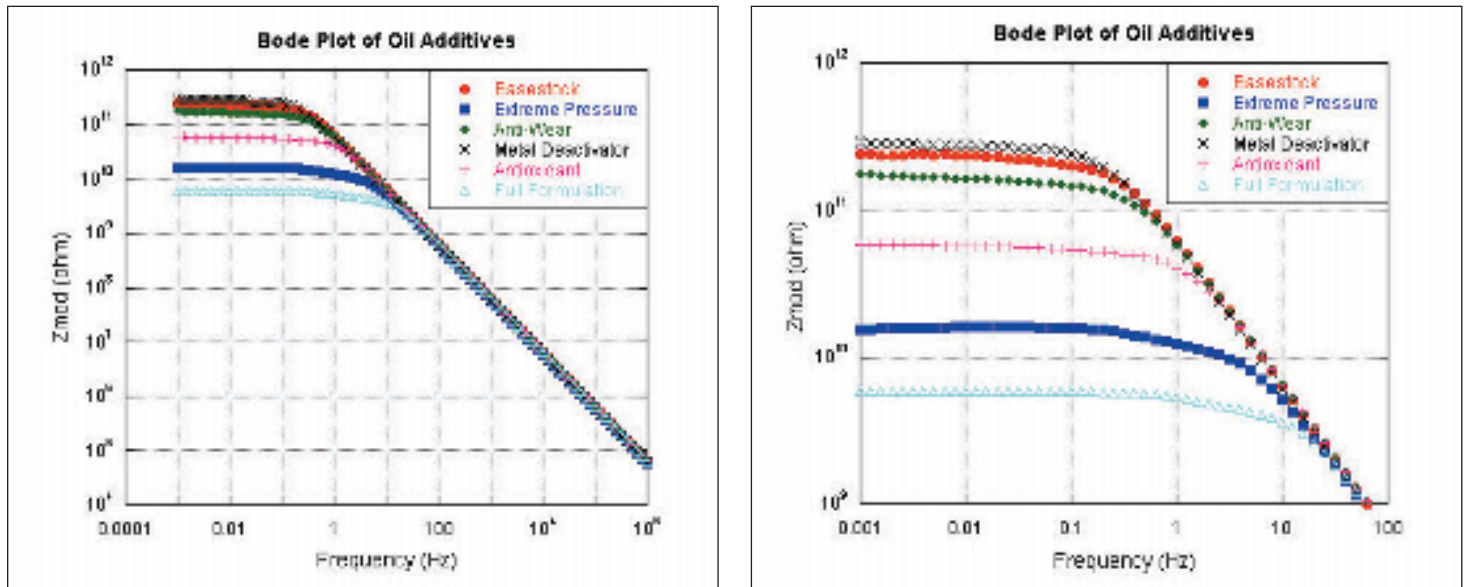


Figure 2. Bode magnitude plot of each BP oil tested. The left shows the full frequency range tested. The high frequency data shows no difference between the oils. The graph on the right is an enlarged view of the low frequency range. The curve selected for each oil was the one closest to the mean.

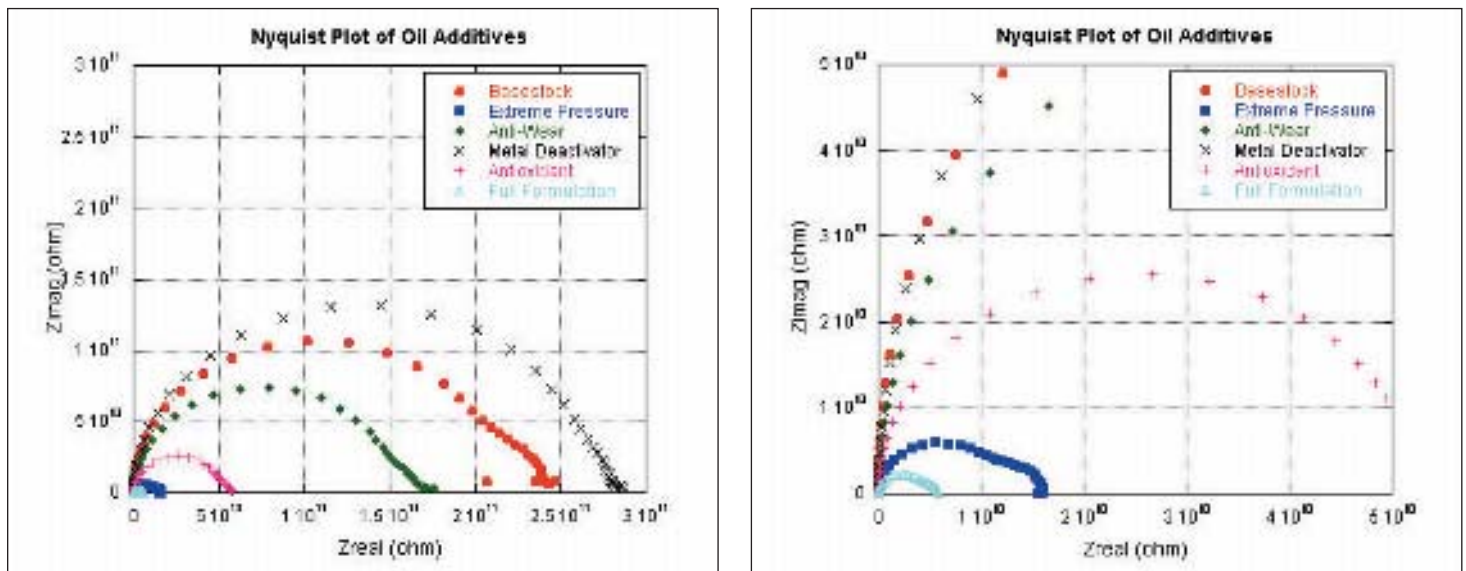


Figure 3. Nyquist plots of the oil additives. The figure to the right shows a zoomed in view of the lower impedance oils (extreme basestock and full-formulation).

in the tables represents one standard deviation. For the high frequency range value, 100 kHz was selected because it lies in the linear range of the Bode plots. For a low-frequency point on the Bode plots 10 mHz was chosen. At this point the slope has changed and the impedance value appears stable.

Statistical analysis was performed for each sample using a paired t-test.^[5] Each sample was first compared to the basestock oil then to the full formulation. The t-test values on the table indicate a statistical significance at a 95% confidence level. The probability of the null hypothesis (that there is no difference in the samples, H_0) is also included to show the how far from the confidence level each sample is. The data is summarized in table 2. Variance from the mean is one standard deviation. T-test values indicate statistical significance at 95% confidence; = indicates no statistical significance, +/- indicate significantly higher or lower values. H_0 values indicate the t-probability associated with the paired t-test values showing confidence levels for all tests. The top group shows a comparison of each oil to the basestock oil while the

10mHz					
Oil/Additive	Zmod (GΩ)	N	t-test	H_0	% change
Basestock	189.85 ± 81.1	4			
EP	14.80 ± 2.0	4	-	0.032	-92.3
AW	177.10 ± 10.3	4	=	0.792	-8.8
MD	284.35 ± 80.8	4	=	0.279	39.2
AO	59.59 ± 4.2	4	-	0.060	-68.6
Full	8.18 ± 0.2	4	-	0.027	-98.6
Full	5.15 ± 0.2	4			
EP	14.80 ± 2.0	4	+	0.004	137.0
AW	177.10 ± 10.3	4	+	< 0.001	2775.0
MD	284.35 ± 80.8	4	+	0.003	4191.4
AO	59.59 ± 4.2	4	+	< 0.001	867.4
100kHz					
Oil/Additive	Zmod (kΩ)	N	t-test	H_0	% change
Basestock	627.55 ± 30.0	4			
EP	591.86 ± 34.4	4	=	0.342	-5.7
AW	653.75 ± 22.1	4	=	0.338	4.2
MD	624.45 ± 28.1	4	=	0.844	-0.5
AO	628.08 ± 56.9	4	=	0.978	0.1
Full	658.13 ± 15.0	4	=	0.083	4.9
Full	658.13 ± 0.2	4			
EP	591.86 ± 2.0	4	=	0.060	-10.1
AW	653.75 ± 10.3	4	=	0.827	-0.7
MD	624.45 ± 80.9	4	=	0.057	-5.1
AO	628.08 ± 4.2	4	=	0.249	-4.6

Table 2. Summary of impedance data at two frequencies, 10mHz and 100kHz.

second group shows a comparison to the full formulation. The 10 mHz impedance data is summarized on the following graph, figure 4, where the mean value for each oil is plotted with error bars representing one standard deviation.

The first set of data in Table 2 compares the additive oil mixtures to the basestock. The basestock displays the most variance in data. Although the values are not statistically significant, the addition of an additive reduces the variance. It was found that only the extreme pressure additive and the full formulation are significantly different from the basestock (using a 95% confidence level) but that the antioxidant additive had a H_0 probability of 0.06 indicating it is close to the confidence level. It is possible that with larger sample sizes this additive also could be shown to be significantly different from the basestock.

The second set of data in Table 2 compares the additives to the full formulation. All additives are significantly higher when compared to the full formulation (as noted by the + sign in Table 2). The extreme pressure additive appears to have the

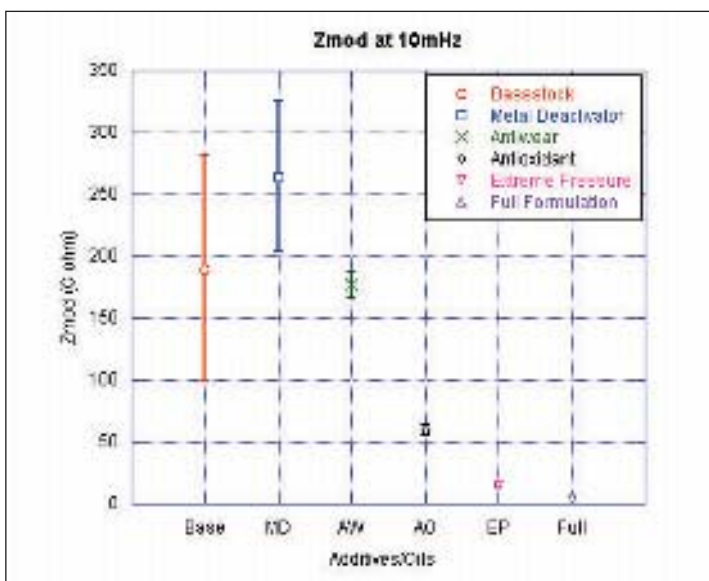


Figure 4. The mean value of each oil plotted with error bars representing one standard deviation. Only the extreme pressure additive and full formulation are statistically significant from the basestock (using a 95% confidence level).

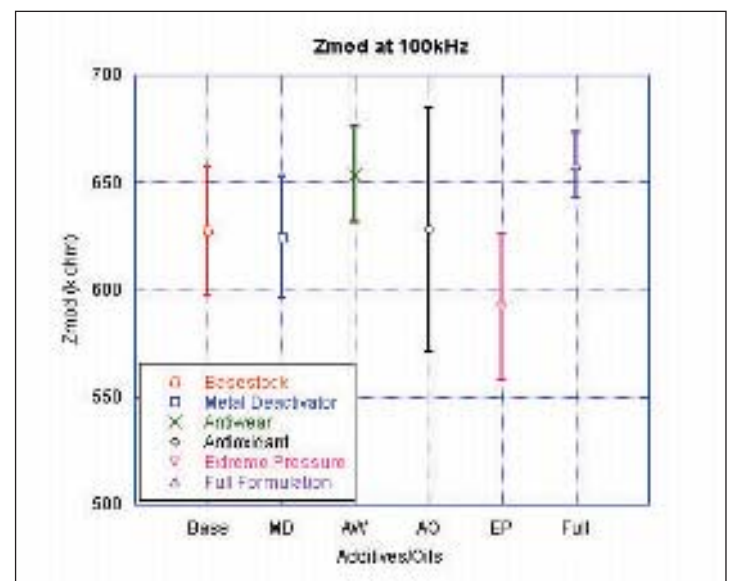


Figure 5. Mean value and standard deviation error bars of oil additives at 100 kHz. None of the tests were significantly different from one another.

Mixtures					
10mHz					
Oil/Additive	Zmod (kΩ)	N	t-test	H ₀	% change
MD	264.35 ± 60.9	4			
1AO-2MD	132.3 ± 8.7	4	-	0.015	-50.0
1AO-1MD	140.7 ± 24.4	4	-	0.027	-46.8
2AO-1MD	91.63 ± 5.5	4	-	0.009	-65.3
AO	59.59 ± 4.2	4	-	0.006	-77.5
AO	59.59 ± 4.2	4			
1AO-2MD	132.3 ± 8.7	4	+	< 0.001	121.9
1AO-1MD	140.7 ± 24.4	4	+	0.005	136.0
2AO-1MD	91.63 ± 5.5	4	+	< 0.001	53.8
1AO-2MD	132.3 ± 8.7	4			
1AO-1MD	140.7 ± 24.4	4	=	0.578	6.4
2AO-1MD	91.63 ± 5.5	4	-	0.001	-30.7
1AO-1MD	140.7 ± 24.4	4			
2AO-1MD	91.63 ± 5.5	4	-	0.020	-34.9

Table 3. Summary of data from mixture tests

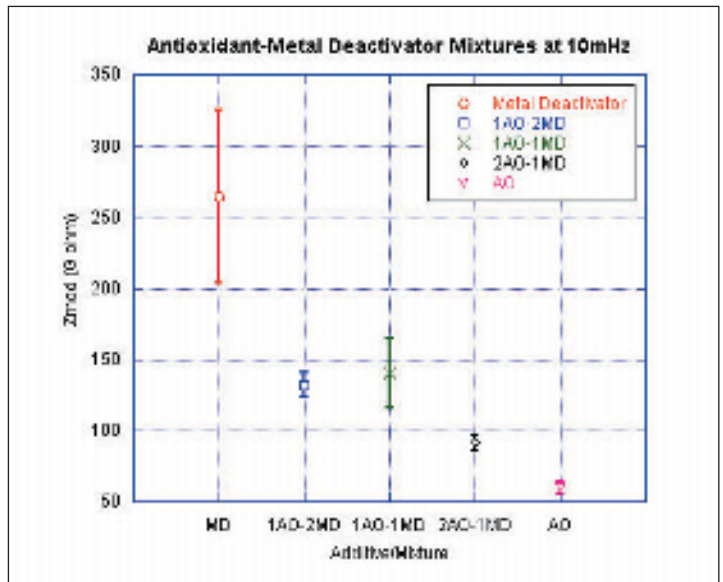


Figure 7. Mean values of the additives and mixtures with one standard deviation error bars. Each mixture was significantly different from each single additive, but only the 2AO-1MD mixture is significantly different from all other mixtures.

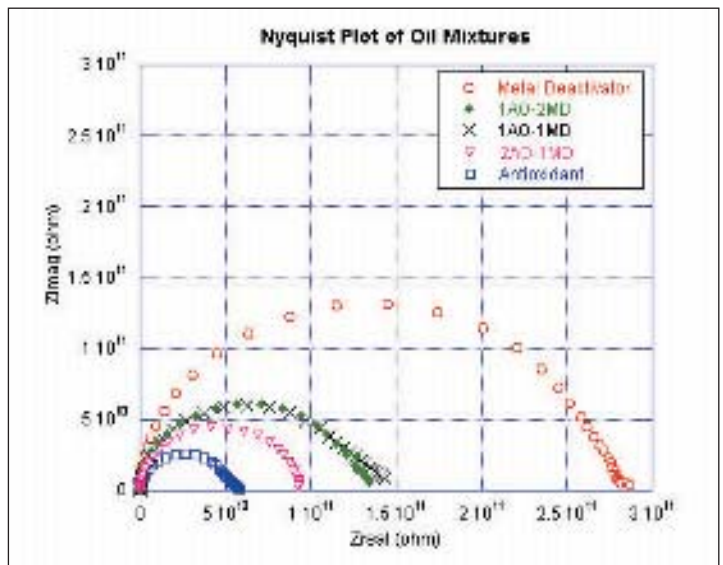
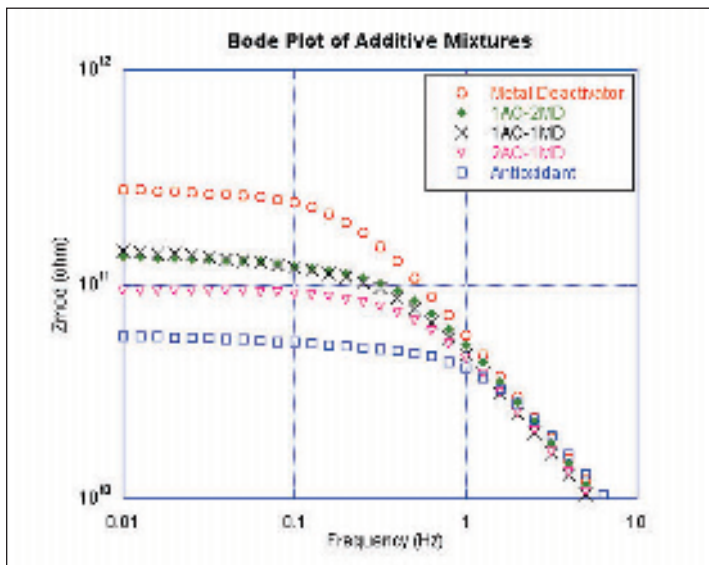


Figure 6. Bode and Nyquist plots of metal deactivator and antioxidant mixture data. The data from the straight metal deactivator and antioxidant additives is included. Only the low frequency data is shown on the Bode plot.

largest effect on impedance of all the additives. A comparison to the full formulation also indicates that the extreme pressure is not the only additive to have a significant effect but that there may be interaction between the additives in the full-formulation oil. Because each additive displays a higher mean magnitude, it is assumed that some interaction is occurring to cause the lower mean magnitude value displayed by a full-formulation.

For the 100 kHz data it can be seen that no difference is observed between the additives and both the basestock and the

full formulation. This frequency is insufficient for impedance testing. Figure 5 shows the mean impedance values for each additive, with error bars representing one standard deviation.

The mixture studies with metal deactivator and antioxidant were performed to understand additive interaction and the effect it has on impedance. The data for each of these is shown in Figures 6 and 7 and Table 3. Variance from the mean is one standard deviation. T-test values indicate statistical significance at 95% confidence; = indicates no statistical significance, +/-

indicate significantly higher or lower values. H_0 values indicate the t-probability associated with the paired t-test values showing confidence levels for all tests. The first group compares the tests to the metal deactivator, the second to antioxidant and the last two groups compare the mixtures to each other. The data presented here is for the test that was closest to the mean. Because the 100 kHz frequency point was shown (see Fig. 5) to be ineffective in detecting differences in impedance, this data was ignored for the mixture tests.

The data shows there is a difference between the two additives, that the mixtures are different from both additives, but that each mixture is not significantly different from one another. If there was no interaction occurring, it would be assumed that the impedance magnitude would vary with the mixing ratio (i.e. the magnitude in Figure 7 would be linear). This trend appears to be the case, except for the 1AO:2MD ratio. For this ratio, it is evident that the antioxidant additive has a stronger contribution to the impedance. If the additives were interacting, the impedance magnitude for the mixtures would be expected to be very different from the single additives (i.e. not have a value between the single additives). This was not observed for any of the mixtures in this study.

4. Conclusions

The amount of variance in data is different for each additive. High frequency tests do not show any significant difference between oils/oil-additive mixtures and are unsuitable for impedance response tests. Compared to the basestock oil only the extreme pressure additive and full formulation are significantly lower using a 95% confidence level. All additives are significantly different from the full-formulation. The mixtures of metal-deactivator and antioxidant do not indicate interaction; however, the antioxidant additive appears to have a stronger contribution to the impedance. The impedance values for these mixtures are proportional to the mixing ratio.

To aid in the development of a suitable equivalent circuit, a model derived from the physical mechanisms related to electronic conduction in oils will need to be addressed. The goal is to “simulate” the response of a fully formulated oil (and incorporate the effects of water content and Cl⁻ contamination). In addition, future work will be focused on identifying the contributions of the interfacial reactions on the impedance.

Acknowledgements

This research was performed at Boise State University with a grant from Pratt & Whitney. Thanks to Herb Chin, Bill Ogden and Curtis Genay of Pratt & Whitney and Ron Yungk of BP.

Drs. Darryl P. Butt and Brian M. Marx were contributing faculty on this project.

References

- [1] Barsoukov, E.; Macdonald, J.R. *Impedance Spectroscopy Theory, Experiment and Applications*, 2005, 2 ed., Hoboken, NJ: John Wiley & Sons.
- [2] Lvovich, V. F.; Smiechowski, M. F. “Impedance characterization of industrial lubricants,” *Electrochimica Acta*, 2006, In Press, Corrected Proof.
- [3] Wang, S. S.; Lee, H. S. “The application of a.c. impedance technique for detecting glycol contamination in engine oil,” *Sensors and Actuators B: Chemical*, 1997, 40, 193-197.
- [4] Allahar, K. N.; Butt, D. P.; Orazem, M. E.; Chin, H. A.; Danko, G.; Ogden, W.; Yungk, R. E. “Application of Measurement and Equivalent Circuit Modeling to High Impedance Data of Steels in Used Oil,” *Electrochimica Acta*, 2006, 51, 1497-1504.
- [5] Box, G. E. P.; Hunter, J. S.; Hunter, W. G. *Statistics for Experimenters*, 2005, 2 ed., Hoboken, NJ: John Wiley & Sons.

About the Author



Matthew Luke is a senior at Boise State University. He will graduate in December of 2007 with a BS in Materials Science and Engineering with emphasis in Electrical Engineering and a minor in Physics. He currently works for Dr. Darryl Butt in the Advanced Materials Lab doing research in electrochemistry and sensor development for Pratt & Whitney. He is a native of Boise, ID. Matt is married and he and his wife have one daughter.

Ruthenium Coordination Chemistry: Implications for Directed Carbon Nanotube Assembly

Thomas J. Younts

University of North Carolina at Charlotte, Department of Chemistry
9201 University City Blvd, Charlotte, NC 28223

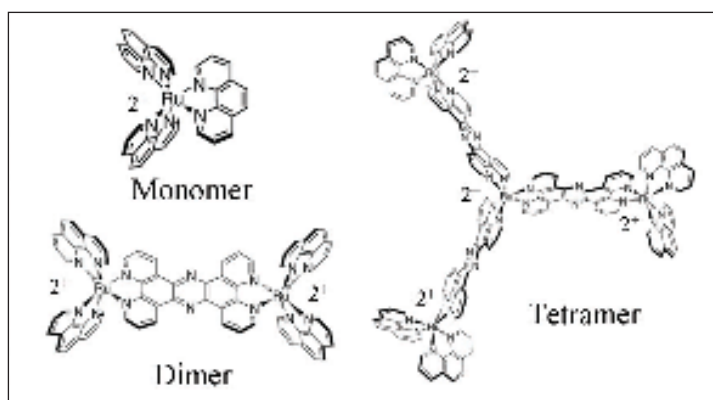
Abstract

Ruthenium coordination chemistry is studied for its usage as a building block for constructing supramolecular coordination complexes. Our laboratory focuses on how nanometer sized ruthenium structures interact with single walled carbon nanotubes (SWCNTs) with implications for directed nano-structure assembly. Understanding aspects of carbon nanotube assembly involves synthesizing ruthenium coordination complexes with various morphological and electrostatic properties. For example, various ruthenium dendrimers, each of which differs in shape and overall cationic charge, can be synthesized. Progress towards synthesizing a ruthenium trimer is reported. The central unit to the trimer, $[\text{Ru}(\text{phendione})_2\text{phen}]^{2+}$, was successfully created in high purity. $[\text{Ru}(\text{phen})_2\text{phendiamine}]^{2+}$, the peripheral monomer implemented in trimer synthesis, was not attained. However, precursor to the peripheral unit, $[\text{Ru}(\text{phen})_2\text{phendione}]^{2+}$, was synthesized. Since ruthenium monomers are built from various diimine ligands, syntheses of these ligands are also presented. Taken together, we possess half the starting material needed to create the trimer that will be utilized for carbon nanotube aggregation studies.

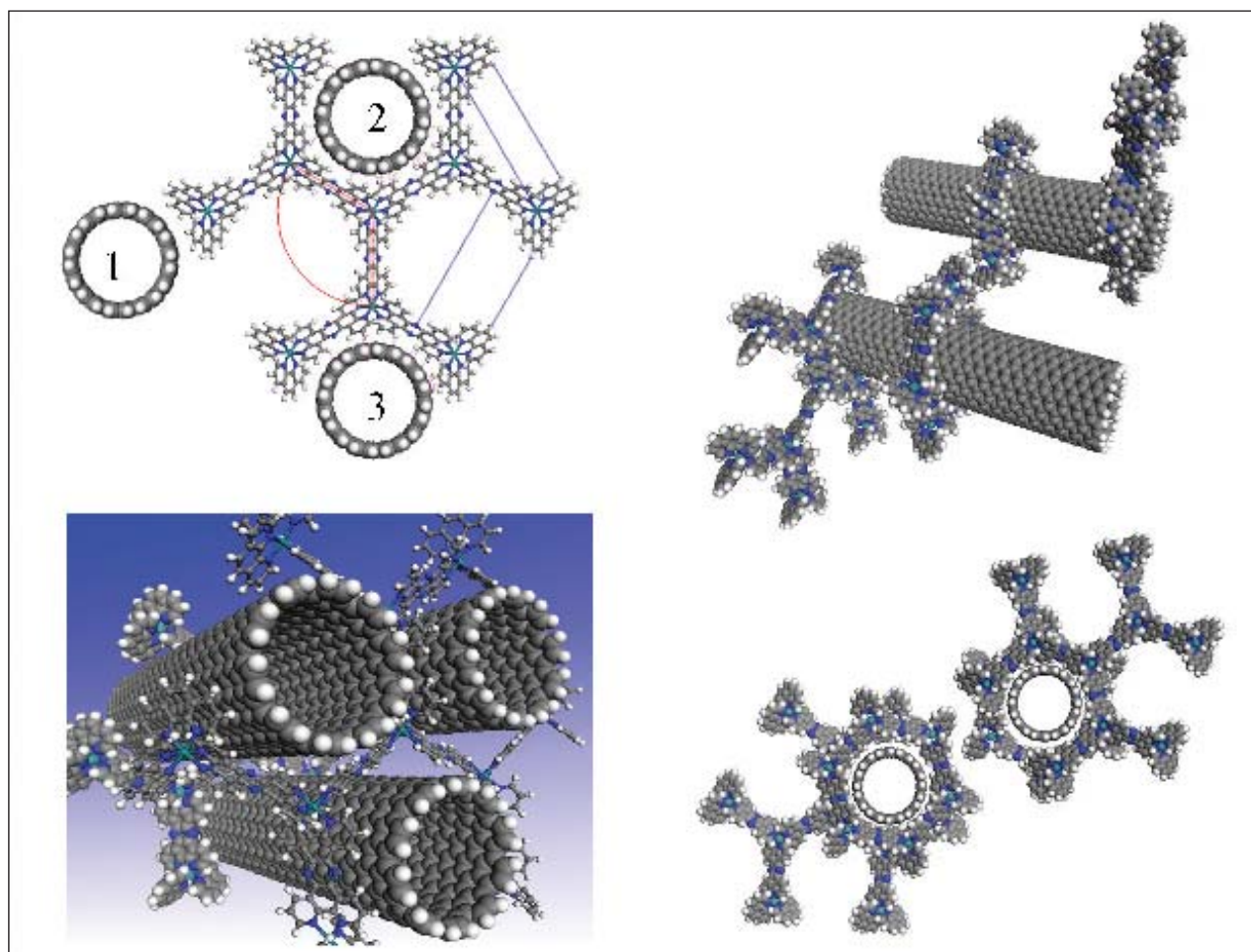
Keywords: Ruthenium, Coordination, Trimer, Carbon Nanotube

1. Introduction

Nanotechnology has wide implications ranging from nano-devices for effective drug delivery systems^[1] to colloidal sciences whereby carbon nanotube self-assemblies can be induced.^[2] Our laboratory is focused on the latter, whereby single walled carbon nanotube (SWCNT) aggregates can be utilized for electrical devices^[3] and photovoltaics.^[4] The self-assembly processes are studied by coagulating carbon nanotubes with various inorganic salts and ruthenium complexes. Several ruthenium coordination complexes are schematized below (Scheme 1), and are referred to as ruthenium monomer, dimer, and, tetramer; the number of ruthenium centers in the complex dictates the dendrimer's name. Importantly, each complex has specific morphological and electrostatic properties.



Scheme 1. Ruthenium Coordination Complexes Possessing Unique Morphological and Electrostatic Properties. Top left: ruthenium monomer with +2 charge. Bottom left: dimer with +4 charge. Right: tetramer with +8 charge.



Scheme 2. Ruthenium Supramolecular Interactions with SWCNTs. (Top left) SWCNTs can bind decamer at one of three locations as shown. (Bottom left) Modeling the assembly of a three tube guide-rail for structures 1000 times stronger than steel. (Right) Modeling the assembly of a nano-gearbox with mechanical parts. Perspective (top right) and edge on (bottom right) views of two SWCNTs rotating through the ratchet motion of ruthenium decamer and the torque transferred to the second SWCNT through a series of gears.

Previous studies from our laboratory revealed an enantiomerically pure ruthenium metallodendrimer $[\Delta_6\Delta_3\Delta\text{-Ru}_{10}]^{20+}[\text{PF}_6^-]_{20}$ to bind strongly and specifically to SWCNTs.^[21] Given its ten ruthenium centers, this large ruthenium complex known as the decamer, was much more effective at coagulating SWCNTs as compared to the monomer, and these observations have been attributed to the stark differences between shape and ionic charge. Scheme 2 (top left) illustrates supramolecular interactions thought to occur between ruthenium decamer and carbon nanotubes. The remainder of the scheme implicates prospective nano-technological devices.

A current goal of our laboratory is to synthesize various ruthenium compounds intermediary to ruthenium monomer and decamer and study their interactions with carbon nanotubes. We discuss the synthesis of a ruthenium trimer (Scheme 3). Synthesizing the rigid, electrically coupled ruthenium trimer is accomplished by first synthesizing various ruthenium monomers with specific diimine ligands (for examples of diimine ligands, see Scheme 4). We report the successful synthesis of the tri-

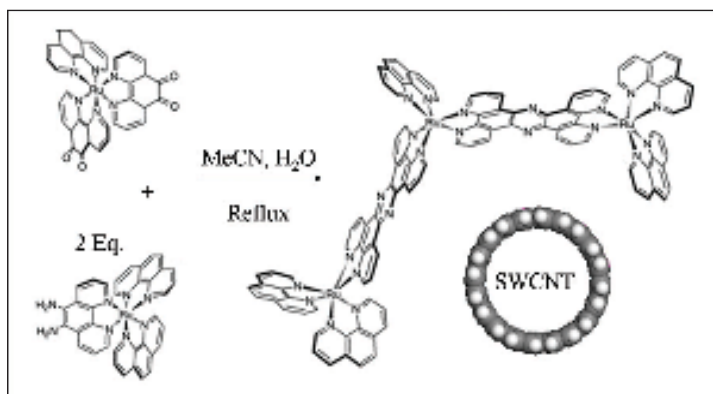
mer's central unit, ruthenium *bis*-1,10-phenanthroline-5,6-dione 1,10-phenanthroline $\{[\text{Ru}(\text{phendione})_2\text{phen}]^{2+}\}$. Although we were unable to achieve the peripheral unit, ruthenium *bis*-1,10-phenanthroline 1,10-phenanthroline-5,6-diamine $\{[\text{Ru}(\text{phen})_2\text{phendiamine}]^{2+}\}$, its precursor ruthenium *bis*-1,10-phenanthroline 1,10-phenanthroline-5,6-dione $\{[\text{Ru}(\text{phen})_2\text{phendione}]^{2+}\}$ was synthesized. Taken together, we possess half the starting material needed to create the trimer.

2. Procedures

The following synthetic procedures were modified from primary literature, and references to the literature are provided where applicable.

2.1 1,10-phenanthroline

This heterocyclic compound was purchased stock (Sigma-Aldrich). Fourier Transform-Infrared (FT-IR): 1419, 1501, 1586



Scheme 3. Synthetic Strategy for Ruthenium Trimer. Two molar equivalents of $[\text{Ru}(\text{phen})_2\text{phendiamine}]^{2+}$ (shown at bottom left) reacted with one molar equivalent $[\text{Ru}(\text{phendione})_2\text{phen}]^{2+}$ (shown at top left) yields the rigid, electrically coupled ruthenium trimer. Trimer has bent geometry that can wrap around SWCNTs.

and 3369 cm^{-1} . 300 MHz ^1H NMR (CDCl_3), ppm: 9.209, 9.194 (d, 2H); 8.278, 8.251 (d, 2H); 7.809 (s, 2H); 7.671, 7.656, 7.644, 7.628 (dd, 2H). See Results and Discussion for presentation of these data.

2.2 1,10-phenanthroline-5,6-dione^[5,6]

Liquid N_2 was poured around a beaker containing 20 ml 18M H_2SO_4 and stir bar. The solution was swirled until chilled (approximately -10°C), at which point liquid N_2 was removed, and 1.000 g (5.04 mmol) finely powdered phen added. While phen dissolved, liquid N_2 was poured around the beaker to ensure mixture remained about -10°C . Next, 5.147g (50.0 mmol) NaBr was added and the mixture warmed to room temperature. Br_2 vapors evolved during this time; no vapors were present after ~ 1 hr. 10 ml 16 M HNO_3 was subsequently added drop-wise after pouring contents into 500 ml round bottom flask. The mixture was refluxed 3 hrs. Vapors (*Caution: Toxic Fumes*) were allowed to escape after reflux to reveal yellow liquid. Contents were poured into 400 ml dH_2O and neutralized with $\sim 37\text{g}$ Na_2CO_3 . Four extractions were performed with 100 ml CH_2Cl_2 . Organic layers were saved and solvent removed. Residue was recrystallized from warm MeOH, rinsed with Et_2O after retrieving crystals, and dried under vacuum. Yield 60-70%. FT-IR: 1413, 1458, 1559, 1683, and 3061 cm^{-1} . 300 MHz ^1H NMR (CDCl_3), ppm: 9.141, 9.125 (d, 2H); 8.534, 8.507 (d, 2H); 7.624, 7.610, 7.597, 7.583 (dd, 2H). See Results and Discussion for presentation of these data.

2.3 1,10-phenanthroline-5,6-dioxime^[7]

0.420 g (2.00 mmol) phendione, 0.486 g (7.00 mmol) $\text{NH}_2\text{OH}\cdot\text{HCl}$, and 0.593 g (3.00 mmol) BaCO_3 were placed in 30 ml EtOH, stirred, and refluxed for 5 hrs. After removing the solvent, residue was treated with 0.2 M HCl, stirred for 30 minutes and filtered to give a light yellow/green solid. The sample

was washed with H_2O , EtOH, Et_2O , and dried to give a 25% yield. Being an intermediate, this compound is not presented in the Results and Discussion section.

2.4 1,10-phenanthroline-5,6-diamine^[7]

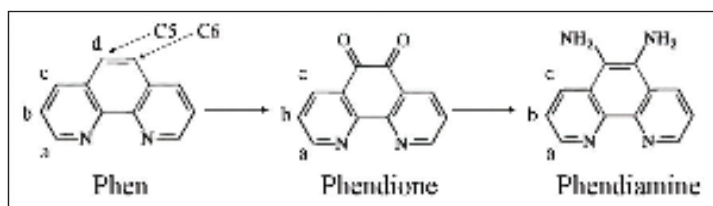
0.400 g (1.66 mmol) phendioxime and 0.400 g Pd-C (10%) were placed in 100 ml 100% (dry) EtOH, purged with Argon, and heated to reflux. 3.50 ml $\text{N}_2\text{H}_4\cdot\text{H}_2\text{O}$ was added to 15 ml dry EtOH, and over the course of 1 hr, this mixture was added drop-wise to the reaction flask. The mixture was refluxed 12 hrs, filtered hot through a bed of celite, and then rinsed with 20 ml portions of boiling EtOH. The filtrate was taken to dryness, the residue triturated prior to adding 30 ml H_2O , and left at 4°C overnight. It was then filtered, washed with cold H_2O , and dried to reveal tan solid. Yield 23%. FT-IR: 1435, 1484, 1561, 1606, 1725, 2925, and 3222 cm^{-1} . 300 MHz ^1H NMR ($\text{CH}_3\text{D}_2\text{O}$), ppm: 8.832, 8.816 (d, 2H); 8.627, 8.600 (d, 2H); 7.767, 7.750, 7.738, 7.724 (dd, 2H). See Results and Discussion for presentation of these data.

2.5 Ruthenium(1,10-phenanthroline)₂Cl₂·2H₂O and Ruthenium(1,10-phenanthroline-5,6-dione)₂Cl₂·2H₂O^[8]

One molar equivalent $\text{RuCl}_3\cdot 3\text{H}_2\text{O}$ was added to 2.1 molar equivalents phen (or phendione) along with LiCl (in excess of 10^3 moles), and placed under Argon. 50 ml DMF was carefully added and refluxed with stirring for 8 hrs. 250 ml acetone was then added and the resulting mixture cooled overnight. Black micro-crystalline products were observed. The crystalline products were filtered, washed with H_2O , Et_2O , and dried *in vacuo*. Being an intermediate, this compound is not presented in the Results and Discussion section.

2.6 [Ruthenium(1,10-phenanthroline)₂(1,10-phenanthroline-5,6-dione)][PF₆]₂ and [Ruthenium(1,10-phenanthroline-5,6-dione)₂(1,10-phenanthroline)][PF₆]₂^[9]

$\text{Ru}(\text{phen})_2\text{Cl}_2\cdot\text{H}_2\text{O}$ or $\text{Ru}(\text{phendione})_2\text{Cl}_2\cdot\text{H}_2\text{O}$ was heated at reflux for 3 hrs with 1.2 molar equivalents of phendione or phen, respectively, in thoroughly deaerated 1:1 EtOH: H_2O . After cooling and stirring for 30 minutes, the complex was



Scheme 4. Synthetic Outline for Diimine Ligands. Carbons 5 and 6 are highlighted on phen. ^1H NMR assignments are shown for phen, phendione, and phendiamine. Compare letters labeled above to letters labeled on ^1H NMR spectra of Figure 1.

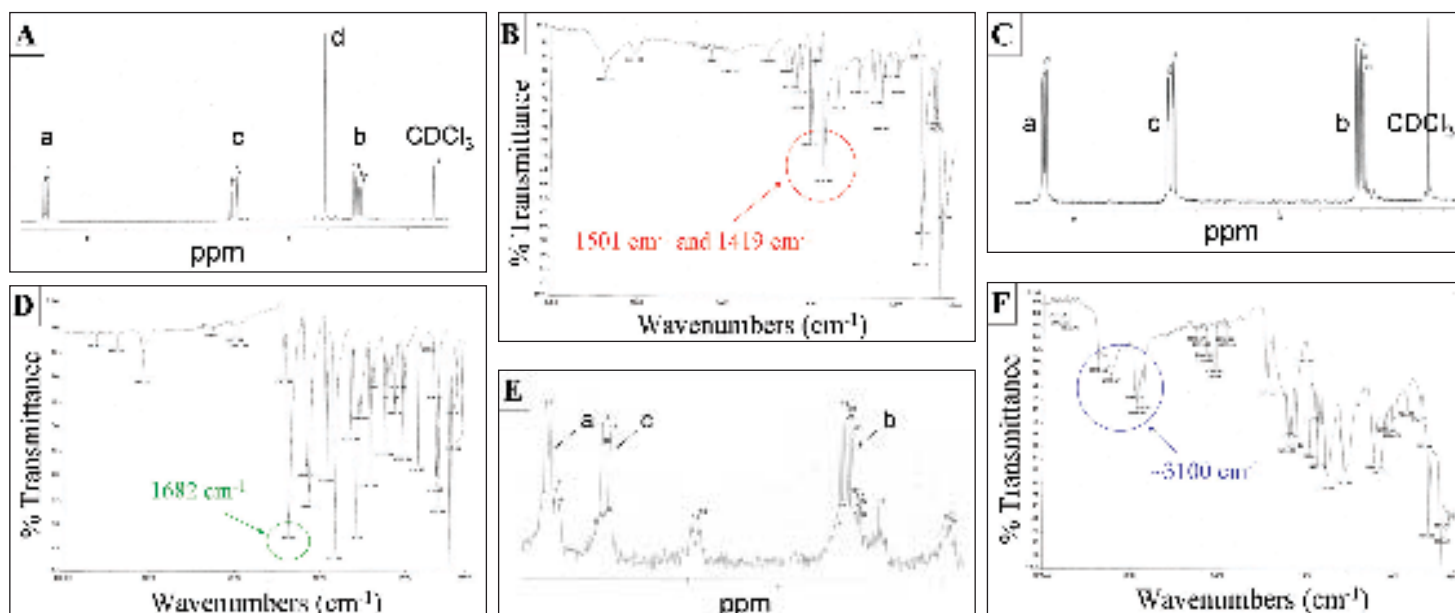


Figure 1. ^1H NMR and FT-IR Spectra of Phen, Phendione, and Phendiamine. (a) ^1H NMR of phen recorded in CDCl_3 . (b) FT-IR peaks at 1501 cm^{-1} and 1419 cm^{-1} correspond to $\text{C}=\text{C}$ stretching and $\text{C}-\text{H}$ bends, respectively, at the five and six positions of phen (circled in red). (c) ^1H NMR of phendione recorded in CDCl_3 . (d) $\text{C}=\text{O}$ phendione absorption peak appears at 1682 cm^{-1} (green circle) as detected by FT-IR. (e) ^1H NMR of phendiamine recorded in CD_3CN . Unidentifiable peaks are present. (f) FT-IR of phendiamine. Blue circle highlights $\text{N}-\text{H}$ or $\text{O}-\text{H}$ stretching around 3100 cm^{-1} . NMR proton assignments for each compound are shown in Scheme 4.

precipitated by addition of saturated NH_4PF_6 aqueous solution. Brown solid was produced which was filtered, washed with H_2O , Et_2O , and dried under vacuum. Crystallization with acetonitrile/ether may be used to further purify. Electrospray ionization mass spectrometry (ESI-MS) confirmed synthesis of these compounds. See Results and Discussion for presentation of these data.

3. Results and Discussion

3.1 Diimine Ligands Synthesized for Ruthenium Coordination Chemistry

Ruthenium has an octahedral binding domain, and therefore three diimine ligands can be coordinated to ruthenium. Diimine ligands we coordinated to ruthenium include 1,10-phenanthroline-5,6-dione (phendione), which contains two carbonyls at the five and six positions, and 1,10-phenanthroline-5,6-diamine (phendiamine), which contains two amines at the five and six positions. Both phendione and phendiamine are synthesized from precursor 1,10-phenanthroline (phen). See Scheme 4 for the synthetic strategy and placement of carbonyls and amines at the five and six positions.

We optimized the oxidation of phen to phendione by modifying literature procedures.^[5,6] ^1H NMR and FT-IR spectra of phen and phendione are shown in Fig. 1, both of which correspond to literature values.^[6,10] By examining ^1H NMR and

FT-IR spectra, it is possible to track the conversion of atoms within molecules, and in this case, the emergence of two oxygen atoms in place of two hydrogen atoms at the five and six positions. Note ^1H NMR of phen in Figure 1a. The singlet peak labeled “d” corresponds to hydrogen atoms at the five and six positions (compare with Scheme 4), and this peak is no longer present in ^1H NMR of phendione (Fig. 1c). FT-IR of phen (Fig. 1b) reveals absorption peaks at 1501 cm^{-1} and 1419 cm^{-1} which correspond to $\text{C}=\text{C}$ stretching and $\text{C}-\text{H}$ bends at the five and six positions, respectively. If phendione was synthesized, absorption peaks inherent to phen should not be present in FT-IR whereas absorption peaks specific to phendione should be present. FT-IR confirmed the presence of carbonyls (Fig. 1d) specific to phendione, indicating phen was oxidized to phendione.

After synthesizing phendione from phen, attempts were made to synthesize phendiamine from phendione^[7] as outlined in Scheme 4. Figure 1e and 1f show ^1H NMR and FT-IR, respectively, of phendiamine. Similar spectral observations have been observed elsewhere.^[11,12] Noisy baseline of ^1H NMR was observed due to solubility issues of the isolated compound; unidentified compounds are present in addition to phendiamine. FT-IR absorption peaks characteristic of phendiamine occur at 3100 cm^{-1} (Fig. 1f, blue circle), representing either $\text{N}-\text{H}$ or $\text{O}-\text{H}$ stretching. It is difficult to determine exactly which peaks in the range of 3100 cm^{-1} represent $\text{N}-\text{H}$ or $\text{O}-\text{H}$ stretching because of their similar absorptions. Based on ^1H NMR and

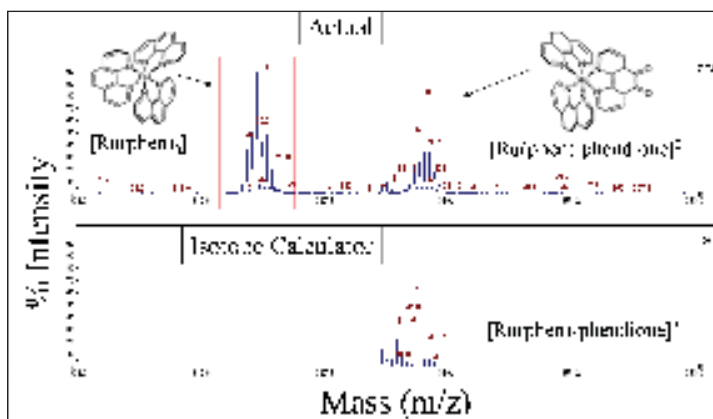


Figure 2. ESI-MS of $[\text{Ru}(\text{phen})_2\text{phendione}]^{2+}$ recorded in Acetonitrile. Two major products are $[\text{Ru}(\text{phen})_3]^{2+}$ and $[\text{Ru}(\text{phen})_2\text{phendione}]^{2+}$ as emphasized by red rectangles in the top spectrum. Schematics of each compound are shown. Computerized isotope calculator illustrates mass spectrum of $[\text{Ru}(\text{phen})_2\text{phendione}]^{2+}$ shown at bottom. Other byproducts were present in complete mass spectrum (not shown), some of which were derivatives of $[\text{Ru}(\text{phen})_2\text{phendione}]^{2+}$.

FT-IR spectra of these three diimines, we were able to synthesize pure phendione from phen; phendiamine was synthesized, but samples were not pure.

3.2 Coordinating Diimine Ligands to Ruthenium: Creating Monomers

With pure samples of phen and phendione, ruthenium coordination chemistry was pursued, and work towards the hexa-valent ruthenium trimer began (Scheme 3). Recall two molar equivalents of $[\text{Ru}(\text{phen})_2\text{phendiamine}]^{2+}$ must be reacted with one molar equivalent of $[\text{Ru}(\text{phendione})_2\text{phen}]^{2+}$ to produce the rigid structure.^[13] Therefore, each of these monomers^[9] must first be synthesized. Peripheral monomeric units, $[\text{Ru}(\text{phen})_2\text{phendiamine}]^{2+}$, were pursued first. Although this molecule was not attained, its precursor $[\text{Ru}(\text{phen})_2\text{phendione}]^{2+}$ was made. We plan to aminate this precursor^[7] to give $[\text{Ru}(\text{phen})_2\text{phendiamine}]^{2+}$ using similar procedures outlined in Scheme 4.

Analyzing syntheses of ruthenium monomers was accomplished with electrospray ionization mass spectrometry (ESI-MS). When examining mass spectra of ruthenium compounds, two salient features of spectra can be used to positively identify ruthenium complexes. First, approximately eleven ruthenium isotopes exist in nature, and each isotope has a relative abundance. Expanded view in Figure 3b shows the distinguishing ruthenium isotope pattern. Note approximately 11 peaks are present. Each peak does not correspond to a different compound. Rather, the entire group of eleven peaks corresponds to one compound. Consider an example with chlorine. Had a compound containing chlorine been analyzed by ESI-MS, only

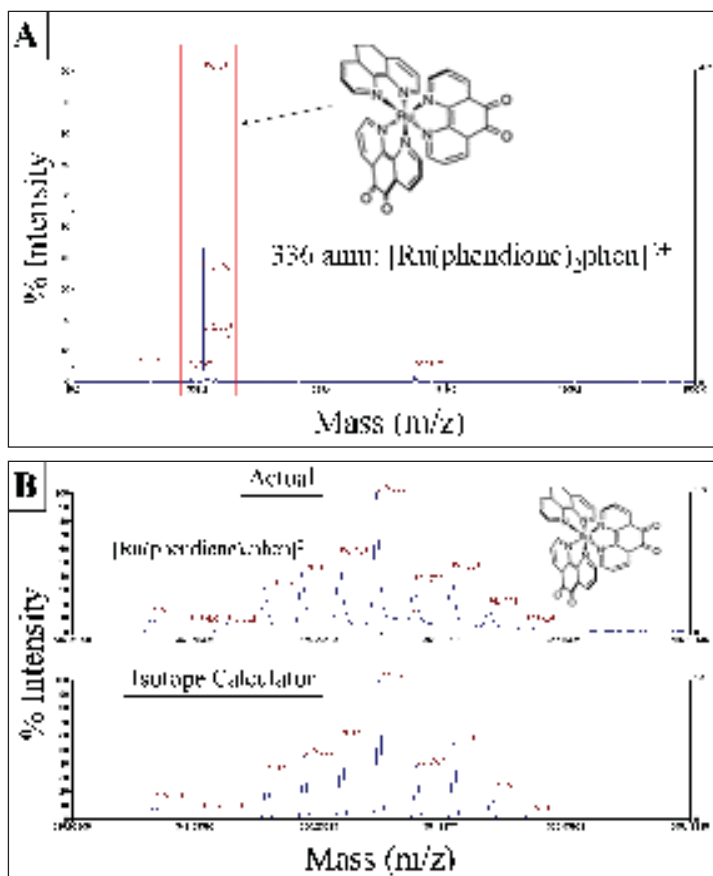


Figure 3. ESI-MS of $[\text{Ru}(\text{phendione})_2\text{phen}]^{2+}$ recorded in Acetonitrile. (a) Complete spectrum reveals $[\text{Ru}(\text{phendione})_2\text{phen}]^{2+}$ as major product (red rectangle). Small peak at 192 amu is solvent. At far right, 847 amu is $\{[\text{Ru}(\text{phendione})_2\text{phen}]^{2+}[\text{PF}_6]^{-}\}^{1+}$ that did not completely ionize. Very little $[\text{Ru}(\text{phen})_3]^{2+}$ was byproduced. (b) Expanded view of region highlighted by red rectangle. Actual and calculated spectra of $[\text{Ru}(\text{phendione})_2\text{phen}]^{2+}$ are presented.

two peaks, each corresponding to the two chlorine isotopes, would be observed. Therefore, compounds containing ruthenium are easily identified by the characteristic peak pattern. The second feature of all mass spectra containing ruthenium compounds is that the numerical difference between two isotope peaks is related to mass to charge ratios. If the difference between two peaks is 0.5 amu, the ruthenium species is a +2 ion; a difference of 1 amu corresponds to +1 ruthenium species. See discussion below for further details on interpreting ESI-MS.

Major byproduct obtained during the synthesis of $[\text{Ru}(\text{phen})_2\text{phendione}]^{2+}$ was $[\text{Ru}(\text{phen})_3]^{2+}$. Figure 2 highlights an expanded region of the complete mass spectrum. The complete mass spectrum has been omitted for clarity. At top, two groups of peaks are observed. Bond-line diagrams of $[\text{Ru}(\text{phen})_3]^{2+}$ and $[\text{Ru}(\text{phen})_2\text{phendione}]^{2+}$ indicate ruthenium

monomers. Using a computerized isotope calculator, a calculated mass spectrum was created for $[\text{Ru}(\text{phen})_2\text{phendione}]^{2+}$ and is shown at bottom for comparison. Notice the actual and calculated isotope patterns for $[\text{Ru}(\text{phen})_2\text{phendione}]^{2+}$ are coincident, indicating successful synthesis of $[\text{Ru}(\text{phen})_2\text{phendione}]^{2+}$.

Synthesis of the central unit, $[\text{Ru}(\text{phendione})_2\text{phen}]^{2+}$, was successful, and a complete mass spectrum of $[\text{Ru}(\text{phendione})_2\text{phen}]^{2+}$ is shown (Fig. 3). The largest group of peaks corresponds to desired product (Fig. 3a, red rectangle). Figure 3b is an expanded view of the red rectangle shown in Figure 3a. An isotope calculator confirmed successful synthesis of $[\text{Ru}(\text{phendione})_2\text{phen}]^{2+}$. Actual mass spectrum is at top whereas computed spectrum is illustrated at bottom. In addition to ruthenium's defined isotope pattern, the numerical difference between isotope peaks is 0.5 amu, signifying +2 cation. Trimer construction is halfway complete at this point; the central monomeric unit of the trimer, $[\text{Ru}(\text{phendione})_2\text{phen}]^{2+}$, was successfully synthesized.

4. Conclusions

Understanding supramolecular binding interactions between various ruthenium coordination complexes and SWCNTs is a goal for our laboratory. Specifically, we are focusing on directed assemblies of SWCNTs. Ruthenium complexes ranging in molecular morphology and cationic charges have been shown to interact with SWCNTs differently.^[2] Elucidating carbon nanotube directed assembly processes may be accomplished by synthesizing novel ruthenium compounds with various morphological and electrostatic properties.

Synthesis of a ruthenium trimer was pursued based on the pathway outlined in Scheme 3. Several diimine ligands were first synthesized and coordinated to ruthenium prior to trimer construction. Phendione was successfully created from its precursor phen; phendiamine synthesis was not synthesized in high purity. Ruthenium coordination chemistry was pursued using diimine ligands phen and phendione. Relatively pure $[\text{Ru}(\text{phendione})_2\text{phen}]^{2+}$, the central unit of the trimer, was synthesized. We also created $[\text{Ru}(\text{phen})_2\text{phendione}]^{2+}$. Samples were not pure, but can easily be purified using column chromatography. Therefore, we possess half the ruthenium monomers needed to create the trimer. After synthesizing the trimer, interactions of this coordination complex with SWCNTs will be studied.

Acknowledgements

Much appreciation is given to the Department of Chemistry faculty at the University of North Carolina at Charlotte for

providing exceptional learning experiences. Special thanks to Jordan Poler, Ph.D., Jon Merkert, Ph.D., and James Crosthwaite, Ph.D., for serving on my honors thesis committee; this research was conducted in partial fulfillment of the requirements for Honors in the Department of Chemistry. I extend my warmest encomiums to Dr. Poler, who supervised this work, for inviting me to join his laboratory.

References

- [1] Ghalanbor, Z.; Marashi, S.; Ranjbar, B. *Med Hypotheses* **2005**, *65*, 198.
- [2] Chaturvedi, H.; Poler, P. *J Phys. Chem. B* **2006**, *110*, 22387.
- [3] Guo, X.; Huang, L.; O'Brien, S.; Kim, P.; Nuckolls, C. *J. Am. Chem. Soc.* **2005**, *127*, 15045.
- [4] Guldi, D.; Rahman, G.; Prato, M.; Jux, N.; Qin, S.; Ford, W. *Angew Chem Int Ed* **2005**, *44*, 2015.
- [5] Hiort, C.; Lincoln, P.; Norden, B. *J. Am. Chem. Soc.* **1993**, *115*, 3448.
- [6] Yamada, M.; Tanaka, Y.; Yashimoto, Y.; Kuroda, S.; Shimao, I. *Bull. Chem. Soc. Jpn.* **1992**, *65*, 1006.
- [7] Bodige S.; MacDonnell F. *Tetrahedron Letters* **1997**, *38*, 8159.
- [8] Sullivan, B.; Salmon, D.; Meyer, T. *Inorg. Chem.* **1978**, *17*, 3334.
- [9] Goss, C.; Abruna, H. *J. Am. Chem. Soc.* **1985**, *24*, 4263.
- [10] Calderazzo, F.; Marchetti, F.; Pampaloni, G.; Passarelli, V. *J. Chem. Soc., Dalton Trans.* **1999**, 4389.
- [11] Kleinewischede, A.; Mattay, J. *Eur. J. Org. Chem.* **2006**, 947.
- [12] Bolger, J.; Gourdon, A.; Ishow, E.; Launay, J. *Inorg. Chem.* **1996**, *35*, 2937.
- [13] MacDonnell, F.; Kim, M.; Wouters, K.; Konduri, R. *Coordination Chem. Rev.* **2003**, *242*, 47.

About the Author



Thomas Younts was born in Greensboro, NC and moved to Charlotte in 2002 to pursue baccalaureate degrees in Psychology and Biology. He has research experiences in psychology, biology, and chemistry. After graduating with Honors in Biology and Chemistry from the University of North Carolina Charlotte in 2007, Thomas will begin advanced studies at the Albert Einstein College of Medicine, where he plans to earn a Ph.D. in neuroscience. Thomas looks forward to a career in academia.

Percolation of Fibrous and Bimodal Fillers in Thermoreversible Gelcast Aluminum Oxide

Kristina Bond

University of Illinois Urbana-Champaign, Department of Materials Science and Engineering
1304 W. Green St., Urbana, IL 61801

Abstract

A novel pore morphology was developed by addition of fugitive fibers to a thermoreversible gel slurry to induce pores in alumina (Al_2O_3) samples. Through density measurements by the Archimedes' method and SEM images the percolation threshold for fibers with aspect ratios of 37 and 120 was found to be less than 1 vol% fibers. Introducing two spherical fillers with different diameters (3.5:1 diameter ratio) to create bimodal filler has a small effect on the percolation threshold, if any. More research is needed to understand the effect of bimodal fillers on the pore morphology.

Keywords: Alumina, Gelcast, Bimodal Fillers

1. Introduction

A ceramic is an inorganic, brittle solid, composed of at least two elements, one of which must be a non-metal. Commonly, these ceramics are carbides, oxides, and nitrides of elemental metals or semiconductors. By nature, ceramics are strong, hard, generally non-reactive, and have very high melting temperatures. They have very low thermal and electrical conductivity.^[1]

These properties are useful in applications that require high strength in high-temperature and/or highly corrosive environments, such as heat exchangers,^[2] many kinds of filters,^[3,4] catalyst supports,^[5] composite preforms,^[6] and biomedical implants.^[7-9] All of these applications require a high surface area within the material, which is achieved by creating a pore network. Pores can be induced by adding organic fillers which are later removed. Other methods of pore forming include partial sintering and the addition of foaming agents.^[10]

Different pore sizes and shapes are necessary for different applications. This study seeks to develop a pore morphology, or network, that is different from spherical pore morphology by introducing fibrous and bimodal filler materials at various concentrations. New network geometries will yield materials with unique mechanical, thermal, and transport properties.

Because of their very high melting temperatures, it is impractical for most applications and sometimes impossible (as in some carbides which dissociate instead of melting) to melt and cast a ceramic. Instead, solid state processing is often used. Shape forming for solid state processing can be accomplished by direct casting, in which the ceramic powder and organic binder are added to a liquid medium and mixed into slurry. The slurry is cast into a mold and is allowed to dry before proceeding to the burnout process. During burnout, the part is heated at a controlled rate which depends on the composition of the organic binders and fillers in the green body. The organics, including fillers for pore introduction, will decompose and leave only the intended pore network in the pure ceramic skeleton. The final step is to sinter the ceramic at a very high temperature, usually above 1000°C , to complete the particle consolidation and densification of the skeleton surrounding the pores. Direct casting methods are near net-shape processes, so the final part typically does not require significant machining or finishing.

Gelcasting is a direct casting method in which the liquid and binder form a gel. Traditional gelcasting is limited because the slurry gels through an irreversible polymerization reaction, and therefore, can only be cast within a short time after the reac-

tion catalyst has been introduced. A variant of this method, thermoreversible gelcasting (TRG), has been developed at Northwestern University.^[11-13] TRG uses the selective solubility of an acrylate tri-block copolymer dissolved in alcohol to form a gel through a physical transition instead of a chemical reaction. The tri-block copolymer has a poly(*n*-butyl acrylate) (PnBA) midblock and two poly(methyl-methacrylate) (PMMA) endblocks. Below the critical micelle temperature (CMT), the PMMA endblocks become insoluble and form micelles. The soluble midblocks effectively cross link the micelles, forming a gel network. The physical transition is reversible, so the gel can be reheated and recast over and over again.^[11] Thermoreversible gelcasting has additional advantages over traditional gelcasting because it is oxygen insensitive, uses safer chemicals, permits for early preparation in producing a slurry, and allows for recycling of flawed castings.

2. Procedure

A thermoreversible gel was made by combining 5 vol% tri-block polymer (PMMA₂₃-PnBA₃₁-PMMA₂₃, Kuraray Corporation, Japan) and 95 vol% pentanol (99+%, Alfa Aesar) in a glass vial, then ultrasonating the mixture in a Branson 2510 Ultrasonicator at 75 °C until dissolved. The solution was removed from the ultrasonicator, and aluminum oxide (Al₂O₃) with 0.05 mol% magnesium oxide (MgO) powder (Baikowski Malakoff, North Carolina), and the filler were added in four equal loads, each added after the previous load had completely dispersed after ultrasonication at 75 °C. Filler concentrations, in vol% of total solids, ranged from 0.5 to 5 vol% polypropylene (PP) or polyethylene fibers (PE) (Minifibers), or 25 to 40 vol% PP bead-corn starch mixture. The sizes and aspect ratios of these fillers are listed in Table I. A dispersant (Aerosol® AY 65 (sodium diamyl sulfosuccinate in ethyl alcohol) Cytec, New Jersey) was added in equal parts at the first and third solids loadings: 2 wt% for bimodal filler or 3 wt% for fiber filler.

	Diameter	Length	Aspect Ratio
Polypropylene Fiber	30	1.1	36.7
Polyethylene Fiber	5	0.6	120
Corn Starch	10	-	1
Polypropylene Beads	35	-	1

Table I: Sizes and aspect ratios of filler materials

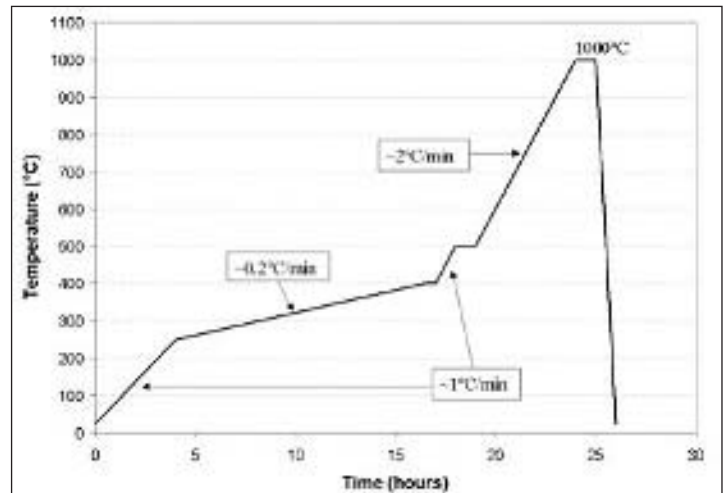


Figure 1. The burnout schedule of polypropylene fiber filler in a thermoreversible gelcast Al₂O₃

Nylon rings coated with Dow Corning Molykote 316 Silicone Release Fluid and glass slides with silicone-coated Mylar sheets (Richard E. Mistler, Pennsylvania) taped to the surface were heated on aluminum blocks in an oven at 70 °C. The glass slides were left on the aluminum blocks to keep them warm. The gel slurry was cast into the rings with a glass slide on either side, Mylar-side towards the mold. When the glass slides were cool to the touch, one slide was removed and the drying process began.

The drying process consisted of one day in a sealed, pentanol vapor environment, created by introducing a pentanol source into the sealed container. This was followed by one day in an air-tight environment (without the pentanol source), and then one day open to air.

Samples went through a burnout process that is customized to the composition of the organics. An example of the PP fiber burnout schedule is shown in Figure 1. The burnout schedules were determined from thermogravimetric analyses of the tri-block copolymer and fillers. A pre-sintering step at 1000 °C was incorporated to give the porous bodies some handling strength before the sintering process. All Al₂O₃ samples underwent the same sintering process as follows: 10 °C/min up to 1600 °C, a one-hour hold at 1000 °C, then 10 °C/min ramp rate down to room temperature (actual ramp rate is less than 10 °C/min at lower temperatures).

The bulk density (density of the overall sample), specific gravity (density of the ceramic skeleton), and apparent porosity of samples were found using ASTM Standard C373, commonly known as the Archimedes' method. Selected samples were sectioned and polished with 0.1 μm suspension to be imaged using a scanning electron microscope (Hitachi S3400), at a pressure of 70-100 Pa, using both backscattering electron (BSE) and environmental scattering electron detector (ESED) modes.

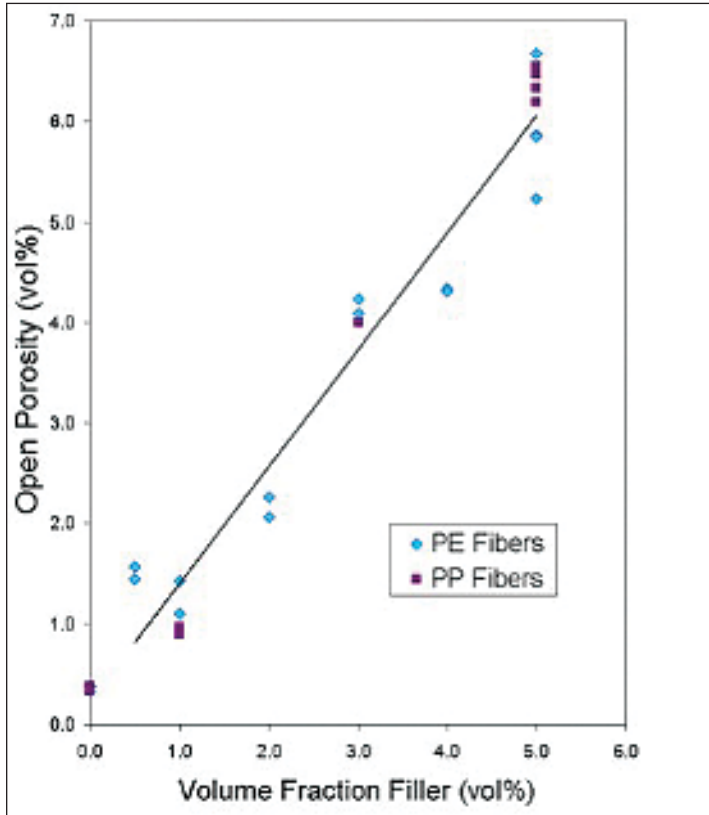


Figure 2. Open porosities of samples produced with polyethylene and polypropylene fibers as a function of volume percent filler

3. Results and Discussion

Pores can be classified as closed, where the individual pore or pore clusters are isolated from each other, or open, where each pore is connected to the pore network that spans the entire volume (a percolative network). A sharp boundary exists between closed and open porosity, known as the percolation threshold.

Percolation theory uses a statistical method to determine the minimum concentration of particles required to create a single, connected network in a multi-phase system. In the case of spherical, monodisperse particles in a simple cubic lattice, the percolation threshold is 31 vol%.^[14] The volume percent of filler material is not necessarily equal to the volume percent of the pores in the final material due to shrinkage of pores during the densification process. Percolation theory can also be useful for predicting results in non-spherical, polydisperse multi-particle systems. Since assumptions for statistical calculations and models outline ideal situations, it is necessary to evaluate pore network morphology and percolation thresholds under experimental conditions.

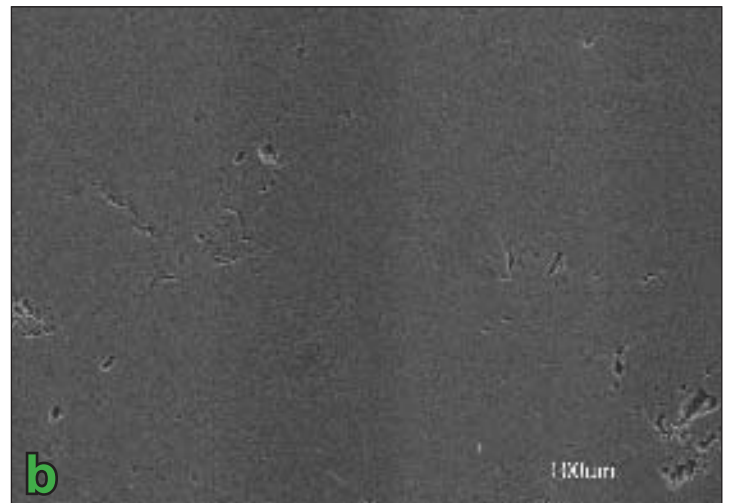
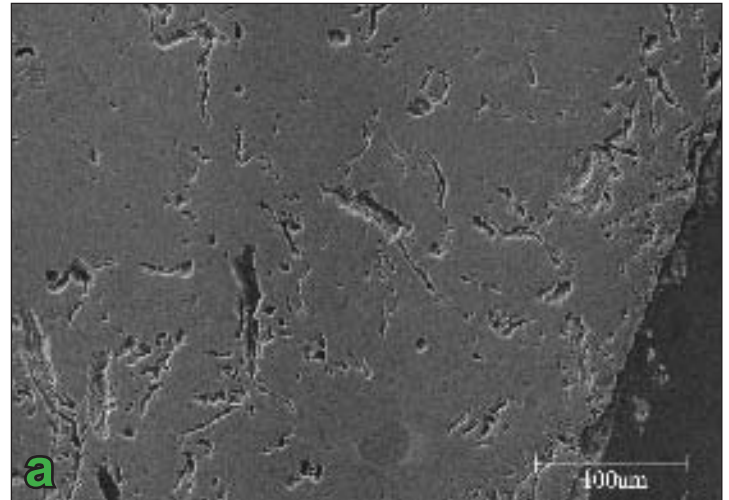


Figure 3. SEM cross-sectional images of porous Al_2O_3 produced with polyethylene fibers of random orientations at (a) 5 vol% and (b) 1 vol% fibers

3.1 Fiber Fillers

Open porosity as determined by the Archimedes' method is shown in Figure 2 for materials made with fugitive fillers of PP and PE fibers at concentrations between 0.5 and 5 vol%. The apparent porosity increases linearly with volume percent fiber and porosity is proportional to filler concentration, which implies that the percolation threshold is below 1 vol% fugitive filler; much less than the 31 vol% threshold of spherical fillers. The fibers act as pre-formed channels which connect into a network at a low concentration. This is an important result because the percolation is achieved while maintaining a very high ceramics concentration, which gives a stronger structure overall.

The randomly oriented pore structures of samples produced with 5 vol% and 1 vol% PE fibers are seen in SEM images, Figure 3. The two-dimensional images of a sectioned and polished surface do not properly show the percolation of three

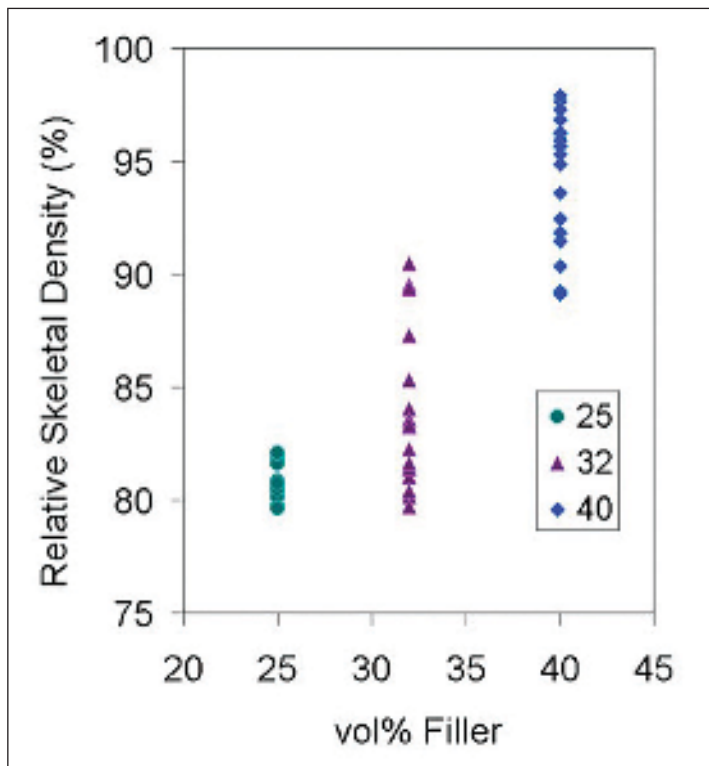


Figure 4. Relative skeletal density of samples produced with bimodal fillers of 25, 32, and 40 vol%

dimensions. The observed plane may not display a fully-connected network even when the volume of the sample shows that, through bulk density measurements, there is complete percolation. However, the SEM images are useful to show variation of filler particle sizes and approximate ratios by the two-dimensional pore shapes, as well as to confirm random orientation of the fibers in slurry.

Modeling studies reported the percolation threshold for ellipsoids with a large range of aspect ratios.^[15] Approximating fibers as high-aspect ratio ellipsoids, the threshold for a PE fiber (aspect ratio 37) should be between 2.6 and 1.5 vol%, and a PP fiber (aspect ratio 120) should reach percolation just below 0.69 vol%. Because the cited values were generated by modeling, the numbers assume a perfect percolative system with straight particles. The flexible polymer fibers used in this study do not form perfect ellipsoids because of size dispersion and fiber bending, and the effective aspect ratios are less than modeled in the study by Garboczi, et al.^[15] Although the PP and PE fibers have different aspect ratios, results show a similar behavior for both fibers due to fiber bending which reduces the relative difference between their aspect ratios.

3.2 Bimodal Fillers

It was expected that the percolation threshold of bimodal fillers will deviate from 31 vol% based on particle packing arguments. The density and porosity of samples produced with

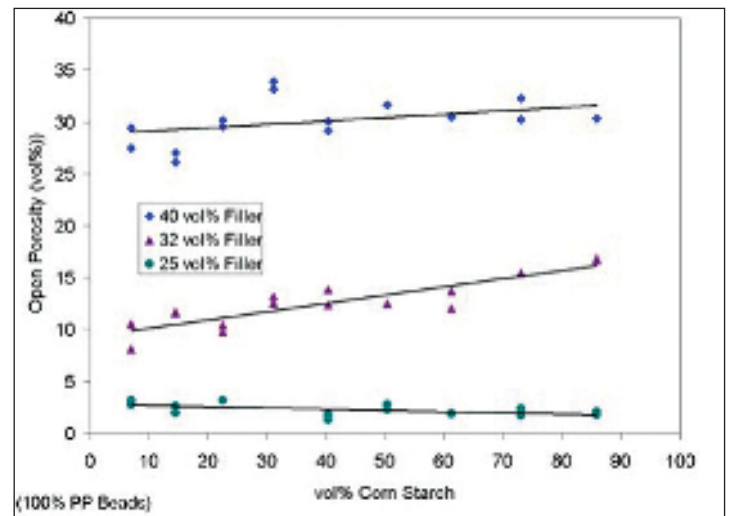


Figure 5. Open porosity as a function of cornstarch fraction for three levels of bimodal (cornstarch and polypropylene) filler

bimodal fillers at three volume percents (25, 32, and 40 vol%) are plotted in Figure 4 and 5, respectively as a function of corn starch to PP bead ratio. Because Archimedes' method interprets closed porosity as a decrease in apparent specific gravity, it is expected that the percent apparent specific gravity will decrease by a percentage approximately equal to the filler concentration if closed pores are present in the sample. This is exactly the case, for samples produced with 25 vol% filler, where the apparent specific gravity is between 79 and 82% of theoretical density. This represents 18-21 vol% closed pores, which is close to the concentration of fugitive filler. More evidence that these samples do not achieve percolation is the open porosity (Figure 5), which is ~3 vol% and less. The small amount of measured porosity could be due to surface roughness, surface cracks, or systematic error Archimedes' method, but <3 vol% porosity suggests a lack of percolation in the case of bimodal spherical fillers at 25 vol%. A SEM image of a samples produced with 25 vol% filler with 61.3 vol% corn starch is shown in Figure 6(a).

Samples with 32 vol% filler in Figure 4 have higher relative skeletal density than samples with 25 vol% filler, suggesting that there are relatively more open pores. It should be noted that corn starch has a large spread in particle size distribution, which could affect the spread of data in Figure 4. Figure 5 shows that samples produced with 32 vol% filler have porosities between 8 and 16 vol%, which are too large to be surface roughness or experimental error, but too small to have reached the percolation threshold. A network has begun to form, but there are still pores in isolation from the network. Although statistical percolation is a sharp transition, the experimental system is not ideal in particle shape and size distribution; thus porosity increases gradually as the filler concentration approaches the percolation threshold. The SEM image of a sample produced

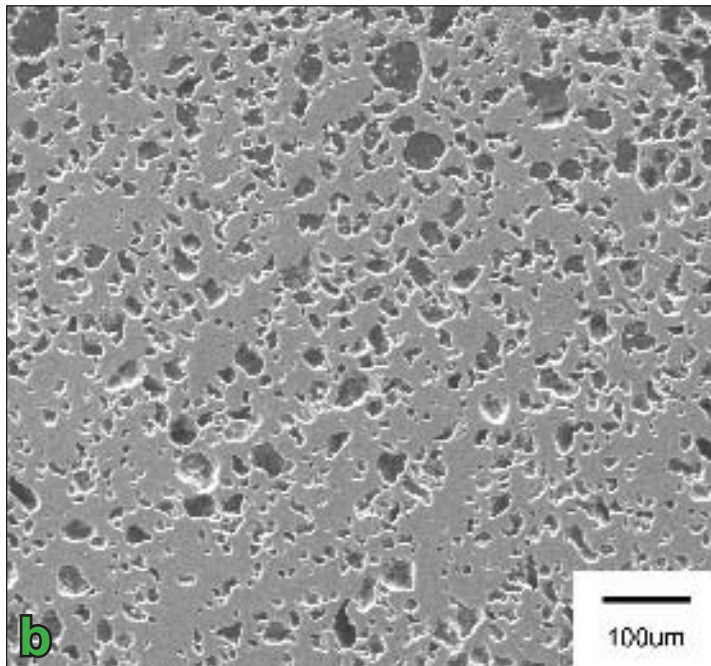
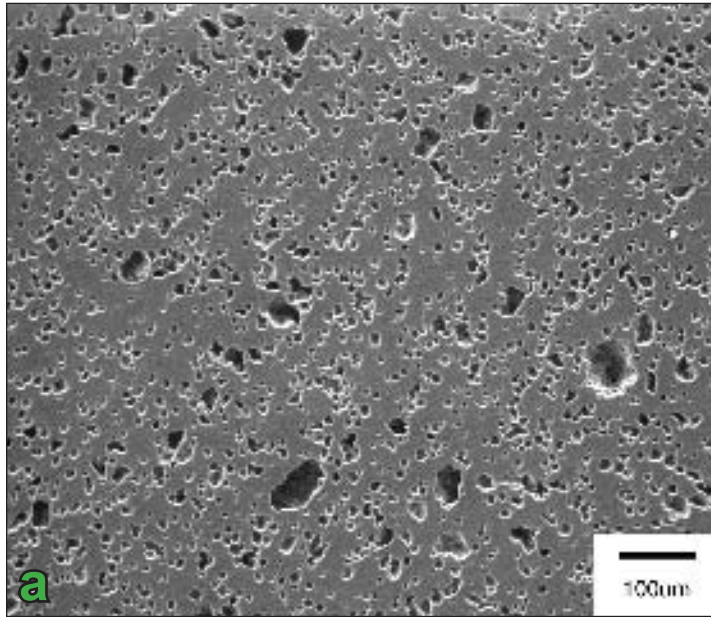


Figure 6: SEM cross sectional images of samples produced with bimodal filler at (a) 25 vol% filler with 61.3 vol% corn starch and (b) 32 vol% filler with 7.0 vol% corn starch. The percent of corn starch is the percent of total filler material.

with 32 vol% bimodal filler is shown in Figure 6(b).

Figure 4 shows the porosity of samples produced with 40 vol% filler to have between 89 and 98% specific gravity. The 2-11% spread from 100% density is attributed to the non-ideality of the bimodal fillers. As expected, there is evidence of percolation, although the data is not ideal. The hypothesis that the percolation threshold of bimodal fillers will deviate from 31 vol% cannot be confirmed or rejected.

4. Conclusions

It was found that fibrous fillers with aspect ratios of 37 and 120 reach the percolation threshold at less than 1 vol% filler. The results for both fibers are similar even though their aspect ratios differ by a factor of four. These results differ from the theoretically predicted result because the fibers are not ideal ellipsoids.

The percolation threshold of spherical bimodal fillers (3.5:1 diameter ratio) is between 32 and 40 vol% filler, but the effect of bimodal fillers as a function of particle size ratio is unclear. Any effect of bimodal fillers with size ratio 3.5:1 on percolation threshold is small due to a large particle distribution and non-ideal system. However, particle size distribution and shape appear to cause a more gradual transition from closed to open porosity instead of a sharp threshold.

Acknowledgements

Kristina would like to thank Noah O. Shanti and Dr. Katherine T. Faber for their guidance with the presented research, and the rest of the Faber group at Northwestern University for a wonderful summer in 2007. Research was funded by the National Science Foundation through the Research Experience for Undergraduates program.

References

- [1] Barsoum, M W. *Fundamentals of Ceramics*. Institute of Physics Publishing: London, 2003; pp 2-9.
- [2] Steen, M.; Ranzani, L.. Potential of SiC as a heat exchanger material in combined cycle plant. *Ceram. Int.* **2000**, *26*(8), 849-854.
- [3] Yank, L.; Ning, X.; et al. Preparation and properties of hydroxyapatite filters for microbial filtration. *Ceram. Int.* **2007**, *33*(3), 483-489.
- [4] Montanaro, L. Durability of ceramic filters in the presence of some diesel soot oxidation additives. *Ceram. Int.* **1999**, *25*(5), 437-445.
- [5] Kolodziej, A; Lojewska, J.. Short-channel structured reactor for catalytic combustion: Design and evaluation. *Chem. Eng. Process.* **2007**, *46*(7), 637-648.
- [6] Han, J.; Hong, C.; et al. Microstructural characterization and ablation mechanism of TiB₂/(Cu,Ni) melt-infiltrated ceramic composite. *Compos. Sci. Technol.* **2007**, *67*(11-12), 2231-2237.
- [7] Lacroix, D.; Prendergast, P. J.; et al. Biomechanical model to simulate tissue differentiation and bone regeneration: application to fracture healing. *Med. Biol. Eng. Comput.* **2002**,

- 40(1), 14-21.
- [8] Navarro, M.; Ginebra, M. P.; et al. (2004). Development and cell response of a new biodegradable composite scaffold for guided bone regeneration. *J. Mater. Sci.: Mater. Med.* **2004**, 15(4), 419-422.
 - [9] Von Doernberg, M. C., von Rechenberg, B.; et al. In vivo behavior of calcium phosphate scaffolds with four different pore sizes. *Biomaterials*. **2006**, 27(30), 5186-5198.
 - [10] Reed, J. S. *Principles of Ceramics Processing*, pp 206
 - [11] Drzal, P. L; Shull, K. R. (2003). Origins of Mechanical Strength and Elasticity in Thermally Reversible, Acrylic Triblock Copolymer Gels. *Macromolecules* **2003**, 36(6), 200-208.
 - [12] Montgomery, J. K., P. L. Drzal, et al. Thermoreversible Gelcasting: A Novel Ceramic Processing Technique. *J. Am. Ceram. Soc.* **2002**, 85(5), 1164.
 - [13] Montgomery, J. K., Botha, A. S.; et al. A thermoreversible gelcasting technique for ceramic laminates. *Scripta Mater.* **2003**, 48(6): 785-789.
 - [14] Stauffer, D. *Introduction to Percolation Theory*. Taylor & Francis: Philadelphia, PA., 1985; pp 17.
 - [15] Garboczi, E. J., Snyder, K.A.; et al. Geometrical percolation threshold of overlapping ellipsoids. *Phys. Rev. E.* **1995**, 52(1), 819.

About the Author



Kristina Bond is a Materials Science and Engineering student at the University of Illinois Urbana-Champaign, class of 2008. She is concentrating her undergraduate study in Biomaterials and plans to begin graduate school in biomedical engineering in the fall of 2008. Her hometown is

Shorewood, IL.

Evaluation of Bearing Steel Corrosion in Oil Contaminated with Synthetic Seawater

Brandon W. Christoffersen

Boise State University, Department of Materials Science & Engineering
1910 University Dr., Boise, ID 83725

Abstract

Lubricant systems in military aircrafts, operating in marine environments, experience corrosion due to seawater contamination. In particular, low chromium martensitic bearing and gear steels are susceptible to pitting corrosion attack in seawater-contaminated lubricants. Therefore, the corrosion performance of two advance bearing steels was assessed in this study. The steels were immersed in oil solutions and the corrosion results were analyzed as a function of seawater content and time. Optical image analysis was used to measure the pit density/size/distribution and an optical profiler was used to measure pit depth. It was found that while the pit surface fraction (pit surface area/total area) and pit depth increased with seawater content and time, the actual chloride content in the oil might have made a greater contribution to the corrosion damage.

Keywords: Pitting, M50 steel, profilometry

1. Introduction

Stainless steels are widely used for their corrosion resistance, especially in harsh environments.^[1] Chloride contaminated environments, in particular, can cause pitting corrosion and possible failure of steel including stainless steel parts. Even in protective oil, corrosion can still occur.^[2] Information pertaining to the protectiveness of oil towards corrosion can be very useful for many applications.

In order to quantify the effects of chloride concentration on corrosion rates in oil, tests were performed on M50 steel and carburized Pyrowear 675 stainless steel (P675) (provided by Pratt & Whitney), while varying the seawater concentration and studying the corrosion at different lengths of time (1 week and 1 month). Upon test completion, each sample was analyzed by optical image software to determine pit density (pits/area), average pit size, and surface fraction of pits. This was followed by optical profilometry to determine deepest pit depth. The results of these tests show the effect of chloride concentration and time on corrosion rate.

2. Experimental Procedure

Corrosion tests were run on ten M50 samples, and four P675 samples. M50 was tested at 0 water (with 5% seasalt), 500ppm seawater, 2500ppm seawater, 5% seawater, and 30% seawater in oil for both one week and one month. Pyrowear 675 was tested at 5% seawater and 30% seawater in oil for one week and one month. The seawater used in this study had 0.6 mole chloride content. Oil-seawater mixtures were made of Exxon 254 jet oil, ASTM D 1141-52 standard seasalt, and DI water. Prior to testing, all M50 samples were mounted in an epoxy resin and polished to a 1 μm polish. P&W supplied Pyrowear 675 samples with a 1 μm surface finish and no further polishing was performed. Samples were placed in sealable mason jars, with polished side up, containing the various oil/seawater solutions. The seawater-oil solutions were added until the sample surface was located approximately 1/3 depth from the bottom (Figure 1). Upon test completion, the samples were cleansed using a DI water sonic bath, acetone, methanol, and a DI water rinse.



Figure 1. (a) 14 samples stored in 7 sealed mason jars. (b) Close-up photo with a superimposed image indicating how the sample was positioned in the solution.

Analysis began with optical digital photos and micrographs taken on a Zeiss Axiovert 200 microscope. Multiple micrographs, at various magnifications and positions were taken of each sample to provide an overall representation of the surface. Three micrographs were selected for areal analysis. Areal analysis was performed using a Scion Image Alpha 4.0.3.2 instrument. Scion Image distinguishes pits based upon a given threshold value (a sample of an analyzed micrograph with pits shown in red can be seen in Figure 2). The threshold corresponds to the pit size and comparisons of the analyzed image and optical image were used to determine the appropriate threshold value. The Scion Image program was used to quantify the number of pits and the area and perimeter of each pit. It also measured the total size of the area being analyzed. From this data, pit density, average pit size, and the surface fraction that pits covered were determined.

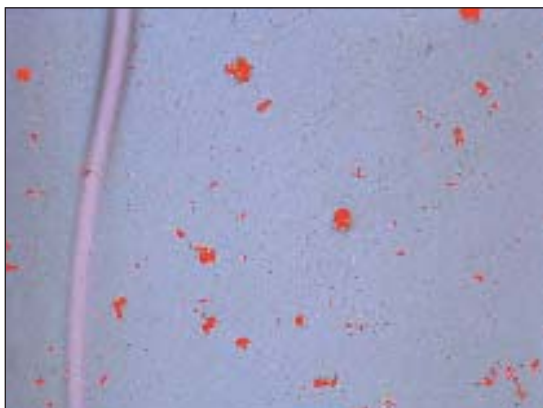


Figure 2. Analyzed micrograph of M50 sample from 2500ppm seawater in oil for 1 week

After analysis, each sample was then surface profiled on a WYKO NT1100 optical profiling system, using Vision 32 3.303 SMU4 Build 5 software by Veeco. Measurements of multiple pits were made to determine the deepest pit on each sample. The deepest pit depths were reported, not the average pit depths, in order to provide useful information regarding critical flaw size.

3. Results & Discussion

Micrographs of the samples can be seen in Figures 3-9. New oil is assumed to contain approximately 150ppm water. The amount of seasalt added is the same as the amount of seasalt that is present in the 5% seawater (0.6 M Cl) solution. This study was performed to understand what might happen if a large quantity of seawater contaminated the oil and then was evaporated off (leaving behind the salt).

As can be seen by the micrographs, only the M50 steel in 0 water, 500ppm, and 2500ppm samples can be analyzed for pitting damage. For the M50 steel, 5% and 30%, the corrosion was more severe and the pitting damage is difficult to quantify. The M50 samples displayed a filiform type of corrosion for the 2500ppm seawater samples, as seen in Figure 5.

Filiform corrosion is a type of crevice corrosion, and has mostly been observed under thin coatings of the organic type. It can most easily be described as worm-looking, with an actively corroding head and an inactive tail filled with corrosion products. Filiform corrosion is generally found to be superficial, and considered not to have a critical effect on the bulk.^[3] More study needs to be done to determine if the corrosion in Figure 5 is indeed a type of filiform corrosion, and therefore

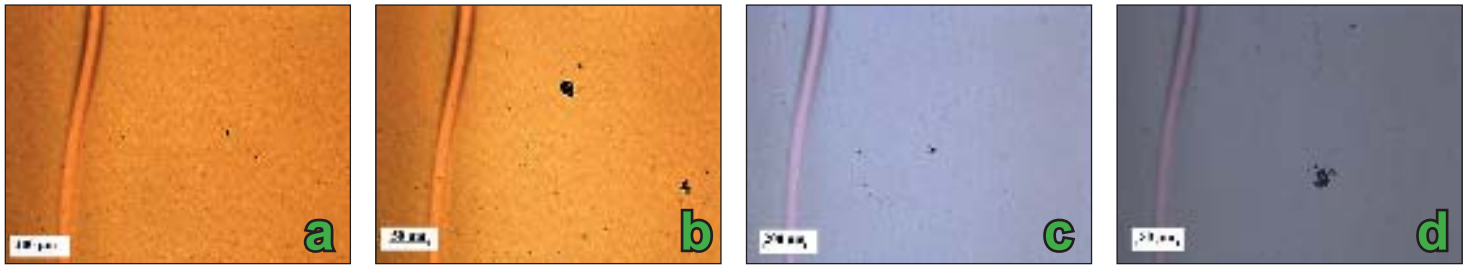


Figure 3. Micrograph of M50 in Oil with seasalt added (no water added) for 1 week, taken with Zeiss microscope (a) 1 week (b) 1 week (c) 1 month (d) 1 month

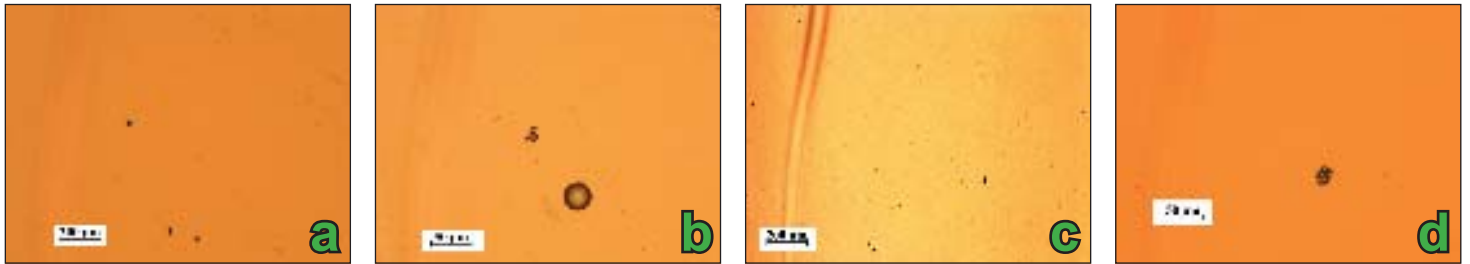


Figure 4. Micrographs of M50 in 500ppm Seawater for 1 week, taken with Zeiss microscope (a) 1 week (b) 1 week (c) 1 month (d) 1 month

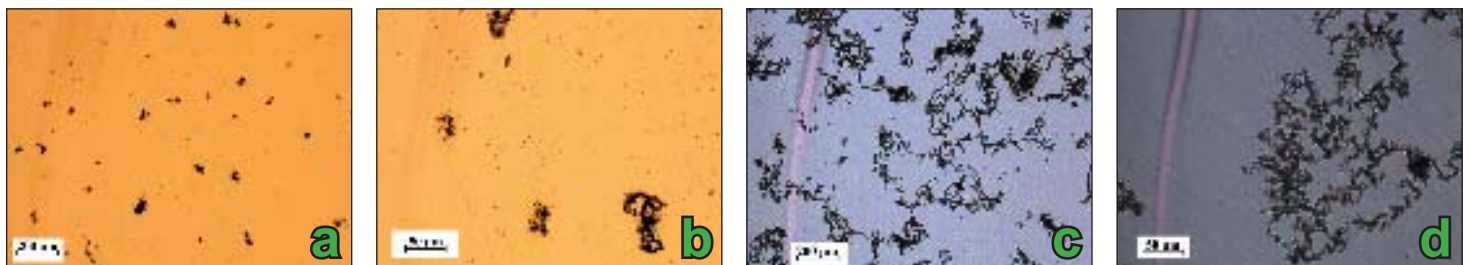


Figure 5. Micrographs of M50 in 2500ppm Seawater for 1 week, with Zeiss microscope (a) 1 week (b) 1 week (c) 1 month (d) 1 month

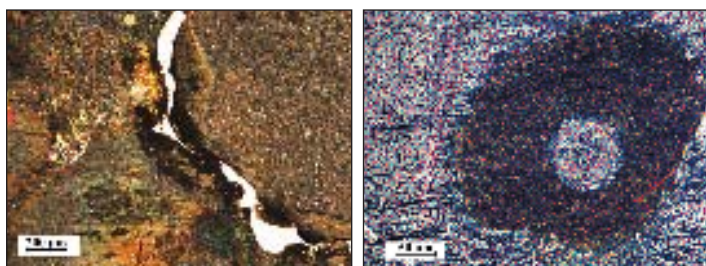


Figure 6. Micrographs of M50 in 5% Seawater for 1 week, taken with Zeiss microscope.

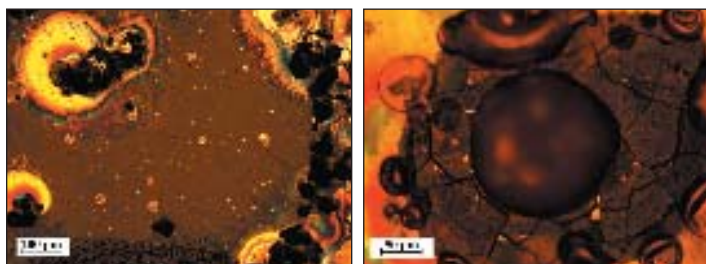


Figure 7. Micrographs of M50 in 30% Seawater for 1 week, taken with Zeiss microscope



Figure 8. Micrograph of Pyrowear 675 in 30% Seawater after 1 week, taken with Zeiss microscope

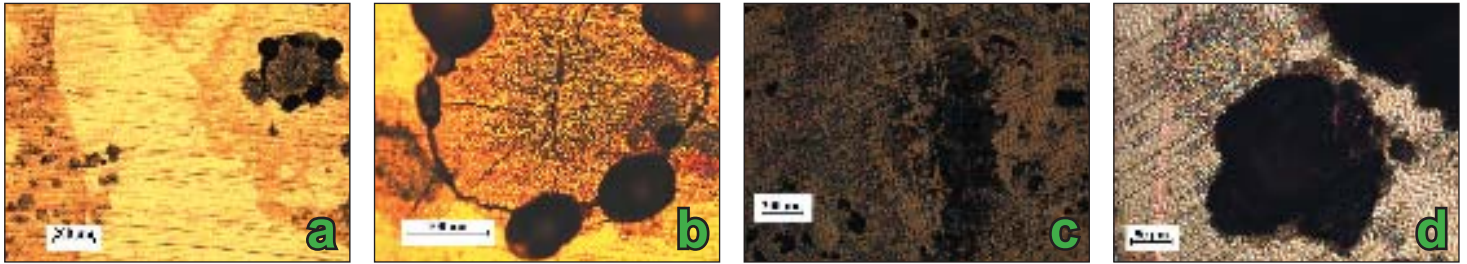


Figure 9. Micrographs showing the localized corrosion region on alloy 2 in 30% Seawater after 1 week, taken with Zeiss microscope (a) 1 week (b) 1 week (c) 1 month (d) 1 month

Seawater in Oil (ppm)	Pits per cm ² , 1 week	Pits per cm ² , 1 month
0	6411.7	30467
500	16977	9322
2500	26606	29173

Table 1. Pit density data collected through Scion Image analysis software

Seawater in Oil (ppm)	Average Pit Size (cm ²), 1 week	Average Pit Size (cm ²), 1 month
0	0.00359315	0.00230226
500	0.002917823	0.007781727
2500	0.00516334	0.063750395

Table 2. Average Pit sizes collected through Scion Image analysis software

Seawater in Oil (ppm)	Average surface fraction covered, 1 week	Average surface fraction covered, 1 month
0	0.0043285	0.0070152
500	0.0049357	0.0035867
2500	0.018819	0.13028

Table 3. Average surface fraction covered by pits, determined through Scion Image analysis software

determine how much or how little need for concern there is in these samples.

The transition from pitting to general/severe corrosion is suspected to be somewhere around 4000ppm, but more studies need to be conducted in that range.

For carburized Pyrowear 675 stainless steel, there was very little corrosion, as compared to M50 steel, though some pitting damage was observable. As mentioned, only the harshest conditions were studied at this point for P675 samples (5% and 30% seawater-oil solutions). Figure 8 represents the typical corrosion damage incurred on P675 samples; however P675 does display some localized corrosion phenomenon as depicted in Figure 9. Pitting was observed to initiate at grain boundaries on the samples as evidenced in Figure 9. The areas of attack are considered to be the steel matrix alloy adjacent to the chromium carbide precipitates, but further analysis is needed.

Pit density data (# pits/cm²) has been collected and is displayed in Table 1 and Figure 10. For the 1 week immersion time, a direct correlation can be seen between seawater content

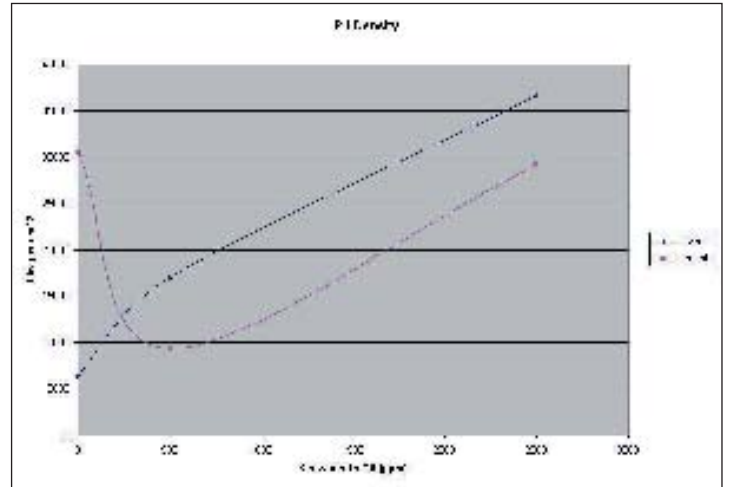


Figure 10. Number of pits per cm² in 0ppm, 500ppm, and 2500ppm seawater concentrations for 1 week and 1 month

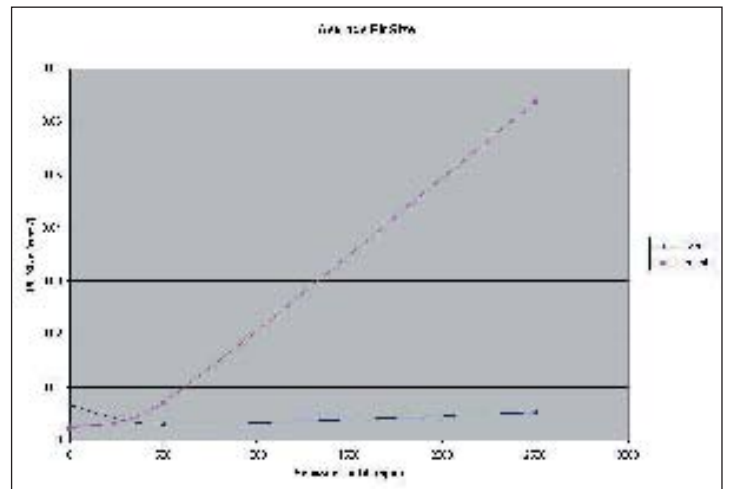


Figure 11. Average Pit Size (cm²) at 0ppm, 500ppm, and 2500ppm for 1 week and 1 month

and pit density. For the 1 month immersion time, the correlation is not as evident due to the coalescence of pits during pit growth (i.e. the number of pits decrease as multiple pits grow to form one larger pit).

Pit size data (pit area) is listed in Table 2 and is plotted in Figure 11. For the 1 month immersion time, there is a very strong correlation between seawater content and average size of pits, but for the 1 week immersion time, a direct trend of pit size to seawater concentration is not present. This indicates that pitting is not just an effect of seawater content, but also a function of the chloride content in the seawater. This is due to the fact that seasalt (not seawater) was added to the oil for the 0 “seawater added” solution, but there is approximately 150ppm water already present in the oil from air exposure. Therefore, the chloride concentration in this solution is much greater than the others, which might explain the excess pitting for the 1 week M50 sample. More studies, which consider various chloride concentrations in seawater, will need to be carried out to verify the correlation between chloride content and pitting damage.

Taking into account the fact that pits eventually grow together, the best way to express the aerial growth of pits is by quantifying the areal surface fraction occupied by pits. Surface fraction data is listed in Table 3 and plotted in Figure 12. Over the time period of 1 week, surface fraction increases from 0.0042 to 0.0189 as seawater content goes up from 0 to 2500ppm. Over 1 month time, the correlation is even stronger. Surface fraction increases from 0.0066 to 0.1860. This means that at 2500ppm seawater content, almost 19% of the surface is covered by pits after only 1 month time.

Seawater in Oil (ppm)	Deepest Pit Depth (microns), 1 week	Deepest Pit Depth (microns), 1 month
0	2.89	4.06
500	3.61	3.28
2500	2.79	6.6

Table 4. Average surface fraction covered by pits, determined through Scion Image analysis software

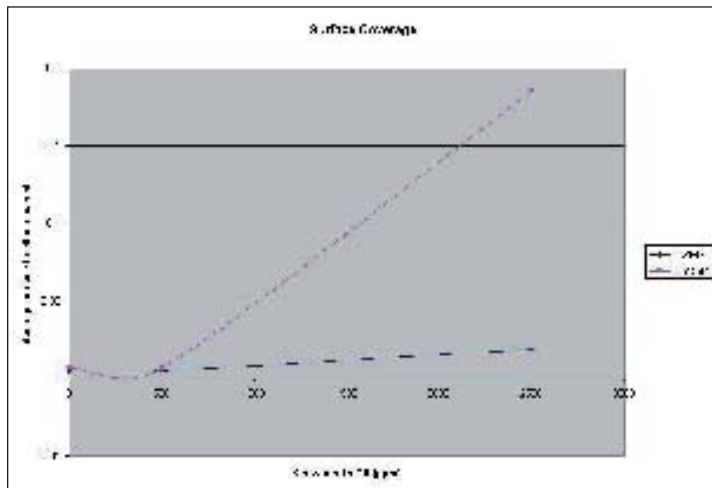


Figure 12. Average surface fraction covered by pits at 0ppm, 500ppm, and 2500ppm for 1 week and 1 month

Pit depths were measured using a WYKO NT1100 optical profiling system, using Vision 32 3.303 SMU4 Build 5 software by Veeco. The deepest pit depth data is presented in Table 4 and plotted in Figure 13. While pit depth would be expected to follow the same pattern as surface fraction, that does not appear to be the case. The pits at 0 water are much deeper than expected (around 4 microns deep). This is possibly due to the 150ppm water already present in the oil dissolving the added salt and making a very high chloride concentration seawater. This high chloride concentration seems to have as much or more of an effect on pit depth (and even pit size) than the seawater content has. For this solution, seasalt was directly added to the oil (not seawater). The amount of seasalt added is the same as the amount of seasalt that is present in the 5% seawater solution. This study was performed to understand what might happen if a large quantity of seawater contaminated the oil and then was evaporated off (leaving behind the salt).

The 2500ppm seawater content solution does not seem to cause pits to grow very deep early on but after 1 month’s time, they are as deep as 6.6 microns. Some of the optical analysis images are shown in Figures 14-16.

5. Conclusion

It has been found that surface fraction is the best way to quantify the pitting damage. Surface fraction of pitting has an obvious correlation with seawater content and time. Pit depth also shows a correlation with seawater content and time, but seawater content and time are not the only factors in pit growth. It has been shown that higher molarity of the seawater causes larger and deeper pits, and may be more crucial to pit depth

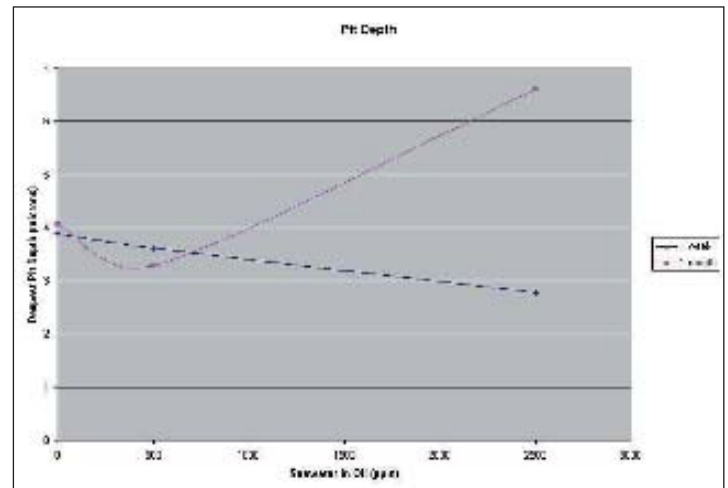


Figure 13. Deepest pit found per sample through optical profilometry

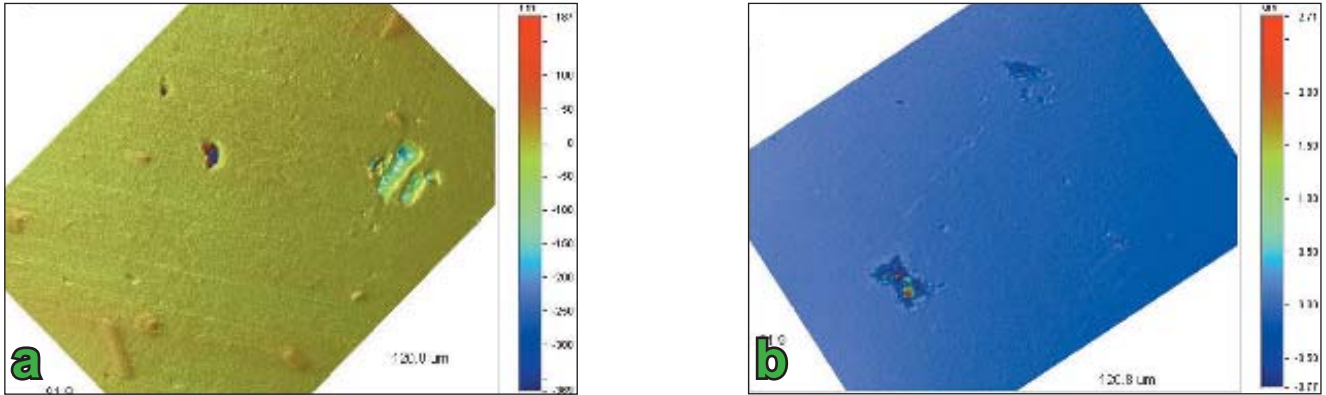


Figure 14. Optical profilometry images used to quantify pit depths in M50 after being immersed in 0ppm seawater added (≈ 150 ppm water present in the oil) for (a) 1 week (b) 1 month

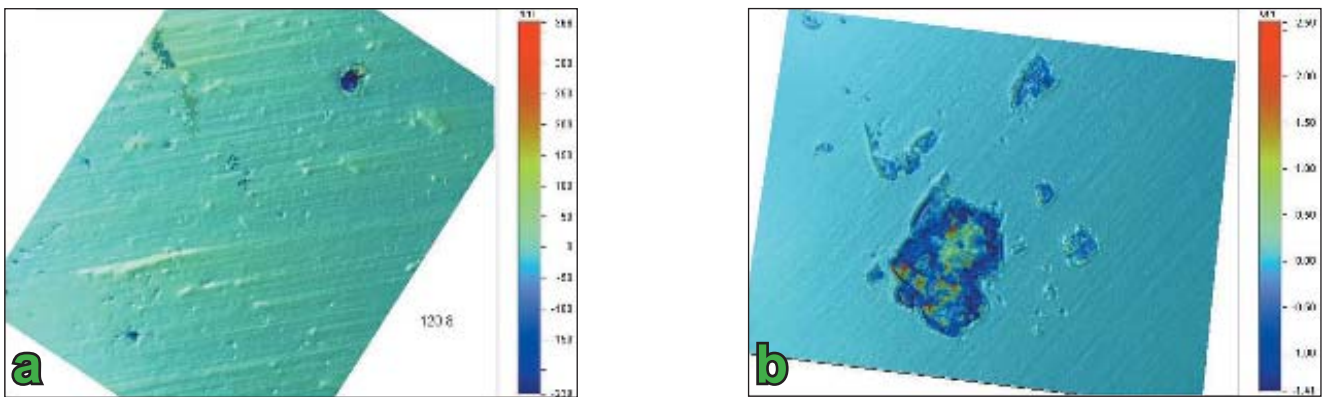


Figure 15. Optical profilometry images used to quantify pit depths in M50 after being immersed in 500ppm seawater (0.6 M Cl^-) + oil solution for (a) 1 week (b) 1 month

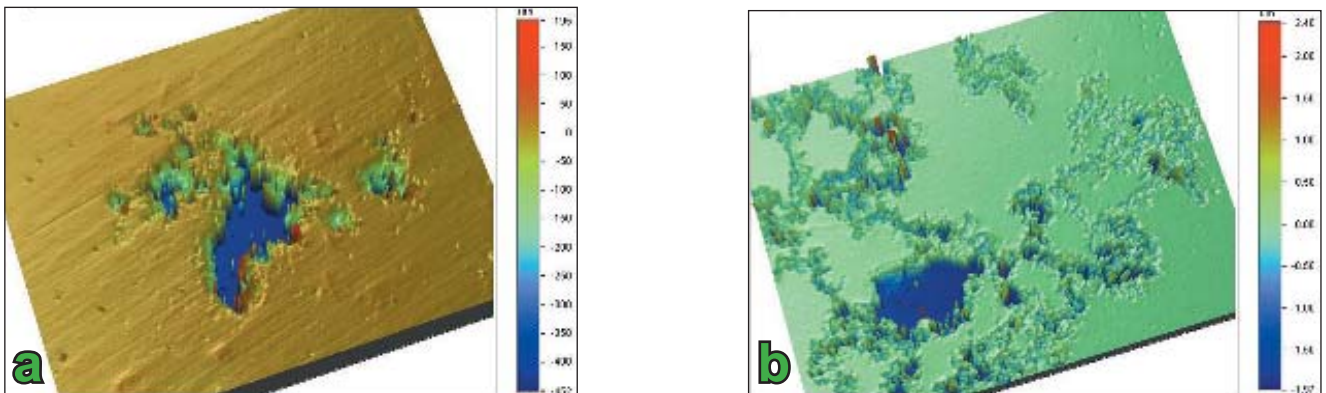


Figure 16. Optical profilometry images used to quantify pit depths in M50 after being immersed in 2500ppm seawater (0.6 M Cl^-) + oil solution for (a) 1 week (b) 1 month

than seawater content. A note should be made that there is an obvious corrosion resistance advantage in P675 as compared to M50.

Acknowledgements

This work was done at Boise State University under supervision of Dr. Darryl P. Butt, with help from the following group members: Post Docs: Dr. Brian Marx and Dr. Abdel Salam Maklouf; Students: Mathew Luke, Gordon Balfour, Brian Jaques, Patrick Callahan, and Prakash Periasamy.

Thanks to Pratt & Whitney for financial support, and special thanks to Herb Chin, Bill Ogden, and Curtis Genay of Pratt & Whitney. Thanks to Dr. Sean Donovan and Pete Miranda for help with sample preparation and optical profilometry.

References

- [1] Tsutsumi, Y.; Nishikata, A.; Tsuru, T. *Corrosion Sci.* **2007**. *99*. 1399-1407.
- [2] Lin, C.M.; Chiou, Y.C.; Lee, R.T. *Wear.* **2001**. *249*. 132-141.
- [3] Jones, D.A. *Principles & Prevention of Corrosion*. Prentice Hall: Upper Saddle River, NJ, 1996. 224-226.

About the Author



Brandon Christoffersen is currently a senior at Boise State University. He is pursuing a Bachelor's in Materials Science & Engineering and is a two-time National Science Foundation Scholar in Materials Science. He has spent the last two years doing research in the Advanced Materials Laboratory at Boise State, under Dr. Darryl P. Butt. Much of his research has focused on steel alloys and their surface behavior in marine environments. He has also done some work in nitride coatings, and powder characterization. In addition, Brandon is a captain on the Track & Field and Cross-Country teams for Boise State.

JOIN STUDENTS, SCIENTISTS AND ENGINEERS FROM AROUND THE GLOBE!

Become a student member of an MSE professional society:



Material Advantage

provides a single low-cost student membership that provides access to the materials science and engineering professional's most preeminent societies:

- The American Ceramic Society (ACerS)
 - Association for Iron & Steel Technology (AIST)
 - ASM International
 - The Minerals, Metals and Materials Society (TMS)
- <http://www.materialadvantage.org>



American Ceramic Society

735 Ceramic Place, Suite 100
Westerville, Ohio 43081
Phone: 866-721-3322
Fax: 614-899-6109
E-Mail: info@ceramics.org
<http://www.ceramics.org>



The Association for Iron & Steel Technology

186 Thorn Hill Road
Warrendale, PA 15086
Phone: 724-776-6040
Fax: 724-776-1880
Email: info@aist.org
<http://www.aist.org>



ASM International

9639 Kinsman Road
Materials Park, OH 44073-0002 USA
Phone: 800-336-5152 (U.S. and Canada)
800-368-9800 (Europe)
Fax: 440-338-4634
Email: cust-srv@asminternational.org
<http://www.asminternational.org>



The Minerals, Metals, and Materials Society

184 Thorn Hill Road
Warrendale, PA 15086-7514 USA
Phone: 800-759-4867 (U.S. and Canada Only)
724-776-9000 (Elsewhere)
Fax: 724-776-3770
E-Mail: members@tms.org
<http://www.tms.org>



Materials Research Society

Materials Research Society

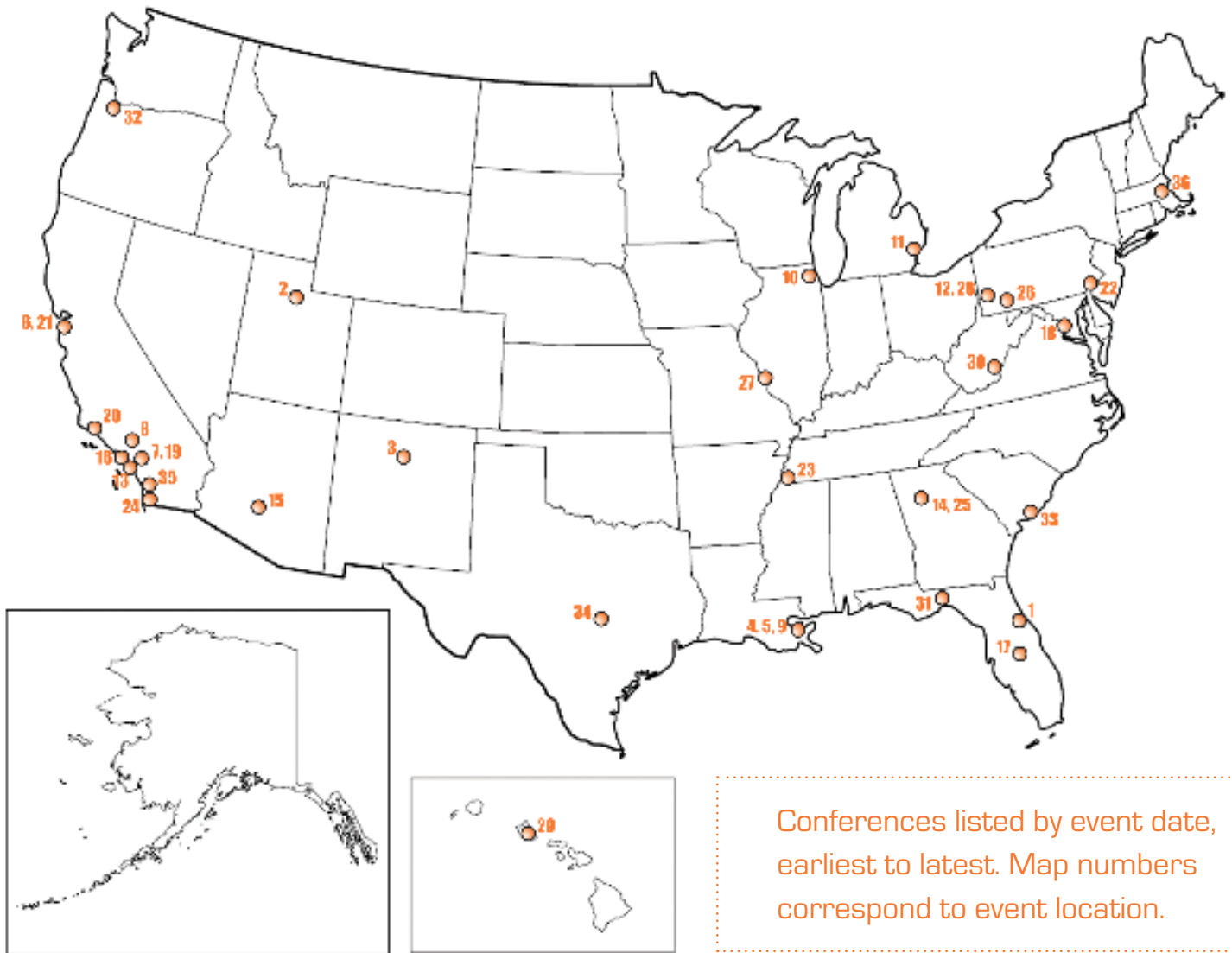
506 Keystone Drive
Warrendale, PA 15086-7573
Phone: 724-779-3003
Fax: 724-779-8313
Email: info@mrs.org
<http://www.mrs.org>



American Foundry Society

1695 North Penny Lane
Schaumburg, IL 60173
Tel: 800-537-4237
847-824-0181
Fax: 847-824-7848
<http://www.afsinc.org>

UPCOMING MATERIALS CONFERENCES



Conferences listed by event date, earliest to latest. Map numbers correspond to event location.

1) ACerS- The American Ceramic Society

32nd International Conference & Exposition on Advanced Ceramics & Composites

January 27-February 1, 2008, Daytona Beach, FL
www.ceramics.org/meetings/daytona2008/

2) SME - Society for Mining, Metallurgy, and Exploration

2008 SME Annual Meeting & Exhibit

February 24-27, 2008, Salt Lake City, UT
www.smenet.org/meetings/

3) ISAF 2008: 17th International Symposium on Applications of Ferroelectrics

February 24-28, 2008, Sante Fe, NM
www.isaf2008.com/ISAF_2008/Home.html

4) ASCE - American Society of Civil Engineers

GeoCongress 2008

March 9-12, 2008, New Orleans, LA
<http://content.asce.org/conferences/geocongress2008/>

5) TMS - The Minerals, Metals, & Materials Society

TMS 2008 Annual Meeting

March 9-13, 2008, New Orleans, LA
www.tms.org/Meetings/Meetings.asp

6) MRS - Materials Research Society

MRS Spring Meeting 2008

March 24-28, 2008, San Francisco, CA
www.mrs.org/s_mrs/sec.asp?CID=6689&DID=174642

7) ASNT - American Society for Nondestructive Testing

ASNT 17th Annual Research Symposium & Conference

March 31-April 4, 2008, Anaheim, CA
www.asnt.org/events/conferences/rs08/rs08.htm

8) SME - Society of Manufacturing Engineers

WESTEC 2008 Exposition & Conference

March 31-April 3, 2008, Los Angeles, CA
www.sme.org/

9) ACS - American Chemistry Society

Spring 2008 National Meeting & Exposition

April 6-10, 2008, New Orleans, LA
<http://portal.acs.org/portal/PublicWebSite/meetings/index.htm>

10) AIAA - American Institute of Aeronautics and Astronautics

49th AIAA/ASME/ASCE/AHS/ASC Structures, Structural Dynamics, and Materials Conference

April 7-10, 2008, Schaumburg, IL
www.aiaa.org/content.cfm?pageid=230&lumeetingid=1875

11) SAE International

SAE 2008 World Congress
April 14-17, 2008, Detroit, MI
www.sae.org/congress/

12) AIST - The Association for Iron and Steel Technology

AISTech 2008 - The Iron & Steel Technology Conference and Exposition
May 5-8, 2008, Pittsburgh, PA
www.aist.org/08_aistech/2008aistech.htm

13) International Hot Isostatic Pressing Conference

May 6-9, 2008, Huntington Beach, CA
www.hip2008.com/

14) AFS - American Foundry Society

CastExpo '08
May 17-20, 2008, Atlanta, GA
www.castexpo.com/

15) ECS - Electrochemical Society

213th ECS Meeting
May 18-23, 2008, Phoenix, AZ
www.electrochem.org/meetings/biannual/213/213.htm

16) SAMPE - Society for the Advancement of Materials and Process Engineering

SAMPE '08
May 18-22, 2008, Long Beach, CA
www.sampe.org/events/2008LongBeach.aspx

17) IEEE - Institute of Electrical and Electronics Engineers

2008 IEEE 58th Electronic Components and Technology Conference (ECTC 2008)
May 27-30, 2008, Lake Buena Vista, FL
www.ectc.net/

18) MPIF - Metal Powder Industries Federation

2008 World Congress on Powder Metallurgy & Particulate Materials
June 8-12, 2008, Washington, D.C.

19) ANS - American Nuclear Society

American Nuclear Society 2008 Annual Meeting
June 8-12, 2008, Anaheim CA
www.ans.org/meetings/index.cgi?c=n#am2008

20) TMS - The Minerals, Metals, & Materials Society

Electronic Materials Conference 2008
June 25-27, 2008, Santa Barbara, CA
www.tms.org/Meetings/Specialty/EMC08/home.html

21) SAE International

38th International Conference on Environmental Systems
June 29-July 3, 2008, San Francisco, CA
www.sae.org/events/ice/

22) ACS - American Chemistry Society

Fall 2008 National Meeting & Exposition
August 17-21, 2008, Philadelphia, PA
<http://portal.acs.org/portal/PublicWebSite/meetings/index.htm>

23) SAMPE - Society for the Advancement of Materials and Process Engineering

SAMPE Fall Technical Conference 2008
September 8-11, 2008, Memphis, TN
www.sampe.org/events/2008Memphis.aspx

24) AIAA - American Institute of Aeronautics and Astronautics

AIAA Space 2008 Congerence & Exposition
September 9-11, 2008, San Diego, CA
www.aiaa.org/content.cfm?pageid=230&lumeetingid=1872

25) SFB - Society for Biomaterials

2008 SFB Meeting on Translational Research
September 11-13, 2008, Atlanta, GA
www.biomaterials.org/Meetings/08AnnualMeeting/index.cfm

26) TMS - The Minerals, Metals, & Materials Society

Superalloys 2008
September 14-18, 2008, Champion, PA
www.tms.org/Meetings/specialty/superalloys2008/home.html

27) BMES - Biomedical Engineering Society

2008 BMES Annual Fall Meeting
October 1-4, 2008, St Louis, MO
bme.wustl.edu/BMES2008/SL_FLYR-10-22-07_V4.pdf

28) MS&T '08: Materials Science & Technology 2008 Conference and Exhibition

October 5-9, 2008, Pittsburg, PA
www.matscitech.org/2008/home.html

29) ECS - Electrochemical Society

PRiME 2008: Joint International Meeting
October 12-17, 2008, Honolulu, HI
www.electrochem.org/meetings/biannual/214/214.htm

30) The Aluminum Association, Inc.

75th Meeting of the Aluminum Association
October 20-21, 2008, White Sulphur Springs, WV
www.aluminum.org/

31) 2008 Fourth International Conference on Multiscale Materials Modeling

October 27-31, 2008, Tallahassee, FL
<http://www.mmm2008.org/bin/view.pl/Main/WebHome>

32) ASM International

34th International Symposium for Testing & Failure Analysis
November 2-6, 2008, Portland, OR
www.istfa.org/

33) ASNT - American Society for Nondestructive Testing

ASNT Fall Conference and Quality Testing Show 2008
November 10-14, 2008, Charleston, SC
www.asnt.org/events/conferences/fc08/fc08.htm

34) 53rd Conference on Magnetism and Magnetic Materials

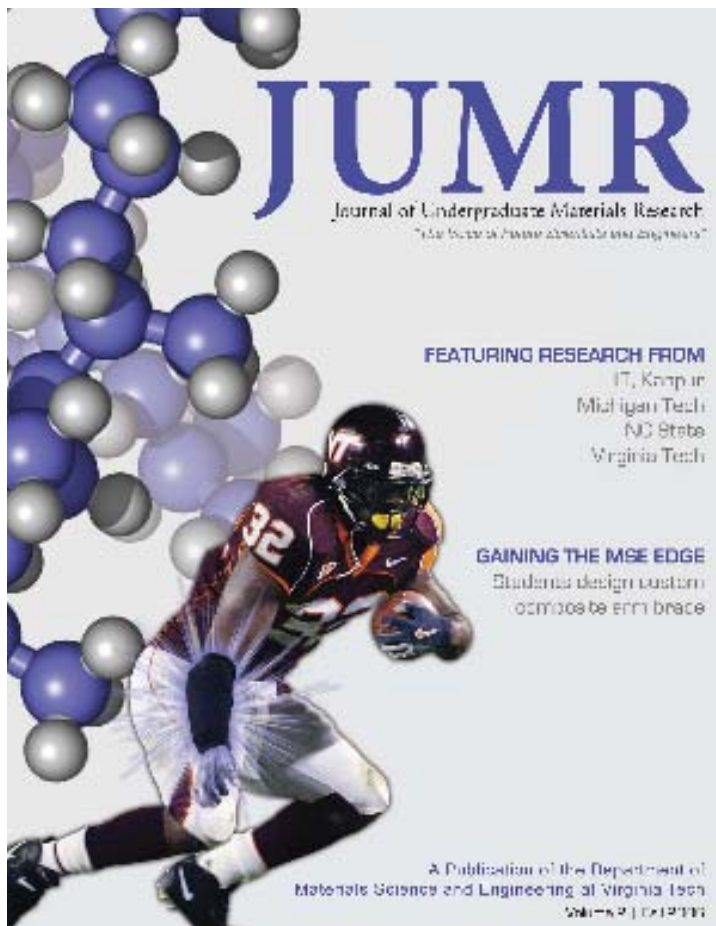
November 10-14, 2008, Austin, TX
www.magnetism.org/futureconf.html

35) ACerS - The American Ceramic Society

International Conference on Sintering - Sintering 2008
November 16-20, 2008, La Jolla, CA
www.ceramics.org/meetings/sintering2008/

36) MRS - Materials Research Society

2008 MRS Fall Meeting
December 1-5, 2008, Boston, MA
www.mrs.org/s_mrs/sec.asp?CID=6688&DID=174641



Publish. Gain recognition. Be part of something exciting.

**Submit your paper for
consideration in Volume 4**

If you are an undergraduate student at any institution working on a materials-related project, here is your chance to become published. Your submitted paper will undergo a peer-review for consideration in Volume 4 of the *Journal of Undergraduate Materials Research*. Please submit your manuscripts by **5:00 PM, May 2, 2008**.

For submission requirements, see:
<http://www.jumr.mse.vt.edu>

Manuscripts or questions should be sent to:
**JUMR
213 Holden Hall
Virginia Tech
Blacksburg, VA 24061
jumr@mse.vt.edu**

JUMR
213 Holden Hall
Virginia Tech
Blacksburg, VA 24061

**Non-profit organization
U.S. Postage PAID
Blacksburg, VA 24060**

Permit No. 28